1992

Control of the wake from a simulated blade by trailing-edge blowing

Timothy E. Corcoran
Lehigh University

AUTHOR:

Corcoran, Timothy E.

TITLE:

Control of the Wake From
From a Simulated Blade
by Trailing-Edge Blowing

DATE: May 31, 1992

CONTROL OF THE WAKE FROM A SIMULATED BLADE BY TRAILING-EDGE BLOWING

by Timothy E. Corcoran

A Thesis
Presented to the Graduate Committee
of Lehigh University
in Candidacy for the Degree of
Master of Science
in
Mechanical Engineering

Lehigh University
Bethlehem, Pennsylvania
January 1992

CERTIFICATE OF APPROVAL

This thesis is accepted and approved in partial fulfillment of the requirements for the degree of Master of Science.

Date: 02/10/92

Professor in Charge
Dr. Donald O. Rockwell

Department Chairperson
Dr. Robert P. Wei

DEDICATION

To My Parents
For their time, love and dedication.

IN REMEMBRANCE

of my brother and friend Michael R. Knapp on his passing
January 5, 1992

ACKNOWLEDGEMENTS

This research was funded by Pratt-Whitney Aircraft Engine Corp. and was administered through the Acoustics Department of their Commercial Aircraft Division in East Hartford, CT. My thanks go out to the project managers Doug Mathews and Barry Wagner for their assistance throughout the project.

I am assuming that there will be a considerable faction who will stop reading by the end of this page so I will try to make it good.

First of all, I would like to thank my family: my parents, Edward and Ruth Corcoran, my brothers Bil and Ned, and my sister-in-law Pattie, for their help through 5.5 years of college.

My thanks go out as well to my advisor Dr. Donald Rockwell for his guidance, insight, and indulgence of my ridiculous lack of patience. The lessons you taught me went far beyond fluid mechanics.

Good luck to the continuing (though God help you, temporary) inmates of the fluids lab, especially Gary, Joe, Georg, John, Jin and Özgür who helped all the way through. (P.S. Try to have that statue of Chuck Magness done by the time I come back.)

Thanks go to the true Engineers I ran across at Lehigh, Dick Towne, Emerson Wagner, and Frank Klucsik. Dick keep my vet in shape while I am gone.

Thanks to my freshman roommate turned grad school roommate Eric Soderberg. Anchors away.....

Thanks go to my fraternity brothers for keeping me from taking any of this seriously. Jay, Marty, Jason, and Mark all deserve more recognition than I would ever want to have published here. P.S.....don't burn down the house.

Finally, thanks to my '82 Jetta for refusing to meet its maker after 160,000 + miles. Duct tape truly is the fastener of the 21st century.

TABLE OF CONTENTS

LIST OF FIGURES

NOTATION

U - Time-Averaged Streamwise Velocity

U_∞ - Freestream Velocity

l - Wake Half-Width

ν_t - Eddy Viscosity

u_{rms} - rms of Streamwise Velocity Fluctuation

v_{rms} - rms of Cross Stream Velocity Fluctuation

$\overline{u'v'}$ - Reynolds Stress

U_s, U_d - Deficit Velocity ($1 - U/U_\infty$) at Centerline

l_o - Wake Half-Width for Zero-Blowing Case

V_j - Blowing Velocity

V_j^* - Blowing Velocity for Momentumless Wake

Q - Volume Flow Rate

V^2A - Momentum Term

f - Focal Length

s - Focal Point of Lens Combination

z - Combination Principal Point Separation

δ - Boundary Layer Thickness

ABSTRACT

One of the most prevalent components of noise created by an aircraft engine is fan noise. One of the major causes of this noise is the wake from a fan blade. This wake impinges upon a downstream stator causing unsteady lift and noise generation. This thesis examines the possible use of trailing-edge blowing from the fan blades to decrease the wake deficit caused by the blades, thereby decreasing the generated noise.

Experimentation was done on a simulated blade within a water channel. A fully turbulent boundary layer was created upstream of the trailing-edge of the blade. The trailing-edge blowing was done through two different trailing edge configurations: (1) a single slit; and (2) a double slit. In both cases, the blowing was done at six different rates. The rate of blowing was increased to and beyond the level where a momentumless wake was created.

Experimental measurements were taken using scanning Particle Image Velocimetry (PIV) and an ensemble-averaging technique, which used Taylor's Hypothesis, in order to generate turbulence data. Data generated included velocity profiles, u_{rms} and v_{rms} profiles, Reynolds stress profiles, and instantaneous vorticity and velocity fields.

Primary comparisons with rotor blade wake data showed the water tunnel model to be an accurate test model for a rotor blade.

The single-slit trailing-edge demonstrated a remarkable transformation when blowing was raised to the momentumless level. All measured quantities tended towards values corresponding to a uniform flow. Lower blowing rates had much smaller effects.

The double-slit trailing-edge proved to be a more complex flow case with somewhat less uniform flow generated

at / near the most effective blowing rate. The various turbulence quantities were attenuated in a different fashion than for the case of the single-slit.

In general, trailing-edge blowing effectively attenuates the wake deficit of a model rotor blade. This attenuation will reduce engine noise at the blade passing frequency. In order to minimize the amount of blowing required to achieve attenuation of the wake deficit, further investigation of alternate trailing-edge configurations is called for.

INTRODUCTION

One of the primary tasks an engineer faces in the acoustic design of a jet engine is the reduction of noise. This problem is becoming more and more prevalent due to the imposition of local ordinances to prevent noise pollution in areas neighboring airports. Similar federal regulations are also in place.

The noise created within a jet engine consists of several components caused by different parts of the engine. The various components of the noise occur at different frequencies, and affect regions at varying distances from the plane. Some of these components include compressor noise, combustion noise, turbine noise, fan exhaust noise, jet noise, and the primary concern of this paper, fan inlet noise.

The fan inlet noise amounts to a large part of the total noise created by the jet engine. It persists for a long distance, primarily in the regions in front of the plane, and is especially prevalent at take-off. Its audible frequency spectrum shows several intense peaks of high frequency noise while the plane is taking off.

Beyond using sound absorbing materials to control a part of this noise, Pratt-Whitney has begun investigations of more active methods of noise control that rely on an understanding of the fluid-dynamic interactions that cause the noise. The major cause of the fan inlet noise is the downstream effect of the wakes created by the blades of the first inlet fan of the engine. These wakes travel downstream and cause the stator blades of the engine to experience unsteady lift, causing them to radiate noise.

One of the primary investigations into this phenomena was done by Kemp and Sears (1955). This work considers the

effect of the viscous wake created by a single stator blade on a downstream rotor blade. It relies on past empirical work to predict the nature of the viscous wakes emanating from a cascade of blades, and then utilizes thin airfoil theory to predict the forces and moments felt by the downstream blade. It concludes that the lift felt by the downstream blades is nearly proportional to the profile drag coefficient of the upstream blades. An analogy can easily be drawn to see the effect a large fan inlet blade could have on the downstream stator blades. This is important due to a general trend in the industry towards larger inlet sections and larger inlet fans.

Kuethe (1972) considers the problem from a different viewpoint and proposes the use of trailing-edge vortex generators to aid in mixing the wake fluid with the freestream, thereby decreasing the wake deficit of the upstream blades. A decrease in this deficit should affect a proportional decrease in the unsteady lift felt by the downstream blades. He concludes that increased mixing caused by the vortex generation decreases the downstream deficit and also suppresses the formation of the Kármán Vortex street over a large range of Reynolds number. Both effects are beneficial.

The primary thrust of this investigation will be to seek reduction of the wake deficit caused by the first row of fan blades, with the intention of reducing the engine noise. The technique to be used to reduce this deficit will involve injection of fluid from the trailing-edge of a model blade. This fluid will add momentum to the wake of the blade, depending on the velocity and mass flow rate of its injection. This project seeks to investigate the effects of various injection rates and physical injection configurations on the downstream wake of the model blade.

This investigation will be performed in a water

channel test facility with a model to be described subsequently. The model will involve generation of a turbulent boundary layer upstream of the trailing-edge in accord with the conditions that would be present within a jet engine.

The overall objective of this investigation is determination of the mean velocity and turbulence downstream of the model blade, primarily using Particle Image Velocimetry.

PREVIOUS THEORETICAL STUDIES

The wake of an object in a fluid is characterized by a region of low velocity within the shear flow. This region constitutes a momentum deficit, which in turn is related to the drag of the object. In concept, momentum could be added to the fluid in this region to offset the deficit. The wake downstream of the body would then be a momentumless wake.

In Tennekes and Lumley (1972), the problem of a self-propelled body is considered. A self-propelled body traveling at constant speed, such as a torpedo, adds just enough momentum through its propulsor to overcome the momentum loss associated with its drag. A theoretical analysis of this problem is made difficult by the fact that the momentum integral disappears due to the zero net momentum, negating the standard self-preserving wake analysis. To overcome this problem, the very approximate assumption that eddy viscosity, ν_t, is independent of vertical position within the wake of the body, is made by Tennekes and Lumley (1972). Their analysis proceeds through a solution of the momentum equation for turbulent flow, which assumes self-preservation of the velocity deficit.

The result of this solution is the prediction of two characteristics of the wake. One characteristic is the streamwise decay of the centerline velocity deficit of the wake, U_s. The other involves the spreading of the wake half-width, l. This distance, l, represents the distance from the centerline of the wake to the point at which the wake deficit has one-half its value at the centerline. (See figure 1.1.) For the wake of the self-propelled body, Tennekes and Lumley predict the streamwise decay of the deficit, U_s, to be of the order of $Ax^{-3/4}$, where A is a

constant. They predict the spreading of the half-width, l, to be of the order of $Bx^{1/4}$, where again B is a constant. An analysis of a pure wake, using the momentum integral, predicts decay of U_s to be of the order of $Ax^{-1/2}$, and l to be of the order of $Bx^{1/2}$. It would seem, therefore, that the momentumless wake would decay much faster than the pure wake.

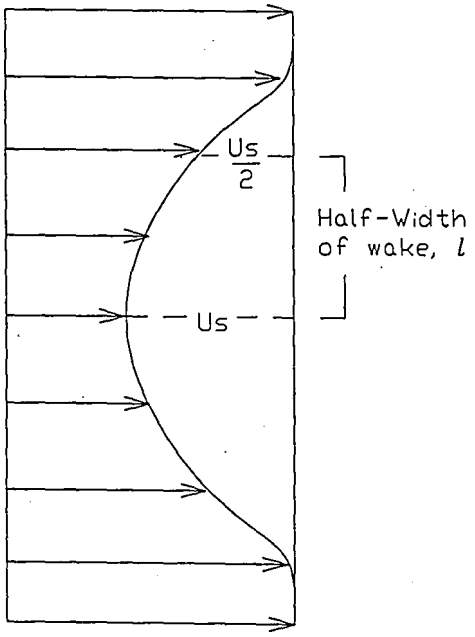

FIGURE 1.1: The Wake Deficit

Several other models have been proposed to predict this behavior. They will be detailed only briefly here.

Finson (1974) makes an analogy between the behavior of a momentumless wake and the effects found in homogeneous grid turbulence. He theorizes that the flow possesses the combined characteristics of the grid turbulence, along with some effects common to free-shear flow. He predicts U_s to be of the order of $x^{-1.636}$, and l to be of the order of $x^{0.276}$. These results are limited to axisymmetric bodies.

Other theoretical methods rely on the use of a turbulent energy model. Dmitrenko et. al (1987) uses such a model and seeks verification by comparison with experimental results. Fair agreement was found in predicting U_s, but poor agreement existed for many of the other predicted quantities. Hassid (1980) proposes a model that shows fair agreement with previous results. He predicts U_s to be of the order of $x^{-1.27}$. This model is addressed again in the primarily experimental work of Park (1989). Park extends the concepts to deduce the extreme difference in turbulence production between the momentumless wake and the pure wake. He theorizes that this may be one of the primary effects contributing to the difference in their decay rates. Swanson and Schetz (1975) perform an analysis based on a kinetic energy method, again reporting agreement with experimental data.

PREVIOUS EXPERIMENTAL INVESTIGATIONS

For the purpose of experimentation, the momentumless wake concept is best thought of as the combination of a pure-wake flow and a jet flow. Tennekes and Lumley (1972) state that the presence of even a small component of momentum within the nearly momentumless wake will cause the profiles to appear either wake-like or jet-like. This behavior does become apparent when attempting to tune the wake deficit. Another well-noted experimental effect is the momentumless wake's ability to "remember" its source of generation. Unlike a pure wake, the characteristics of a momentumless wake are greatly affected by the method that was used to generate the momentumless wake. This has prompted many experimenters to investigate the use of different physical arrangements for generating momentumless wakes.

Some of earliest experimental work involving momentumless wakes was done by Ridjanovic (1963) and Wang (1963) in their thesis work at the University of Iowa. This work was continued by Naudascher (1965). The work in these experiments was done using a disk with the center removed. Fluid was introduced through the center of the ring, adding momentum into the wake. The research presented was extensive, and extended up to 130 disk diameters downstream. Naudascher concludes that the downstream flow from the disk can be divided into two basic regions. The region closer to the disk is dominated by the characteristics of a basic turbulent shear flow. Further downstream, the characteristics turn to those found in decaying homogeneous turbulence. He reports U_s to decay as x^{-2} for the momentumless wake of the disk, versus a pure wake decay rate of the order of $x^{-2/3}$. Similarly, the half-

width, l, is reported to grow as $x^{1/5}$ for the momentumless wake, and $x^{1/3}$ for the pure wake.

Another investigation, involving an axisymmetric body was performed by Schetz and Jakubowski (1980). They examined data taken from a body in a wind tunnel, first providing no added momentum, and then adding momentum using a propeller, and then a jet. The propeller and jet were used to create momentumless wakes, which proved to be quite different in their nature. The jet-propelled model showed the highest level of axial turbulence intensity with a slower decay rate than the propeller-driven model. They also note that the results differ from those of Naudascher, again lending credence to the momentumless wake's ability to "remember" its method of generation.

Schooley and Stewart (1962) examine the wake of an axisymmetric, self-propelled body within a stratified medium. They note a significant difference in the generated wake. Under a vertical density gradient, the wake collapses vertically, and spreads horizontally, forming waves in the medium.

Higuchi (1977) uses a tube mounted axially in the flow in order to form a momentumless wake. Fluid ejected from the open end of the tube was used to balance the momentum loss caused by the wake of the tube itself. The work demonstrated that artificial boundary layer thickening along the shear surfaces of the tube (caused by specially mounted rims) caused the turbulence to decay more quickly. He also provides flow visualization of the eddy structures generated by the tube.

Some of the earliest work on momentum injection from a two-dimensional body was done by Wood (1964). Wood's work was done using a standard airfoil which was equipped to bleed air from its trailing edge. The trailing-edge was blunt. Wood states that the drag of

the airfoil decreased with an increased amount of air flow from the trailing edge. He asserts that the drag reduction is caused by the bleed flow's ability to offset the formation of the instability caused by the separated shear layers. He also notes a decrease in the trailing-edge vorticity. Although he finds an optimum bleed rate, at which the drag appears to settle to a reduced level, he makes no mention of the concept of the momentumless wake within his work, nor does he address the concept of adding momentum to the flow through the base bleed.

Wood (1967) performed similar water-based visualization work. He concluded that the fluid ejection from the trailing edge displaces the formation of the vortex street away from the body. It also decreases the strength of the vortices, but does not affect their rates of decay. He proposes that the vorticity created along the trailing-edge of a body without any blowing serves only to mix the dead fluid within the wake with the higher speed fluid above it. When base blowing is used, the mixing is done by shear between the two layers, therefore decreasing the vorticity.

Bearman (1966) performed very similar work to Wood. He demonstrated that the vortex street disappeared at the proper rate of trailing-edge blowing, only to appear again further downstream. Neither Wood nor Bearman achieved a momentumless wake.

Motallebi and Norbury (1981) perform wind tunnel tests on an airfoil equipped with training-edge blowing, at free stream velocities ranging from M=0.68 to M=1.3. They provide measurements of base pressure and Spark-Schlieren photographs demonstrating the effect of the base blowing on the Kármán vortex street. For transonic flow, a small amount of base bleed resulted in the relocation of the vortex motion downstream, decreasing the base pressure. As the bleed rate increased, the vortex motions were found to

disappear near the point at which the maximum base pressure was predicted. Bleed rates beyond this point caused the formation of pairs of vortices: one drawing its vorticity from the shear layer, and the other alternately drawing it from the bleed air. At higher bleed rates, the bleed itself becomes supersonic as it progresses away from the base. At this bleed rate, two vortex streets form, as the vortex formation becomes increasingly dominated by the presence of a central jet. At M=1.3, similar phenomena were noted.

Perhaps the previous research most applicable to this project is that of Park (1989). Park utilized airfoil-like bodies with various injection schemes, to create momentumless wakes within a wind tunnel. Park's measurements include downstream measurements of wake decay, smoke visualization, and turbulence measurements.

In the visualization results, pure-wakes, momentumless-wakes, and jet-wakes are compared for each of three different trailing-edges. One trailing-edge had a single slit across its center through which fluid was ejected. Another had an asymmetric slot, and the third edge had two slots on opposite sides of the centerline. His results show the presence of different turbulent structures within the flow for each different trailing-edge configuration.

Hot wire results reveal the expected rapid decay of turbulence within the momentumless wake. Results for the single, centered slit demonstrated a reduction of U_S as $x^{-0.92}$, an increase of half-width, l, as $x^{0.3}$, and a decrease in Reynolds stress, $\overline{u'v'}$ as $x^{-1.84}$. Results were similar for the asymmetric single jet with the only differences being a reduction of U_S as $x^{-1.24}$, and a slightly larger rate of increase for the half-width, l. Results for the dual jet case proved to remarkably different. In this case, U_S was found to decrease as $x^{-2.02}$, l to increase as $x^{0.46}$ and the Reynolds stress to

decrease as $x^{-2.49}$.

From his observations, Park reasserts the similarity between the characteristics of a momentumless wake, and those found in the wake of grid turbulence. Simple turbulence models are dismissed in lieu of higher order models of a momentumless wake. The dependence of a momentumless wake on the conditions of its creation is reinforced by the difference of flows from different trailing-edge configurations.

In Park (1985), the latter point is clarified somewhat. The dependence of U_s, l, and u_{rms} on the trailing-edge blowing configuration is addressed. For each case, velocity and length scales are found to normalize the data for each trailing-edge configuration into self-similar forms. The forms are, however, unique to each configuration. In conclusion, this study proposes that more complex velocity and length scales may be required to normalize the data obtained from various trailing-edges. It asserts that the complexity of these normalizations results from the complex nature of the momentum injection. It should be noted that throughout Park's work, the momentumless wake is simply "tuned in" using visualization. Therefore no data are available as to the mass flow into the wake, nor are any data available on the rate of its injection.

EXPERIMENTAL APPARATUS

The primary test facility used for this project was the large water tunnel (rm. 174, Packard Lab). The tunnel is approximately 3 ft. wide, 16. ft long, and constructed of optically transparent plexiglass with large inlet and exit tanks at either end. Typical water depths in the tunnel are of the order of 21 inches. Water flow rates in the tunnel can be established up to approximately 9 inches per second. The flow speed is controlled by varying the speed of the pump motor. Another smaller, recirculating pump continually forces the water through filters, maintaining the cleanliness of the water.

Figure 2.1 shows the top view of the water channel with the full experimental apparatus in place. Figure 2.2 shows the side view. Design of the initial rig was done by Naumann and Rockwell (1992). The flow is pumped into the entrance tank at left, and flows forward onto the large conditioning plate. The plate is designed to trigger transition of the boundary layer near its leading-edge. Details on generation of the fully turbulent boundary layer will be presented later. The plate is 6.0 ft long, 0.5 inches thick, and spans the entire width of the tunnel. It is supported by legs at a vertical height approximately half the water height in the tunnel; this height corresponds to a distance 10 inches from bottom of the tank to the bottom of the plate. The plate has several rows of hemispherical beads along its leading-edge to facilitate transition. These will be discussed subsequently.

The trailing-edge of the conditioning plate is mounted within a set of false walls that span the remainder of the length of the test section. The false walls add support to the system and protect the area of experimentation from any

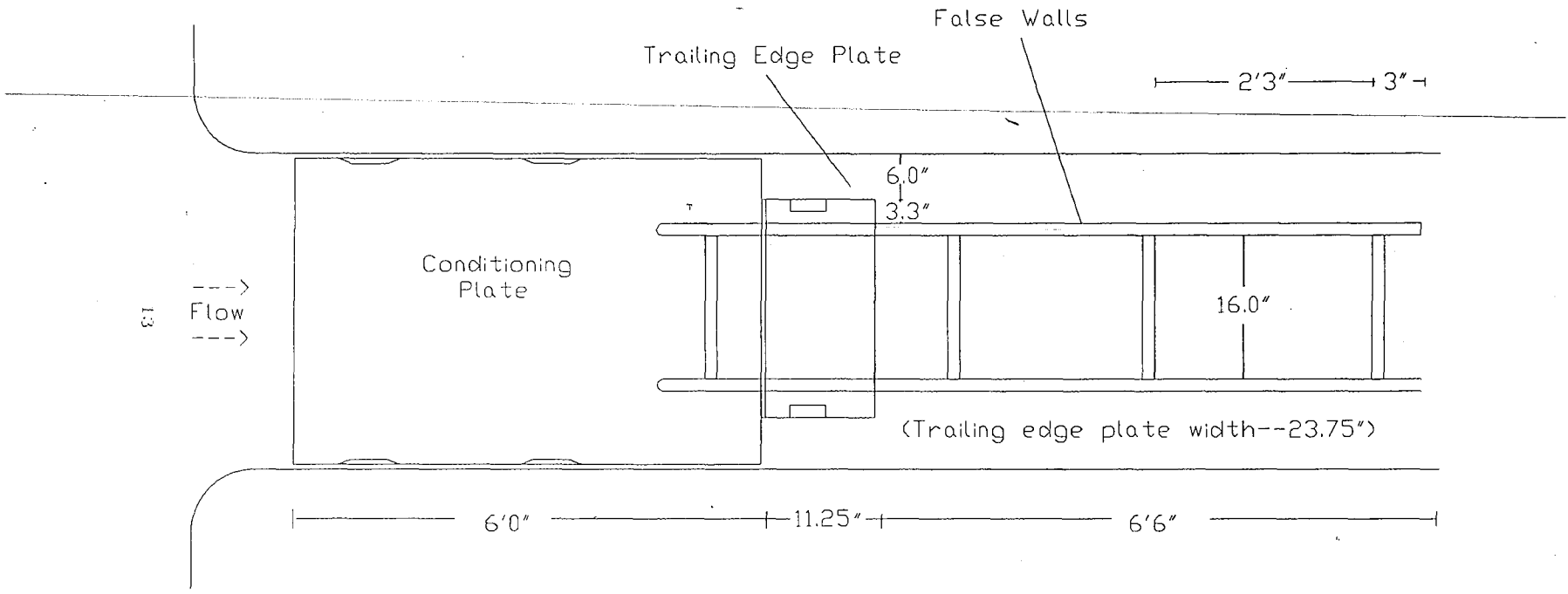

FIGURE 2.1: TOP VIEW OF TEST SECTION

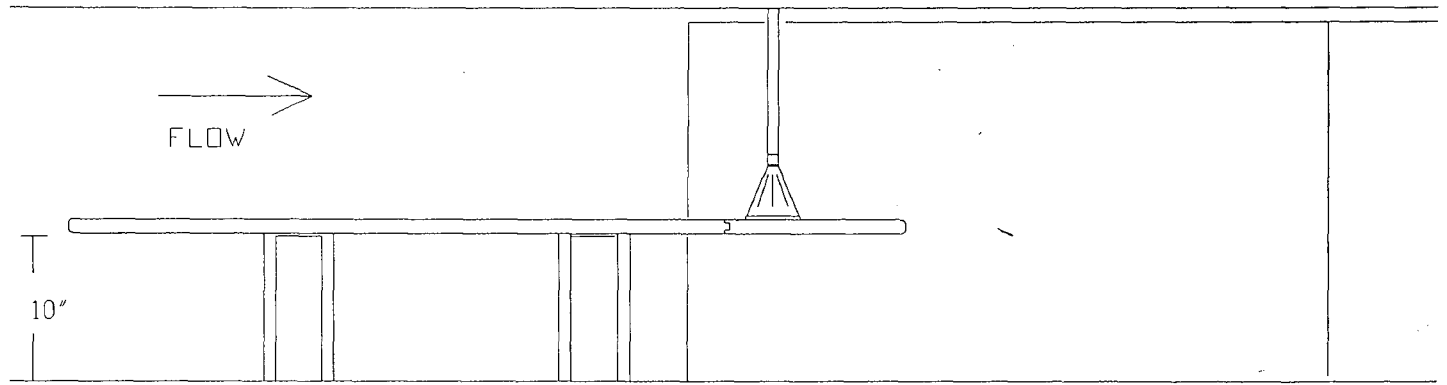

FIGURE 2.2: SIDE VIEW OF TEST SECTION

tunnel wall effects. All experimentation was done near the center of the false walls.

The trailing-edge of the conditioning plate was tongue cut so that the experimental trailing-edge sections could be joined to it. Trailing-edge sections were grooved to fit into the end of the conditioning plate and allowed to rest in a large groove within the false walls. This feature allowed experiments to be done on multiple trailing-edges without altering the rest of the facility.

The trailing-edge plates compose the heart of the apparatus. The plates themselves are hollow, with various ejection-oriented trailing-edges. A side view of the first trailing-edge appears in figure 2.3. The side view of the second trailing-edge, is given in figure 2.3 a. A pumping system forces water from the exit tank into the region above the trailing-edge plate (figures 2.4 a,b). The water is separated just downstream of the pump and conveyed into two diffuser towers on either side of the trailing-edge plate (on the outside of the false walls). One tower diffuser can be seen in figure 2.3 or 2.3 a. The diffusers are vaned to ensure an even distribution of flow into the trailing-edge plate. Water is pumped through the diffusers and into the hollow plate. From there, it is forced out of the trailing-edge to create the desired blowing conditions. The various trailing-edge configurations will be described at the end of this section.

The pumping system used to generate blowing for the first trailing-edge consists of a small pump (Jabsco Centri Puppy, MD 18510-0000), an in-house produced pump controller, and a flow meter (Micro Computer Controls). A diagram of the system appears in figure 2.4 a. Water from the base of the exit tank is drawn to the pumping system. It first passes through a flow meter, and then into the pump. The flow rate of the pump can be controlled using a

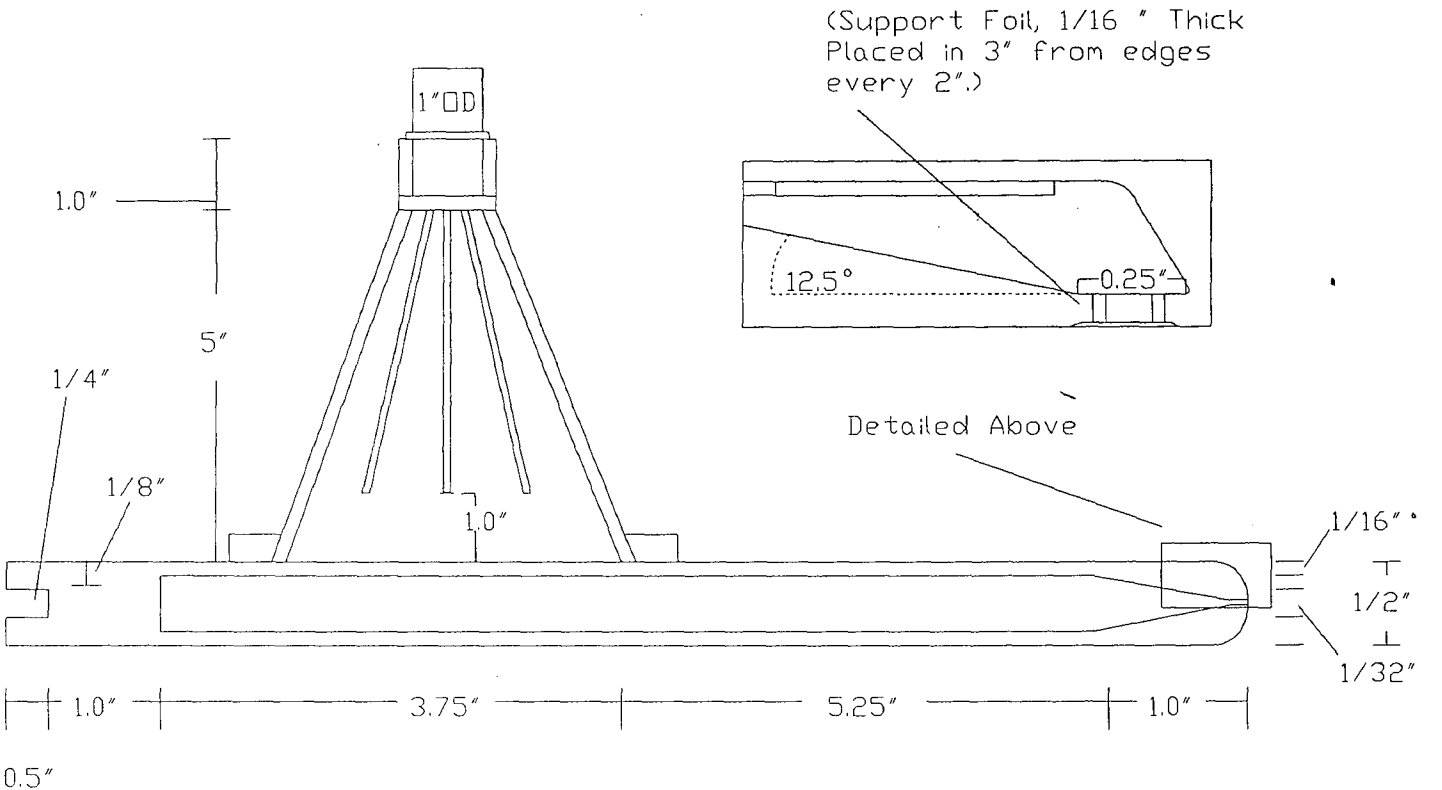

FIGURE 2.3: TRAILING EDGE PLATE NO.1: SIDE VIEW

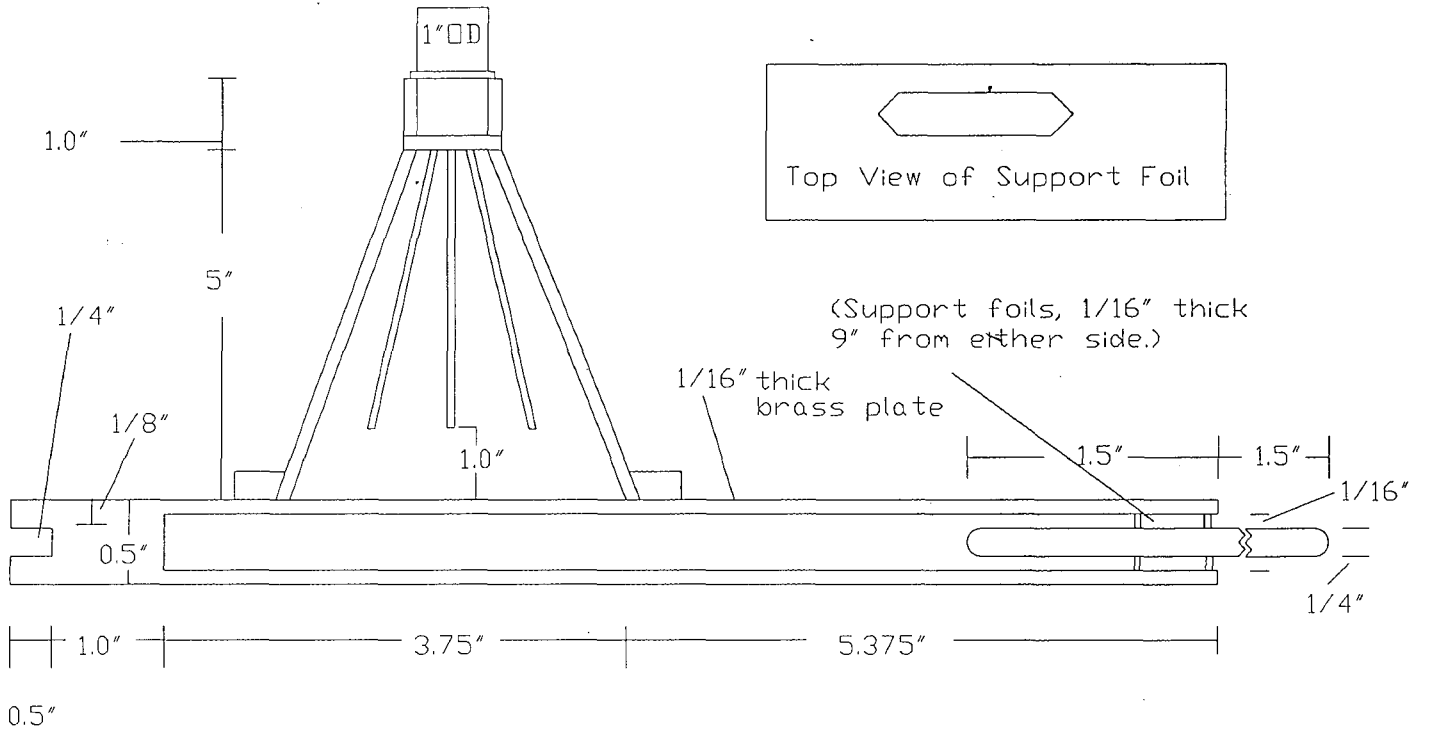

FIGURE 2.3a: TRAILING EDGE PLATE NO. 2: SIDE VIEW

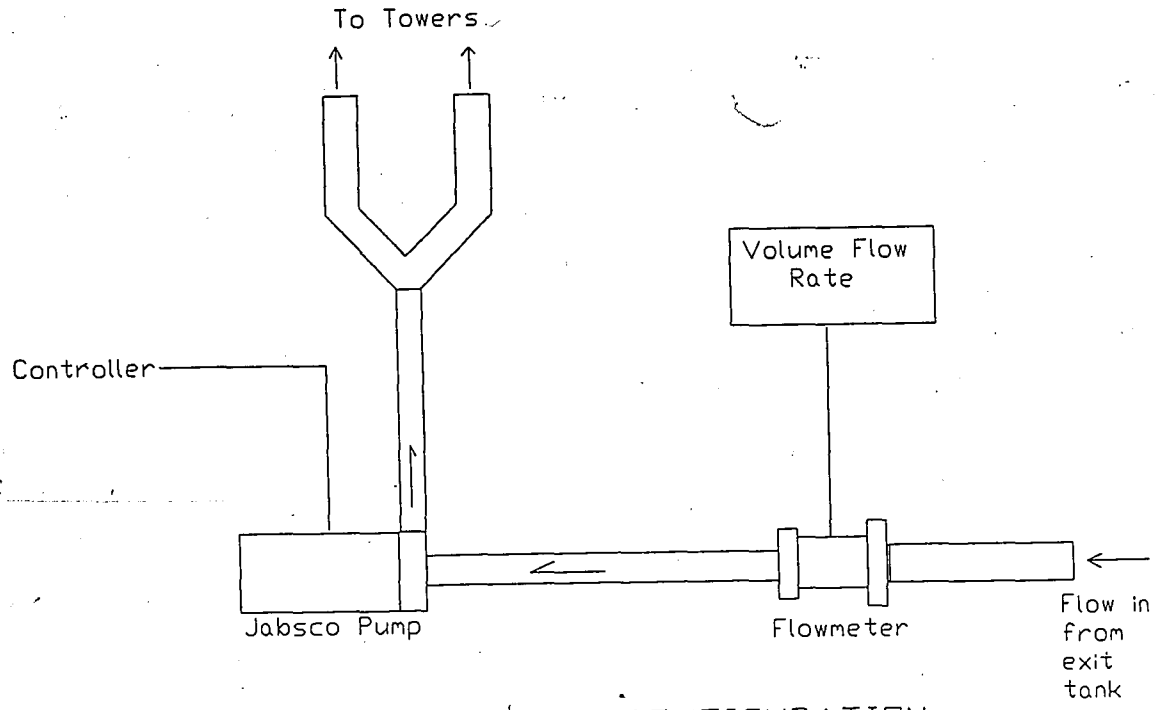

FIGURE 2.4a: PUMP CONFIGURATION FOR SINGLE-SLIT TRAILING EDGE NO. 1

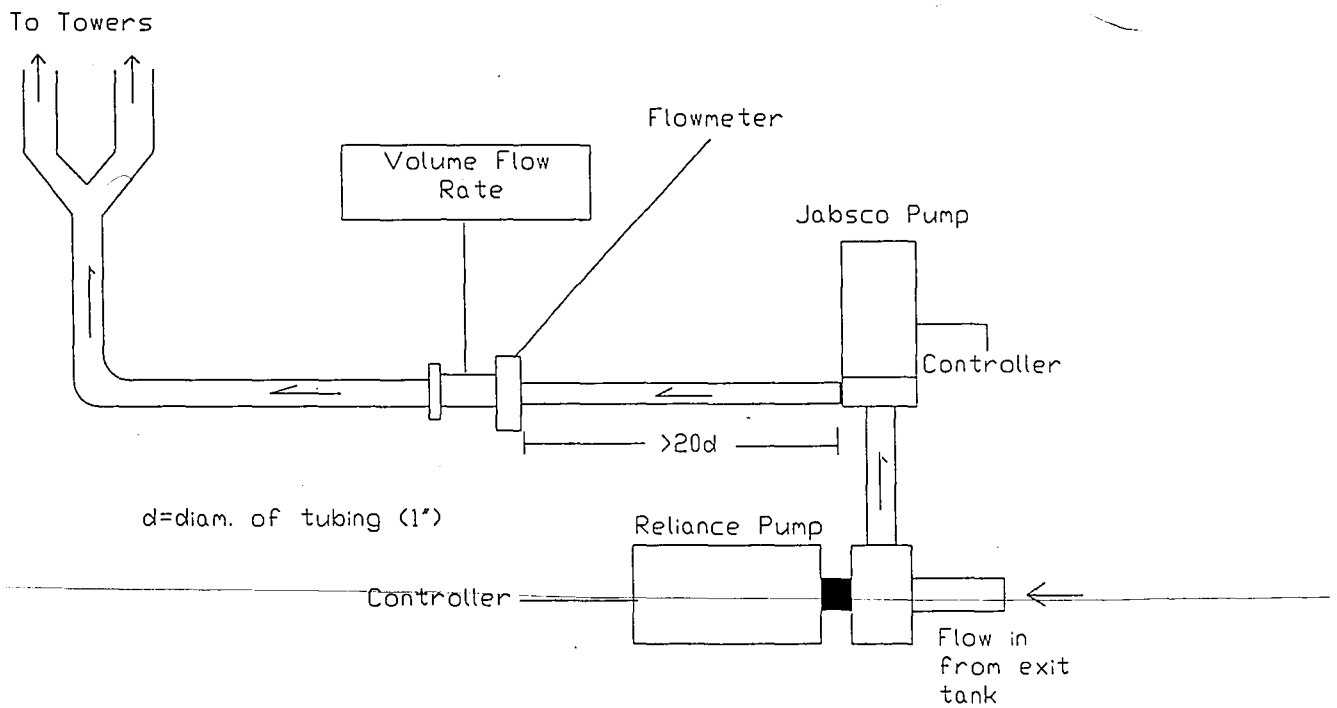

FIGURE 2.4b: PUMP CONFIGURATION FOR DOUBLE-SLIT TRAILING EDGE PLATE NO. 2

dial mounted on the top of the pump controller, with digital readings from the flow meter providing a total flow rate in gallons per minute.

The second trailing-edge required an increase in flow rate that was beyond the capability of the original system. To overcome this difficulty, a second pump (Reliance Centrifugal type TP3) was put in series. (See figure 2.4b.) The flowmeter was also relocated with the hope of obtaining a slight decrease in resistance. The new pumping system allowed rates upwards of 11 Gallons per minute.

Beneath the water tunnel is a rail system used to move the Particle Image Velocimetry optics to the proper location. The laser utilized for this system is located just beyond the entrance tank and off to one side. This laser system is detailed in the section describing Particle Image Velocimetry.

Trailing Edge Configuration 1: Lengthwise slit.

As shown in figure 2.3, the first and most basic trailing-edge configuration is the spanwise slit. The slit is 1/32 inches high, and runs across the width of the plate contained by the false walls. The trailing-edge shape is based on data obtained from Pratt-Whitney and is approximately the trailing-edge shape of a fan blade of their ADP (Advanced Ducted Propeller) series engine. The slit is centered within the trailing-edge.

Initial tests showed that reinforcements of the trailing edge-slit would be necessary to maintain uniform flow. The Bernoulli effect caused the slit of the initial trailing edge to collapse at the center of the span. This problem was alleviated by placing support foils on the

inside of the plate near the trailing edge slit. After this modification, the velocity from the slit proved to be satisfactorily uniform across the span.

Trailing Edge Configuration 2: Double Slit Trailing Edge

The second trailing-edge configuration appears in Figure 2.3 a. It consists of two slits 1/16 inches high on either side of a centered foil plate, that protrudes a distance of three trailing-edge thicknesses from the trailing-edge of the plate. These slits run the width of the plate contained by the false walls. Similar reinforcements as the ones used for the first trailing-edge configuration, were placed in this trailing edge. Interest in this design was twofold. First, it falls in line with the practical desire to avoid machining a slit through the minimal trailing edge area of a fan blade. Secondly, it seeks to demonstrate the considerable increase in wake reduction noted by Park (1989), when experimenting with a double-slit configuration.

Generation of Fully-Turbulent Boundary Layer:

The purpose of the conditioning plate is to generate a fully-turbulent boundary layer before the the flow reaches the trailing-edge of the plate. Its design is based primarily on the work of Johansen (1982). The two primary design factors contributing to the creation of the turbulent boundary layers are the rows of hemispheres along the leading-edge, and the length of the plate. A diagram of the hemisphere spacing can be found in figure 2.5.

The hemispheres are laid out in nine rows beginning two inches from the leading-edge of the plate, on both the top and bottom surfaces. In reality, the hemispheres are small spheres that have been sunk into the surface of the plate such that slightly more than half of the sphere is above the surface of the plate.

The first four rows of spheres are spaced 0.375" apart (center to center) with 0.750" between the rows. The spheres are 1/8" in diameter. Their centers are positioned 0.0127" above the plate. The fifth row consists of alternating spheres of 1/8" and 5/32" diameter spaced 0.375" apart (center to center) with the continued spacing of 0.750" row to row. The centers of the larger spheres rest 0.00345" above the plate surface. The final four rows of spheres are of the larger size, spaced 0.750" apart (center to center).

In all cases, the first row of spheres along the sides of the plates is staggered so that parallel columns do not exist; that is, a space in the first row is followed by a sphere in the second row. The rows themselves are parallel.

Johansen based his work on that of Klebanoff (1955). Klebanoff established that a Reynolds Number transition criterion could be used to determine whether the spheres would trigger a turbulent flow. Klebanoff defines the

Reynolds Number as $Re=U_k k/\nu$, where U_k is the velocity of the fluid at the height of the sphere, k is the exposed height of the sphere, and ν is kinematic viscosity. Using elements of almost identical size and spacing as those used in this experiment, Johansen calculates the Reynolds number to be 490, at the first row of spheres for a channel speed of 9.88 in/s (our experiment was slightly slower, apx. 9 in/s.)

To assure transition had occurred, Johansen performed hot film experiments at three locations downstream of the leading edge. Profiles taken at 0.84 m, 1.52 m, and 2.06m downstream of the leading edge all showed the characteristics of a turbulent boundary layer.

Any possibility that the slightly slower velocity used in this experiment (of the order of 0.9 in./s slower), may invalidate the comparison with Johansen is compensated for by the length of the conditioning plate. It is a relatively safe assumption that if transition is not triggered by the hemispheres, it will be triggered by shear flow along the remaining length of the conditioning plate.

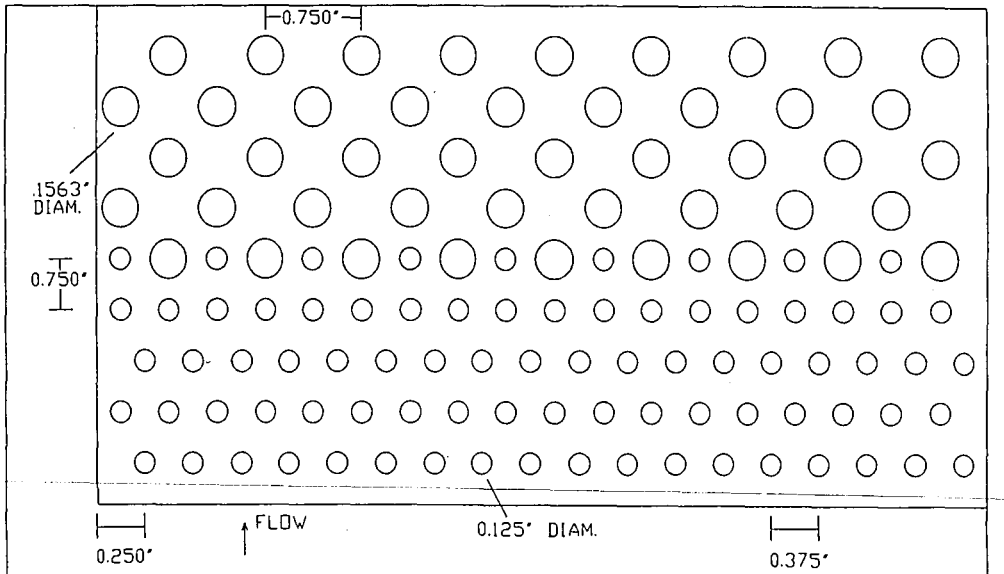

FIGURE 2.5: CONDITIONING PLATE LEADING EDGE
(Hemispheres run along the first 8" of 72" plate)

SCANNING PARTICLE IMAGE VELOCIMETRY

Particle image velocimetry has become one of the leading velocity measurement techniques in fluid mechanics today. It offers the advantage of generating a field of velocity vectors in a plane as an end product. The size, placement, and orientation of this field can be controlled easily within the bounds of the experiment. The velocity vectors generated by the process are two-dimensional, giving two velocity components at each measuring point. The advantages of producing this kind of data for use in analyzing a turbulent flow, such as the one presented in this project, are obvious.

The theory behind the technique relies on our ability to track the motion of particles suspended within the flow. In theory, if one follows the trajectory of a particle as it moves through a given distance, and the time between successive positions of the particle is known, a two-dimensional velocity vector can be generated representing the motion of the particle, and therefore the motion of the fluid that entrains it.

Working from this premise, the early work in PIV relied on two primary techniques to track particles within the flow, based on the density of the particles. Low particle density techniques relied on the tracking of individual particles, while high density techniques relied on more complicated analysis in order to track a large number of particles in the flow. Discussion here will be limited to the latter case.

Much of the crucial developmental work in particle image velocimetry can be traced back to Adrian (1986) at the University of Illinois. His early experimental apparatus utilized a pulsing laser that was spread into a laser sheet with the use of a cylindrical lens. A

photographic exposure was taken of the flow that included several pulses of the laser. Each pulse illuminates the particles at a new successive position, making the end product of this initial phase a multiply-exposed photographic negative that shows the trajectories of a large number of particles over an established period of time. The analysis of these negatives will be detailed momentarily.

The laser sheet used in these experiments was created in a different manner, although the basic principles of its use are similar to those of PIV systems using a pulsed laser sheet. The apparatus used to create the sheet appears in figure 3.1.

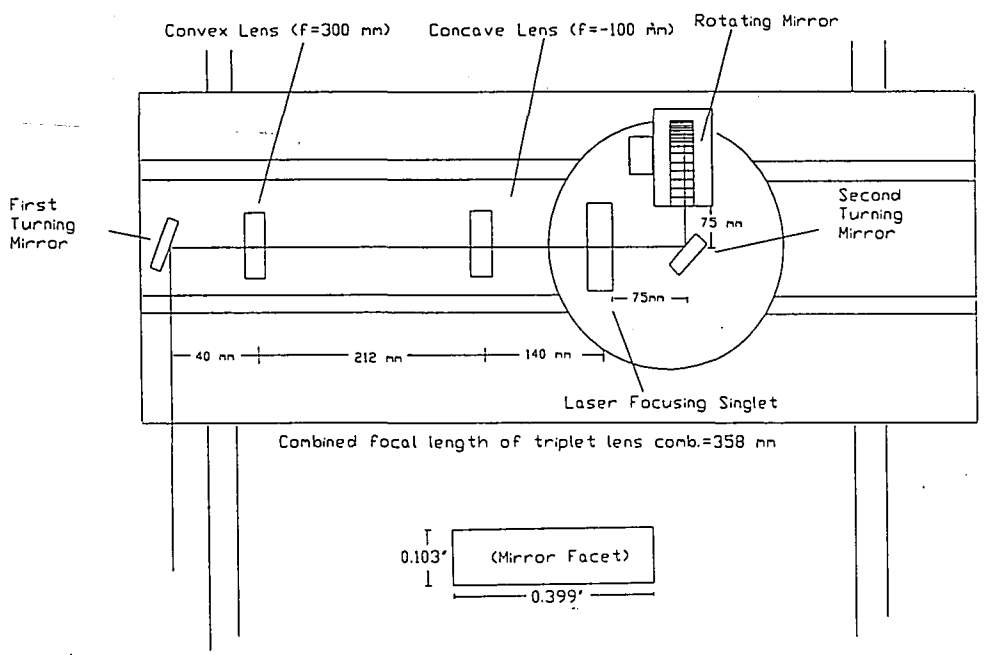

Figure 3.1: PIV Laser Table
Rotating Mirror r= 1.181"

Use of Rotating Mirror

A multi-line laser beam is generated using a LEXEL model 95A laser. The beam's power varied throughout the experiments, due to technical problems with the laser, but in general experimental power was usually in the range of 2-2.5 watts. The laser itself was approximately twelve feet from the first turning mirror that appears in the figure. All further components of the scanning system were located on a moving table that could slide on rails along the length of the water tunnel. The final lens and scanning mirror were located on rails that allowed movement across the width of the tunnel, thereby optimizing the available positions for the laser sheet.

Once the laser beam was turned by the primary turning mirror, it was collected by the triplet system of lenses pictured in the figure. The exact nature of this lens system will be explained momentarily.

Once through the lenses, the beam is directed by a final turning mirror, onto the scanning mirror device. The scanning mirror device is a 72 sided mirror with dimensions shown in figure 3.1. The mirror was constructed by Lincoln Laser Corp. of Phoenix, AZ, and used for the first time with this type of PIV experiment. When the laser beam is directed incident to the mirror the beam is deflected into the tunnel. As the mirror rotates, the angle of deflection of the beam is changed causing it to move in a sweeping motion. This motion continues until the edge of a facet is reached. At this point the laser beam is incident upon the end of the initial facet as well as the beginning of the next facet. For a brief period, this divides the power of the beam and projects two weaker beams into the tunnel. Finally rotation causes the far beam to disappear, and returns full power to the beam which is now entirely

incident at the beginning of the next facet. When rotated at a given speed, the mirror causes the beam to scan (each facet causes one scan so one rotation would include 72 scans). Each facet's scan begins and ends at the same point, causing a wedge of light or laser sheet, to form. This laser sheet is for all intents and purposes, of the same nature as the ones created using a cylindrical lens. The effect of having to scan the beam through the area of illumination rather than illuminating the entire area at once, is negated by the speed at which the laser beam scans. The laser scanning speed is typically two orders of magnitude higher then the flow velocity.

The rotation of the mirror is driven by a motor installed by Lincoln Laser Corp., which is controlled by one of their controllers. An external function generator was also used, due to the controller's inability to generate speeds lower than 3.5 rot/s using its internal generator. When a square wave was generated by the external generator, with an amplitude of 5 V, and fed into the external port of the controller, the rotational speed of the mirror could be significantly lowered.

A series of tests was performed in order to verify the scanning rate indicated by the motor controller. The tests were performed by setting the motor controller to a given scanning rate, and then checking the laser beam's scanning rate using a photocell and a frequency counter. See Figure 3.1 a.

The tests showed that the mirror demonstrated a respectable accuracy in maintaining its scanning rate when near, and especially above, a rotational speed of 2 rev/s. A detailed test was taken at a motor controller setting of 1.7 rev/s. It showed that the actual scanning rate of the laser varied from a maximum of 123.1 scans/s to a minimum of 122.5 scans/s. Fourteen trials were performed at

randomly spaced intervals generating an average of 122.7 scans/s with a standard deviation of .177. When compared with the relative accuracy of the controller, these values demonstrate a consistent rotational speed that agrees with the value measured by the motor controller.

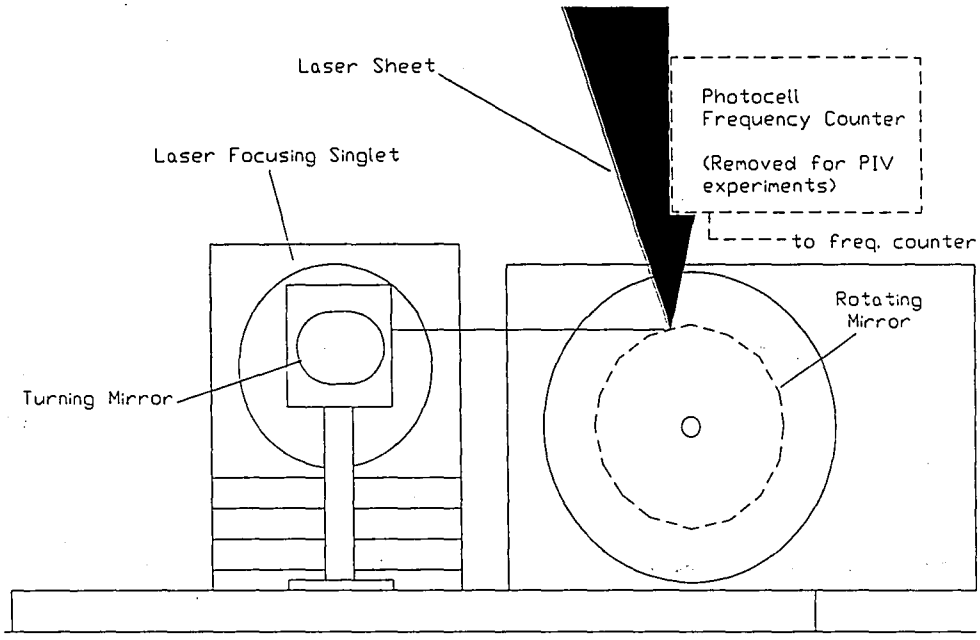

FIGURE 3.1a: END VIEW OF ROTATING MIRROR

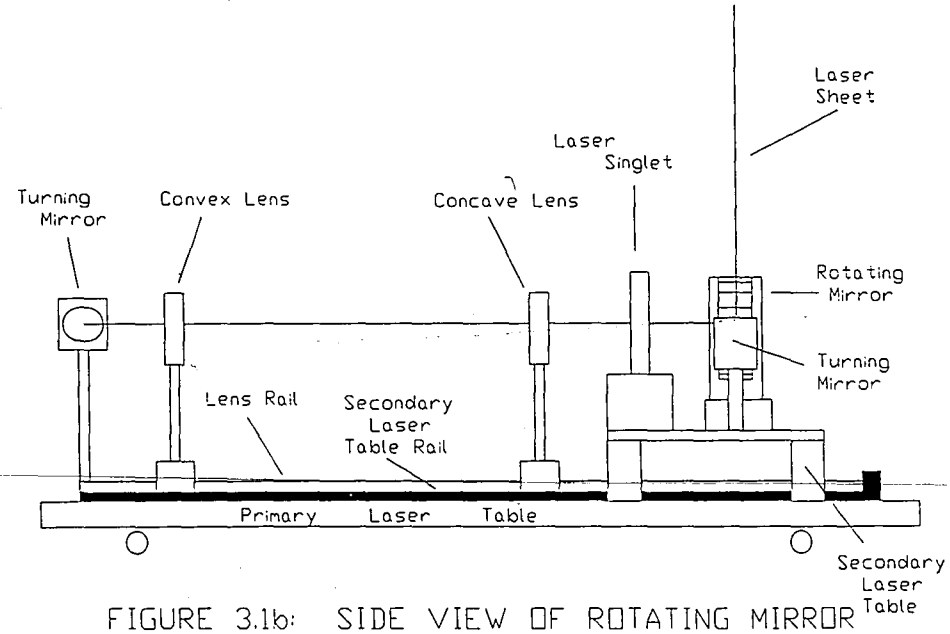

FIGURE 3.1b: SIDE VIEW OF ROTATING MIRROR OPTICAL TRAIN SYSTEM

Beam Collimation

The facets on the rotating mirror are quite small (dimensions appear in figure 3.1). In order that the mirror be utilized properly, the laser beam must be collimated to a size such that it illuminates only one facet for most of its scanning time. (The exceptional time is, of course, the point at which the beam is leaving the edge of one facet and moving onto the next.) Otherwise, illumination of multiple facets will cause the production of multiple-scanning beams, which will divide up the total light intensity. This effect is demonstrated in figure 3.2. The device is even more prone to this behavior if the beam is directed high relative to the center of the mirror. However, a high beam height relative to the center of the mirror is in general desirable, because it allows the creation of a narrower laser sheet emanating from the top of the mirror. The smaller sheet concentrates the illuminating power, and the sheet position makes its orientation easier. A lower beam creates a large laser sheet that spreads out the laser power. It also projects off of the mirror at a lower angle making it more difficult to direct into the flow.

The concepts are more easily understood when the total normal area of a facet is considered. If the laser beam is directed towards the center of the mirror, the entire area of a given facet is normal to the beam. Each facet higher than the center is 5 degrees less vertical than the one before it. It can easily be seen that facet area normal to the beam drops as the sine of that total change in angle when the beam is raised above the center position. At the top of the mirror, the facet faces up and the normal area is zero. The smaller the normal area, the harder it is to illuminate only one facet. But also, the smaller the normal

area, the smaller the range of the scan, and the higher its intensity.

One further consideration involved is the actual size of the laser beam when it enters the water channel. It is desirable to have a small scanning beam for the same reasons that it is desirable to have a small width of the scanning laser sheet, i.e. it decreases the available laser power.

Given that the laser power was limited, and that low laser light levels would restrict the possible shutter speeds available on the camera (affecting the critical aspect of image spacing, to be discussed later), it was necessary to collimate the beam as much as possible. Previous systems incorporated with other scanning devices used one of two optics concepts: 1) a telephoto lens combination of a convex lens followed by a concave lens (Magness, 1991); or (2) a Laser focusing singlet (Towfighi, 1992). (See Melles-Griot product 01 LFS 027).

The telephoto combination allowed adjustable collimation of the beam by alteration of the relative spacing between the two lenses. Unfortunately, once the beam was collimated close enough to the mirror to be effective, it began to diverge again and was quite wide by the time it entered the water channel.

The laser singlet could be acquired only with a focal length of 0.9 m, which meant that focussing of the beam could not be executed until far past the surface of the rotating mirror. Multiple beams were almost always present. Structural difficulties discouraged the placement of the singlet before the first turning mirror.

The obvious solution was the combination of both lens systems. The lens arrangement is noted in figure 3.1. The telephoto arrangement offers quick collimation, while the singlet assures that the beam retains intensity as it

passes into the tunnel. The series used involved a symmetric convex lens (f=300), followed by a symmetric concave lens (f=-100), then a laser-focusing singlet (f=900). The distances between them appear in the figure. The combination focal length for the three lens system was 357.6 mm. Information used to design the optics configuration was obtained from the Melles-Griot Optics Guide 5 (1991). The calculations done are detailed in Appendix A. Using this optical arrangement a small laser sheet was generated from a position high on the rotating mirror. The triplet configuration allowed shutters speeds as fast as 1/125 of a second vs. 1/30 of a second with the telephoto combination. No successful tests were ever performed using only the singlet.

Particles

The water tunnel was seeded with metallic-coated spheres with an approximate diameter of 9 μm. The spheres used were purchased from TSI corp. (Model 10087, ρ=2.6 gm/cm^3). The nature of the particulate matter used tends to depend on the researchers involved. Experimenters have had luck with particulates ranging from hydrogen bubbles (Welsh, 1990) to conifer pollen (Gray, 1987). The nature and size of the particles is quite crucial to the veracity of the results. Adrian and Yao (1985) discuss the effect of seed materials on the results obtained using the PIV technique. With respect to size, they suggest the following: although images of larger particles are easier to detect, images of smaller particles are more desirable. The smaller the particle, the larger the increase in accuracy in the velocity measurements, and the better the spatial resolution. Adrian suggests particles in the range

of 0.5 μm -10 μm, with a suggestion of 10μm for water use. Particles smaller than this are hard to detect on film. Particles larger than this add error due to diffraction effects caused by the large particle sizes.

Surface coatings on the particles also vary. Particles with fluorescent coatings have been used on a small scale within Lehigh's facilities with some success. Several different coatings have been tried in the past with the most success having been obtained with the TSI particles. The only drawbacks involved with the use of TSI particles are their deviation from neutral buoyancy (ρ=2.6 gm/cm^3), which causes them to sink slightly over long distances at low velocities, and their cost which requires restricted use.

Interrogation Technique

All previous techniques mentioned are implemented in order to optimize the next stage of the PIV technique known as interrogation. This procedure involves the actual analysis of the photographic negatives in order to obtain a velocity vector field.

The interrogation procedure will be outlined briefly here. A more exact reprise on the subject appears in Appendix B. The interrogation procedures used for high density PIV techniques, such as the one detailed here, usually rely on the use of two-dimensional autocorrelation techniques, or a Young's fringe technique. The Young's fringe procedure was used within the Lehigh interrogation system.

The procedure analyzes photographic negatives produced

through the procedures already outlined. The experimental technique used must be varied in order to obtain negatives that can be analyzed by the system and produce accurate results. One of the crucial aspects to be considered is the spacing between successive particle images on the negative. The spacing itself must be within a small range that will assure proper spacing between the generated fringes. Images that are too far apart will produce fringes that are too close together for the computer to analyze, while images that are too close together will produce solitary or otherwise over spaced fringes. No general rule or guide exists for obtaining the proper spacing other than examining past successful results.

The choice of spacing is influenced by three factors: (1) shutter speed; (2) beam scanning rate; and (3) water channel speed. Control of shutter speed is obtainable only if a reasonable amount of laser light is available. Otherwise slow shutter speeds must be used to allow for proper exposure. By varying the shutter speed and scanning rate, a proper spacing often can be found. Beyond the consideration of having the proper spacing of particles, the overall length of the particle trajectory recorded must also be considered. The velocity vectors generated represent the average velocity over the recorded trajectory of a single particle. We must therefore restrict the length of the trajectories recorded in order to obtain accurate results. This can again be controlled using alteration of shutter speed, and is a further factor that makes a faster shutter speed desirable. For a correct particle spacing, a track including 3 to 4 particle images is usually optimum.

The final factor is the actual speed of the fluid. High water speeds were necessary for this experiment in order to assure the transition to turbulent flow. The

higher speeds obviously affect particle spacing. A more difficult problem arises when two flows with greatly varying speeds exist within the same field. It is quite difficult and often impossible to adjust the parameters of the experiment to obtain reasonable results. One device often used to counter this problem is a biasing mirror. The mirror is placed in front of the lens with the desired image reflected onto it. The mirror is turned using computer control so that it adds a bias to particle spacing in the photo.

Once suitable photographs are chosen they can be analyzed using the interrogation apparatus that appears in figure 3.3. The software to drive this system was purchased from Fluid Flow Diagnostics. The negatives are placed in the mechanical traverse. The traverse is computer-controlled so that the negative can be examined on a small piece by piece basis. A small HeNe laser illuminates a small circular area of the negative. Inside that area there are particle images and spaces between them. The relative orientation of the images causes an interference pattern behind the negative. This interference pattern takes the form of Young's fringes once the image has been transformed by an optical Fourier lens. The image is collected by another lens and pictured by the video camera. The computer program PDV digitizes these fringes with the help of a frame-grabbing board. A two-dimensional Fourier transform then brings the fringe pattern back into an analyzable form which provides a two dimensional velocity vector corresponding to that region on the negative. Again much more detail on the interrogation procedure is provided in Appendix B .

The computer scans the entire negative using two high resolution Klinger stepping motors that control the movement of the traverse. A typical detailed scan would

typically search a 25 X 22 mm negative using a 50 X 44 point grid.

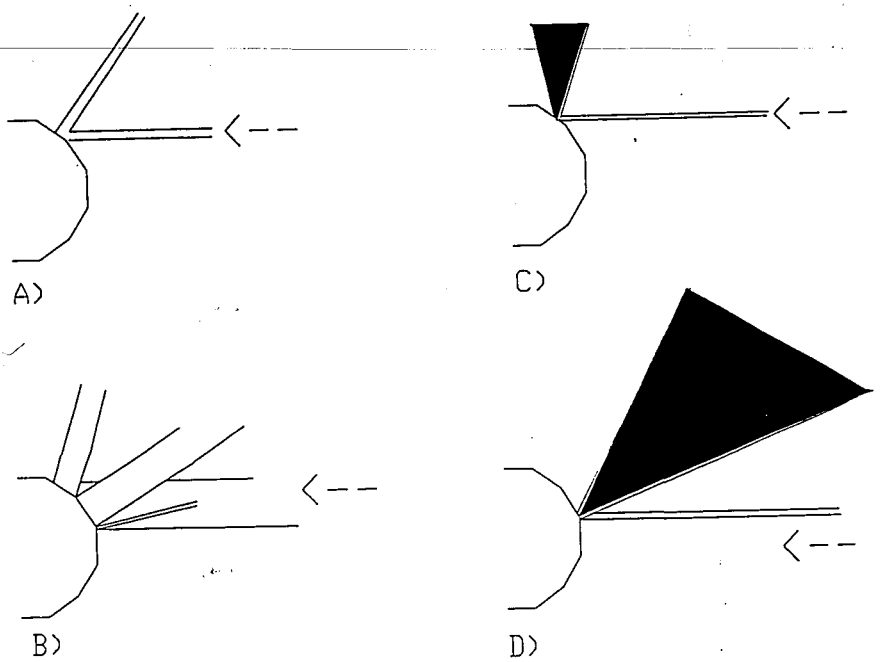

FIGURE 3.2: (A) and (B) show contrasting effects of small and large incident beam (C) and (D) show contrasting effects of beam position

A series of programs is executed after the initial interrogation. CVPIV by Robinson and Magness (1991), transforms the data into viewable information. The program V by Robinson (1991) allows the vector field to be viewed and manipulated. Included within these manipulation procedures is the opportunity to discard errant vectors. Program V also includes a biasing system that can subtract a given amount off of the velocities of the entire vector field. This is particularly useful for bringing out the turbulent characteristics of a flow which normally amount to only a small percentage of the mean flows in experiments similar to ours. PLOT (Golden Software, 1988) can take a plot file from V and create a suitable plot file for use on the many printers. Program FILV (Robinson and Magness, 1991) can be used to fill in any spaces where sufficient fringes were not found. It fills in gaps using

interpolation of surrounding vectors, and is inappropriate if large sections cannot be interrogated. FILV also generates grid files that can be converted into vorticity contours. (Usually done with SURFER, Golden Software, 1989.)

Previous-related Investigations:

Given the above established procedures for PIV analysis we can examine some previous uses of the technique. At Lehigh, much of the pioneering work was done by Magness (1991). His doctoral thesis involved the analysis of flow over a delta wing, and includes detail on many of the techniques mentioned above. Most of the computer analysis techniques were compiled by Magness and Robinson during Robinson's post-doctoral work. Further study continues at Lehigh using the technique to examine further delta wing experiments and experiments involving various cases of oscillating cylinders.

Outside Lehigh, a very relevant case of the use of PIV for measurement of turbulence within a channel flow is presented by Liu, Landreth, Adrian, and Hanratty (1991). The paper details use of the PIV technique, as well as detailing velocity field results. This paper also introduces the concept of using the ensemble average of a small number of interrogated images (10-12) in order to obtain reasonable mean and turbulent quantities. The data for a turbulent flow are presented in detail. The low number of samples can be justified by the amount of detail provided in each sample. The assumptions are confirmed by the use of Laser Doppler Anemometer. The use of a small number of averaged images is crucial to the analysis done for this thesis and is discussed again within the section entitled Use of Taylor's Hypothesis and Program

Fandango.

Further examples of the use of PIV can be found in the work of Gray (1987) in problems such as the analysis and study of water waves, as well as in the work of Welsh (1990) for many flow cases. Other referenced sources include Keane et al (1989), Landreth et al (1986), and Liu et al (1991).

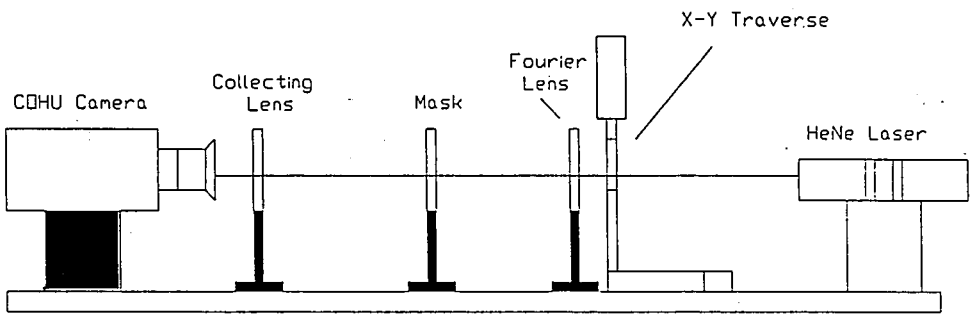

FIGURE 3.3:
Interrogation Apparatus

USE OF TAYLOR'S HYPOTHESIS AND PROGRAM FANDANGO

As stated previously, the Particle Image Velocimetry technique yields a two dimensional field of velocity vectors. An example of this output can be seen in figure 4.1. The intention of this section is to illustrate a means by which this field data can be used in order to obtain turbulence information on the flow.

Taylor's Hypothesis (Tennekes and Lumley, 1972) allows an equivalence between measurements made in space and time. The analogy assumes that the structure of the turbulence is "frozen" over the length of the measurement.

Figure 4.1 depicts the original output from a PIV interrogation. Averaging the velocity vectors along each of the rows of the diagram can be done, in order to obtain horizontally-averaged and therefore analogously time-averaged velocity data using the assumption of Taylor's hypothesis. The data can then be ensemble-averaged with similar data from other PIV interrogation frames in order to generate turbulence information.

Program FANDANGO (Redi and Corcoran 1991) was designed to accomplish this task. The program reads in files representing the vectors contained within the PIV interrogation frames and averages them along the rows of the frame. It then averages successive files together. The output consists of several files, each with the original number of rows, but now containing a single averaged column of specific data. Files generated include average the velocity U, u_{rms}, v_{rms}, and $\overline{u'v'}$. The listing of the program is included in appendix C.

An averaged set of data includes an average of 50 points per row, per file, times a usual twelve files, giving us the equivalent of 600 instantaneous measurements, per row of data, for determining the time-averaged value.

A similar technique is used by Liu et al (1991). The technique is used to analyze the turbulence within a fully-developed channel flow. The turbulence quantities generated are similar to the ones generated by program FANDANGO. Included is a verification of the technique performed by comparison of the PIV turbulence data with turbulence data taken with Laser Doppler Velocimetry. Comparison is also made with a computer simulation. The comparison showed a very close agreement between measurements taken by the two velocimetry methods. The study also demonstrates the ability of the PIV technique to resolve the smaller turbulent structures within a flow.

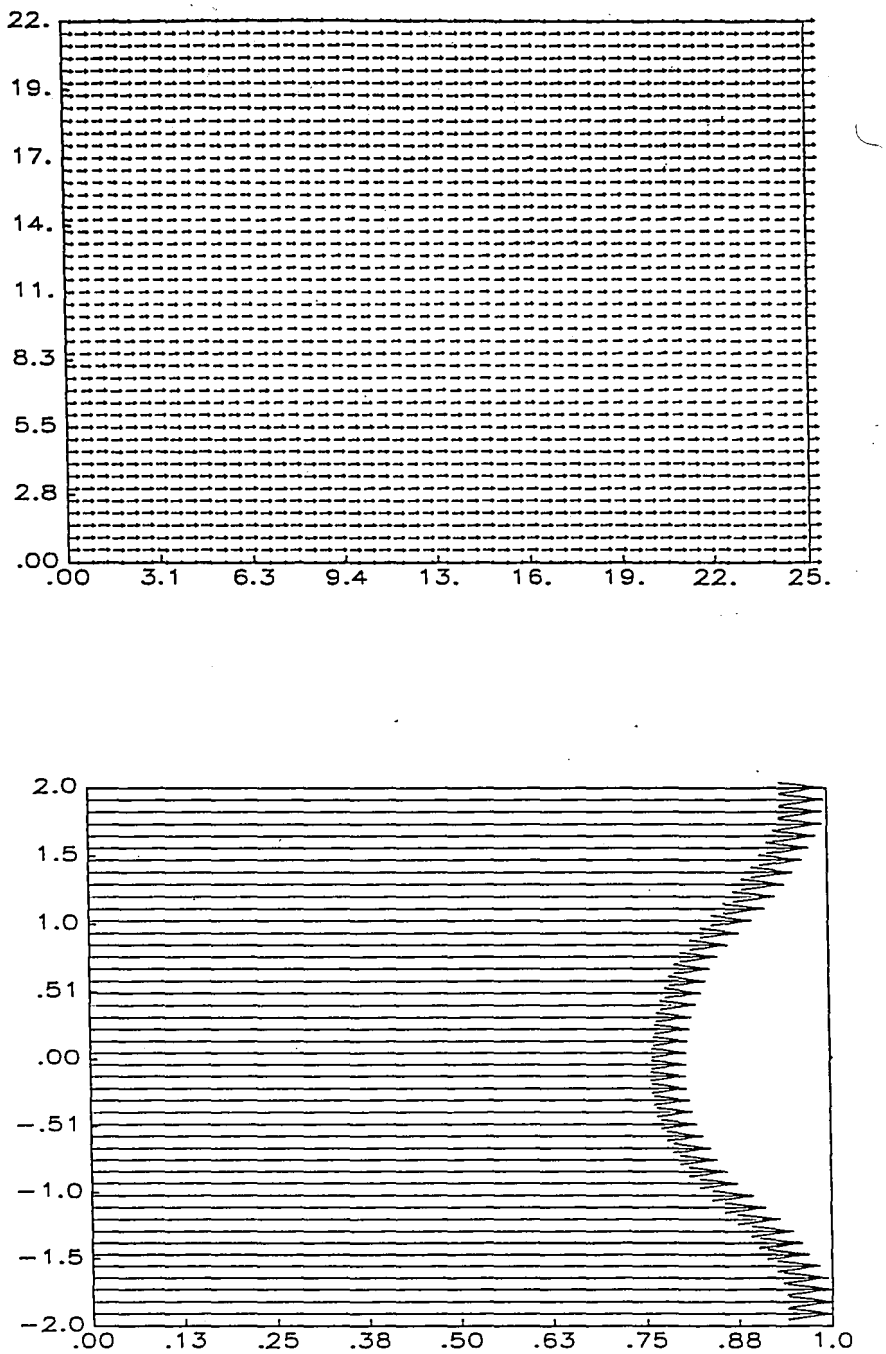

FIGURE 4.1: The upper image represents an initially unbiased output from a PIV experiment. The ordinates represent (arbitrary) vertical and horizontal scales. The lower image represents an average of 12 images created by FANDANGO.

EXPERIMENT 1--EXAMINATION OF ZERO BLOWING CASE

If no fluid is ejected from the (single) slit of trailing-edge #1, the experiment becomes simply that of the wake generated from a flat plate with a turbulent boundary layer at its trailing edge. The purpose of this first experiment is to compare the wake data with wake data from a rotor blade in previous experiments. This is a necessary step to verify that our experimental apparatus will indeed generate a wake similar to that of a rotor blade, thereby validating the basic approach.

The approach that we will concentrate on is that of Majjigi and Gliebe (1990). In that work, the objective was to develop a wake model of a rotor blade by investigating the extensive empirical data available on the subject. Most of the data used in compiling the model were gathered from two experiments. The first involved Tri-axial hot wire measurements done on a twelve-blade rotor (blades: British C-1 profile), and the second was a similar experiment done on a 21 blade rotor (blades: NACA 05-018 profile). The exact citations for the work can be found within Majjigi and Gliebe (1990) . These works are, in turn, used by Majjigi and Gliebe, in order to generate several models for the wake deficit of a rotor blade. These models will be used in order to validate the current experiments.

The details of the current experiment will now be presented. The single-slit trailing edge was fitted into the experimental apparatus as detailed in the Experimental Apparatus section of this thesis. A 35mm camera (Nikon F-4, with a 55mm lens), was positioned to take a photograph that began 5 ft. downstream of the trailing-edge of the plate. The frame of the camera included an area 7.08 in. (18 cm) x 8.05 in. (20.45 cm). The scanning rate of

the rotating mirror was set at 266.4 scans/s (3.7 rot/s). With a camera shutter speed of 1/60 s, this resulted in 4.44 images per particle to be captured on each frame. The aperture used was 2.8. The water tunnel speed was set at apx. 9 in/s (maximum). All of the above quantities were previously decided upon after tests to optimize available light and particle spacing.

Twelve photographs were taken with time intervals between shots of approximately 10 seconds. The photographic negatives were interrogated by the standard method detailed previously, and their results combined using program FANDANGO (see previous section of same name.) Data of U(y), $u_{rms}(y)$, $v_{rms}(y)$, and $\overline{u'v'}(y)$ were found. Only that of U(y) will be presented in this section. The rest will be presented in subsequent sections.

The data were normalized in order to agree with the form of Majjigi and Gliebe (1990). The normalizations used within that work correspond to most other works on the subject. The horizontal scale is normalized by the half width distance, l, as detailed in the theory section of this thesis (See Tennekes and Lumley, 1972). The vertical scale is the velocity deficit U_s (here called U_d to agree with Majjigi and Gliege), normalized by the maximum velocity deficit U_{dc}. This maximum velocity deficit is found at the center of the wake.

Figure 5.1 presents the first model proposed by Majjigi and Gliebe (1990), labeled in the figure as NASA (due to their sponsorship). The model is based on a Gaussian curve fit of their included data. The fit corresponds the following model:

$$U_d / U_{dc} = \exp(-\eta^2 \ln(2)), \qquad (1)$$

where η is the normalized distance, y/l.

This model is based on a classical analysis presented in Tennekes and Lumley (1972), pp. 117. The model presented therein uses a coefficient of 0.5 rather that the ln(2) used above. The Tennekes and Lumley model is based on a simplified analysis; this model is compared with experimental data. The coefficient, the natural log of 2, used in (1) reflects attempts to compensate for the discrepancy between model and experiment. The data generated within these experiments are designated by the symbols on the graph of the model. The correspondence with the unmodified model is generally good with slight deviations easily noted towards the edges of the wake. A Gaussian curve fit was performed on the data in order to generate a coefficient similar to those employed in the two above models. The fit specified a coefficient of 0.71765.

A second model proposed by Majjigi and Gliebe used a hyperbolic secant to model the flow. This model showed a smaller standard deviation from their data than their Gaussian model. The formula for the model is as follows:

$$U_d / U_{dc} = \frac{1}{\cosh(1.3169579\eta)} \qquad (2)$$

where η is y/l.

The second model appears in figure 5.2 along with the data of the present experiment. Also appearing on this figure is a fit of our data to a hyperbolic secant function. This fit gave a coefficient of 1.38546 vs. 1.31695 as seen in the above model.

In general, the results obtained within these experiments justified further use of the experimental rig

as a simulation of an active rotor blade. Slight deviations from the models presented can be noted. This may be due the lack of data generated in this experiment in the regions beyond two half-widths from the center of the wake.

Further comparisons can be made between the present work and that of Chevray and Kovasznay (1969). Their experiment involved measurements taken downstream of a 50cm wide by 240cm long plate in a wind tunnel. The plate was 0.160 cm thick. The last 60cm of the plate was milled so that the thickness of the trailing edge was 0.025cm. Coil springs were mounted on the plate at 30cm from the leading edge in order to generate turbulence. The Reynolds number at the trailing edge, based on boundary layer thickness, δ, was 1.5×10^4 for all tests. Measurements were made using a hot wire anemometer from a point near the trailing-edge to a distance 7.88 ft. (240cm) downstream of the trailing-edge. The comparisons made within this section involve measurements made 4.90 ft. (142cm) downstream of the trailing-edge

Comparisons between the fluctuating velocities and the Reynolds stresses obtained in this work and those found by Chevray and Kovasznay appear in figure 5.3. It was assumed that the great difference in thickness between the two plates used would prevent exact comparison. Instead we seek to compare the general shapes of the curves by normalizing each quanity by its maximum value and each distance by the location of the variable's maximum value.

Given this unusual method of comparison, we do see reasonable agreement between the shapes of our results and those of Chevray and Kovasznay. Discrepencies, such as the deviation of the u_{rms} values near the center of the wake are most likely effects caused by the different degree of development of the wake as it evolves in the streamwise direction.

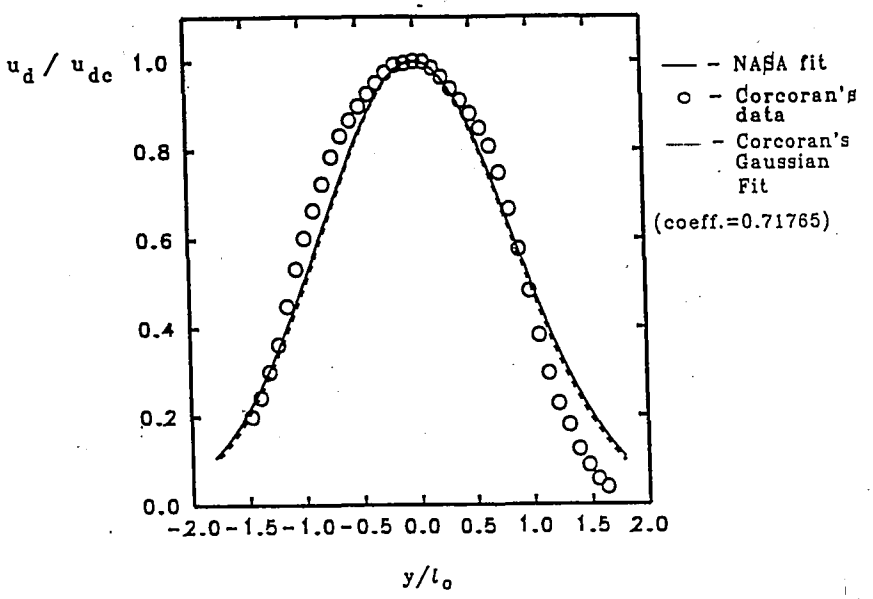

FIGURE 5.1: Gaussian rotor blade wake model proposed in NASA study (Majjigi and Gliebe, 1990) vs. data taken from blunt trailing-edge model used in the present experiments. NASA model appears in eqn. (1).

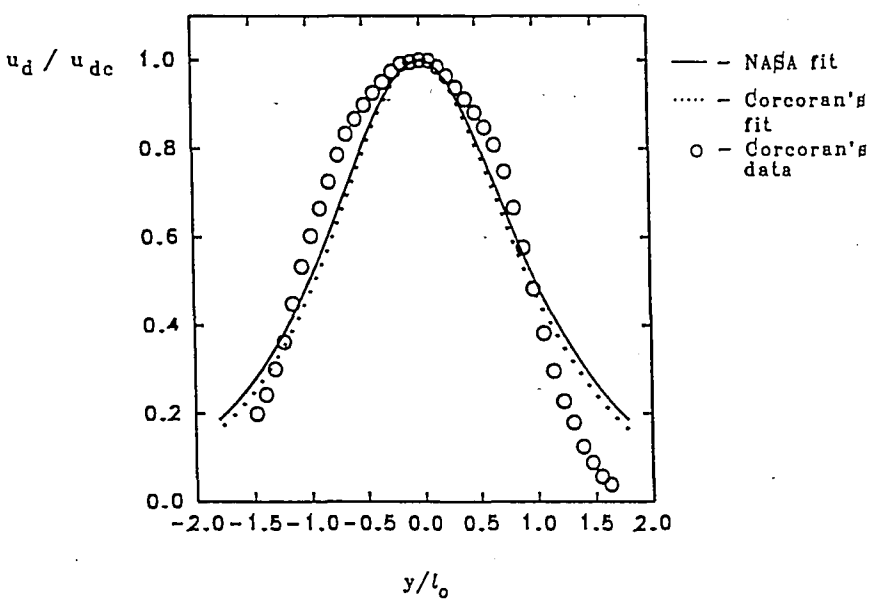

FIGURE 5.2: Hyperbolic secant model of rotor blade wake. Figure includes NASA (Majjigi and Gliebe, 1990) model as well as data gathered from the trailing-edge employed in the present study, and a hyperbolic secant fit of the data. NASA curve corresponds to eqn. (2).

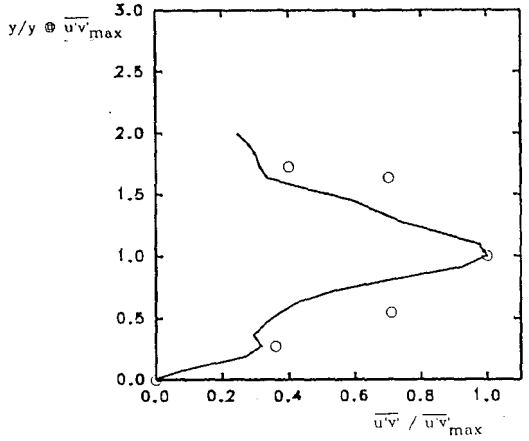

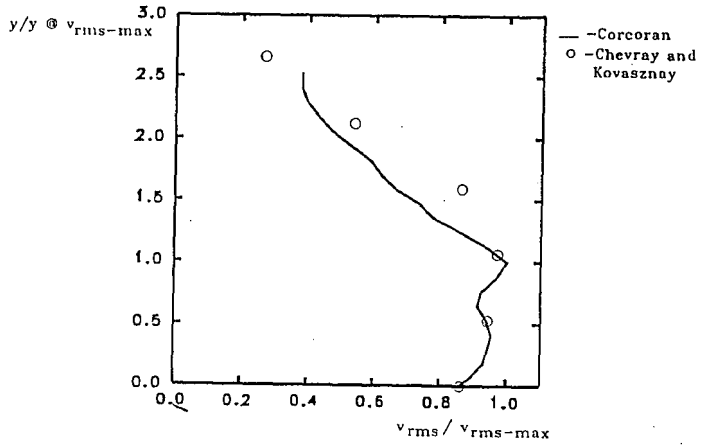

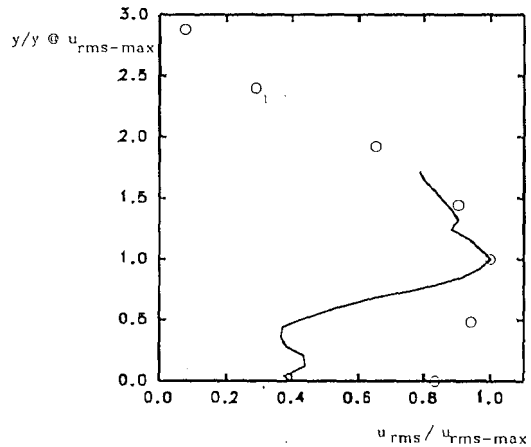

FIGURE 5.3: Comparsion of data between the present work (solid lines) and Chevray and Kovasznay (point data). Data are normalized by maximum value and position of maximum.

EXPERIMENT 2: SINGLE-SLIT TRAILING-EDGE WITH BLOWING

Assuming the results from experiment 1 justify fully the use of the proposed apparatus, the next logical step becomes the examination of the wake structure using varying rates of trailing-edge blowing. The volume rate of blowing needed to obtain a momentumless wake was determined by Naumann (1992) in some early hydrogen bubble work. The fluid velocity corresponding to this volume rate is designated as V_j^*. The actual blowing rate for a given experiment will be designated as V_j. In this experiment results were gathered at V_j/V_j^*= 0, 0.25, 0.50, 0.75, 1.00, and 1.25.

For each blowing rate the following data will be reported: U, u_{rms}, v_{rms}, and Reynolds stress. The vertical axis in all these cases will represent the vertical distance from the centerline of the wake, normalized by the half-width of the wake corresponding to zero-blowing, l_0 (see theory section for a detailed explanation of the half-width). Magnitudes of the Velocity fluctuations u_{rms} and v_{rms} will be indicated along the horizontal axis and normalized by the freestream velocity U_∞. This freestream velocity actually corresponds to the highest velocity on either side of the wake. The local value of mean velocity U will be normalized by U_∞ in a similar manner; in this case however U_∞ will be the average of the velocities taken at the upper and lower edges of the wake. This different representation was used to obtain a slightly more accurate approximation of the wake, and will not substantially affect results. The difference between the velocities on the upper and lower side of the wake was of the order of 3% percent of the average value of U_∞. Reynolds stress will be normalized by U_∞^2, where U_∞ is derived in a similar manner to u_{rms} and v_{rms}.

Instantaneous vorticity and velocity fields will be examined as well for the cases V_j/V_j^* = 0, 0.50, 1.00, and 1.25. The x and y locations in these fields will be presented in terms of normalized distances x/l_o and y/l_o.

The same experimental techniques were used for experiments 1 and 2. The field of view was centered on the vertical center of the trailing edge, and placed 5 ft. downstream of the trailing-edge. All optical/laser settings were identical to experiment 1.

At the freestream velocity of approximately 9 in/s, the following blowing rates were used for a cross-sectional area A of the slit of 1/32" x 16" = 1/2" sq.:

V_j/V_j^*=0.00	Q=0.00 gal/min	V_j=0.00 in/s	V^2A=0.00 in^3/s
0.25	1.33	10.2	52.0
0.50	2.65	20.4	208
0.75	3.98	30.6	468
1.00	5.30	40.8	832
1.25	6.63	51.1	1305

Figures 6.1 - 6.6 show the mean velocity profiles at the six different blowing rates. Figure 6.1 shows the case of zero blowing. The zero blowing wake deficit is approximately 15%. Figure 6.2 shows the velocity deficit profile for a V_j/V_j^* = 0.25. A small decrease of the deficit can be noted relative to the case of V_j/V_j^* = 0. No further decrease is noted until V_j/V_j^* = 0.75. It is quite interesting to note the sudden decrease of the deficit that occurs, shown in figure 6.5, for the case of the the momentumless wake. Although a small deficit remains, the reduction in the deficit between V_j/V_j^*=0.75 - 1.00, is by far the largest reduction noted. In fact, it represents a deficit reduction several times the size of the total reduction in the range from $V_j/V_j^* \leq 0.75$. Figure 6.6 shows how quickly the wake takes on the

characteristics of a jet as the blowing rate is increased.

Figure 6.7 shows the typical u_{rms} and v_{rms} profiles that one expects for the flat plate with no blowing. There is little change in the either u_{rms} or v_{rms} as the blowing rate increases to $V_j/V_j^*=0.25$. For higher rates of blowing, v_{rms} shows a gradual decrease as the blowing rate rises until $V_j/V_j^*=0.75$, while u_{rms} remains fairly constant (figure 6.10). At this point, one of the peaks of the u_{rms} seems to drop off suddenly. As the momentumless wake is achieved (figure 6.11), both curves suddenly flatten. A small increase of blowing above this value causes u_{rms} to increase dramatically and take the form typical of a jet flow.

The zero-blowing Reynolds stress (figure 6.13) appears as would be expected for a flat plate (see Chervay et al, 1969). The decrease in Reynolds stress $\overline{u'v'}$ with an increase in blowing rate occurs gradually. This distribution of $\overline{u'v'}$ does show some slight, unexplained asymmetry. When blowing corresponds to the momentumless case is applied, the magnitude of $\overline{u'v'}$ nearly goes to zero (figure 6.17). Application of blowing in excess of this value shows, in figure 6.18, the reversal of the sign of $\overline{u'v'}(y)$, typical of a jet flow.

Figure 6.19 shows instantaneous vorticity fields at various blowing rates. The level of vorticity increases from the outside contours to the inside ones. So a "higher mountain" represents an area of larger vorticity. The sign of the vorticity can be determined by noting reference numbers marked along various contours. The lowest number represented on the outside most contours is a vorticity level of 0.1. The method of generation of these contours is mentioned previously in the section on Particle Image Velocimetry. It should be emphasized that these plots represent instantaneous levels of vorticity (one photographic frame), and do not represent averaged values.

For V_j/V_j^*= 0.50 the mean vorticity of the flow dominates. As the momentumless wake is attained, the concentrations of vorticity suddenly disappear. The flow itself appears practically undisturbed. Vorticity concentrations typical of a jet flow appear as the blowing rate is increased.

Figure 6.20 show instantaneous velocity fields at several blowing rates. A bias equal to 0.78 U_∞ has been subtracted from the field so that the wake structure can be examined. For the case of zero blowing, a fairly narrow wake structure is apparent. The wake shows a wave-like structure along the boundary between the higher and lower speed flows. This structure can easily be seen during experimentation. An increase in blowing to V_j/V_j^*=0.50 causes an apparent widening of the wake. The momentumless wake, V_j/V_j^*=1 shows an approximation to uniform flow. The jet flow case, V_j/V_j^*=1.25 shows vectors corresponding to higher velocity along the centerline of the flow as expected for jet flow.

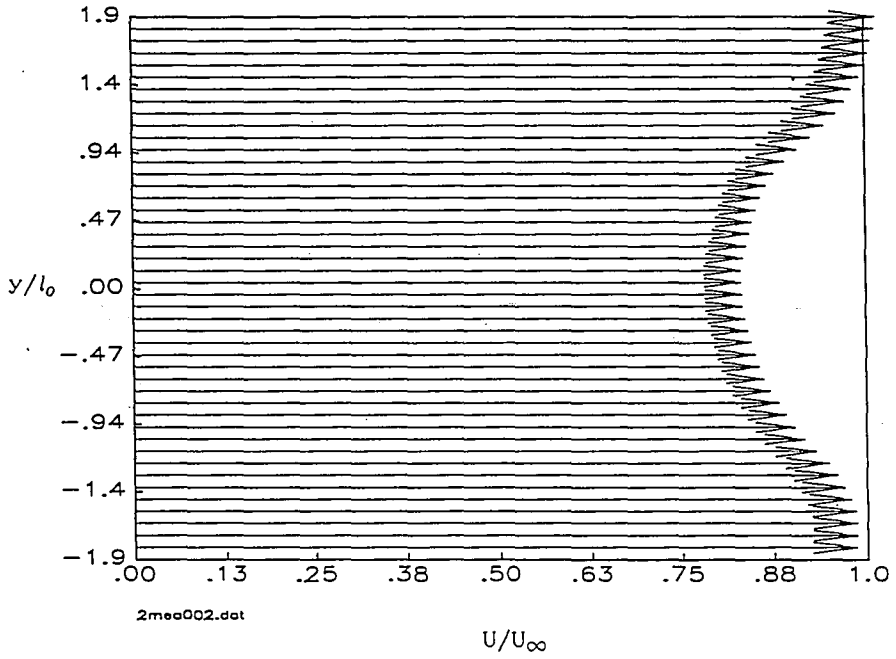

FIGURE 6.1: Normalized Velocity Profile for single-slit trailing-edge (#1) with no blowing.

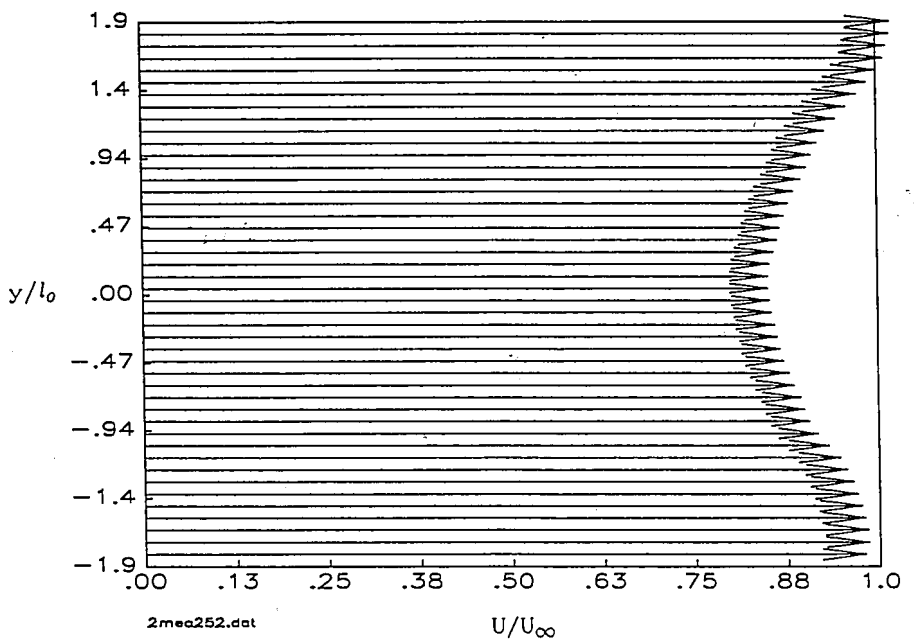

FIGURE 6.2: Normalized Velocity Profile for single-slit trailing-edge (#1) with blowing rate approximately 25% of that needed for a momentumless wake.

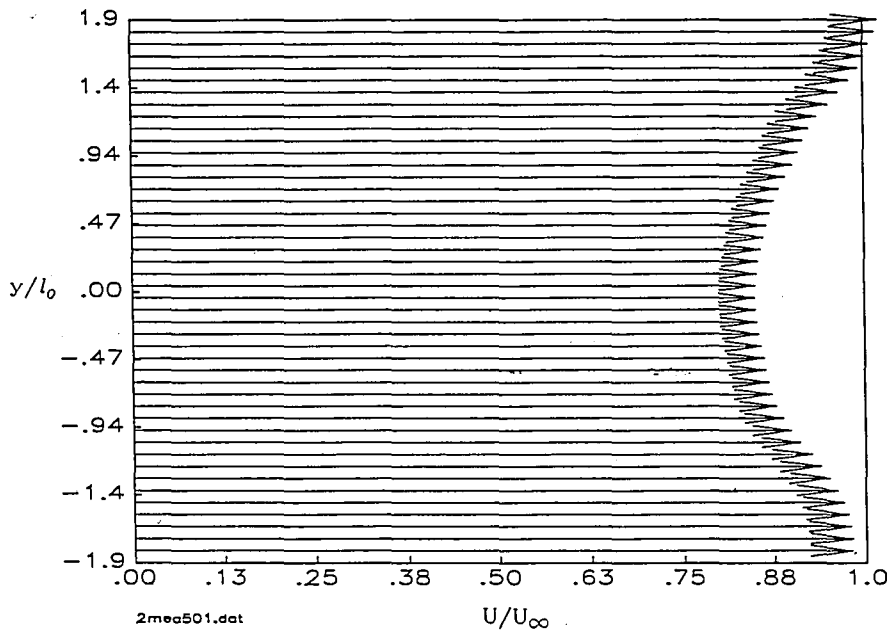

FIGURE 6.3: Normalized Velocity Profile for single-slit trailing-edge (#1) with blowing rate approximately 50% of that needed for a momentumless wake.

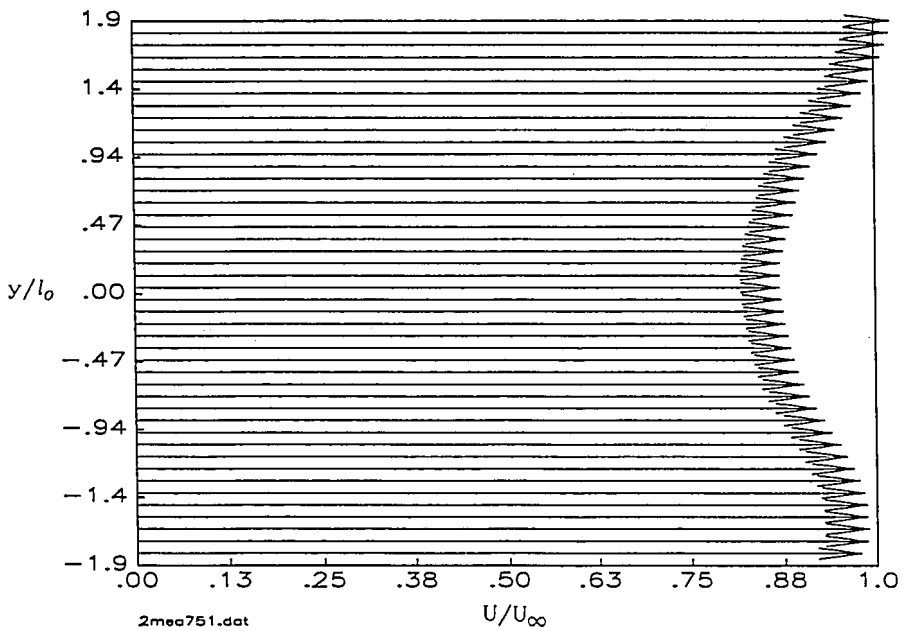

FIGURE 6.4: Normalized Velocity Profile for single-slit trailing-edge (#1) with blowing rate approximately 75% of that needed for a momentumless wake.

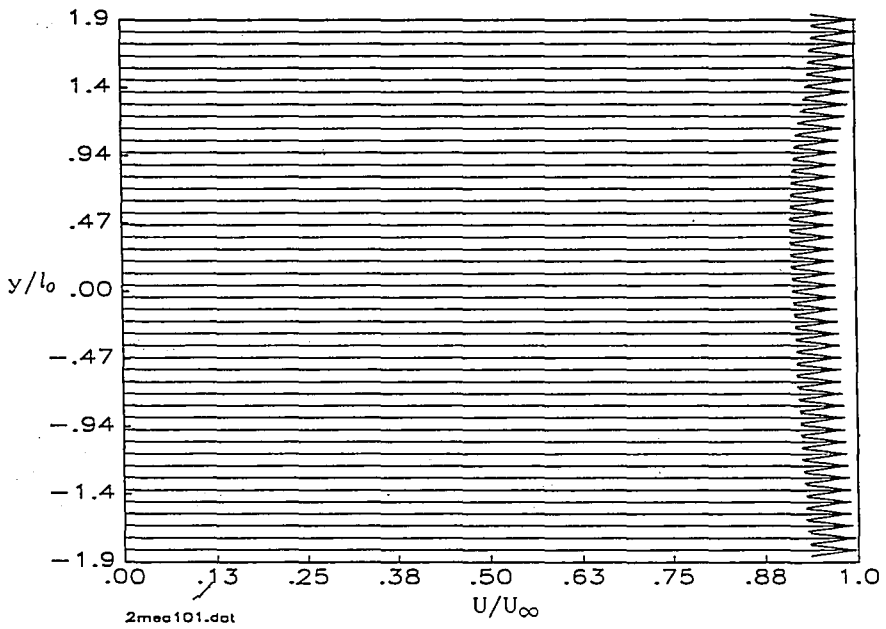

FIGURE 6.5: Normalized Velocity Profile for single-slit trailing-edge (#1) with blowing to generate a momentumless wake.

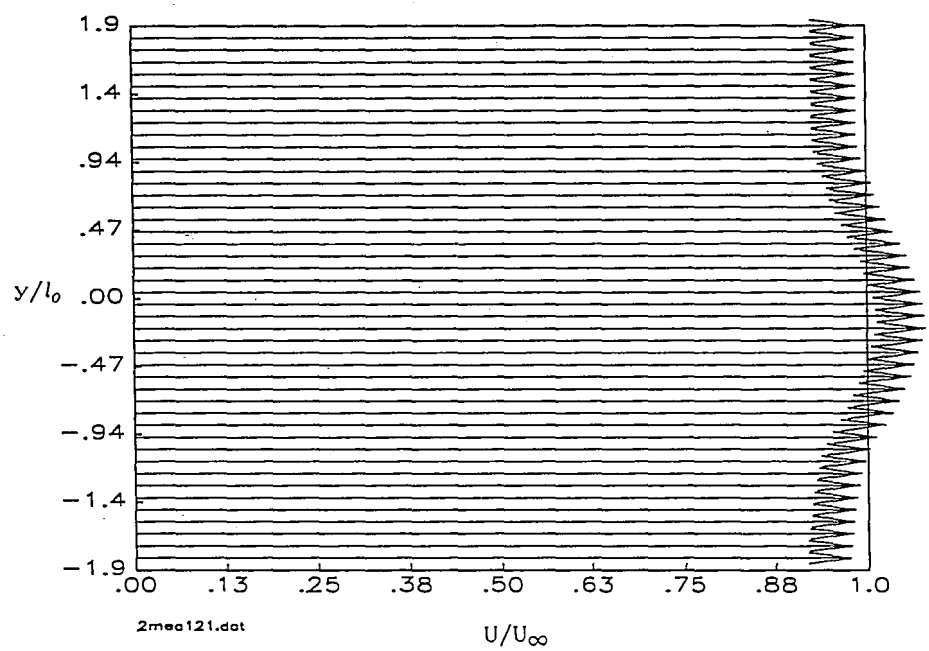

FIGURE 6.6: Normalized Velocity Profile for single-slit trailing-edge (#1) with blowing approximately 125% of that needed for a momentumless wake.

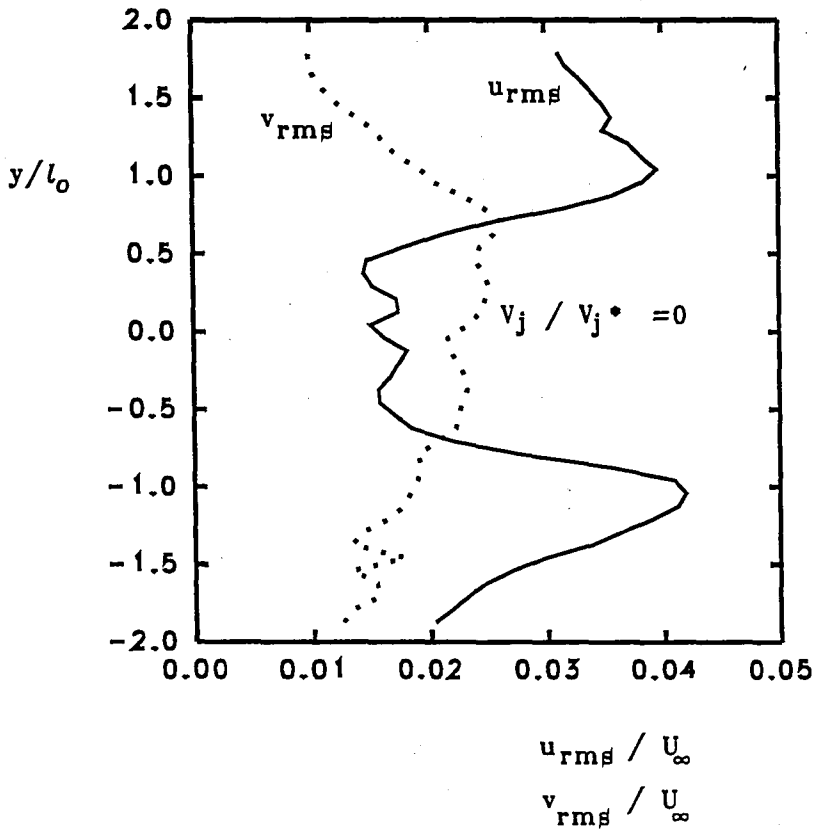

FIGURE 6.7: Normalized u_{rms}, v_{rms}, for single-slit trailing-edge (#1) with no blowing.

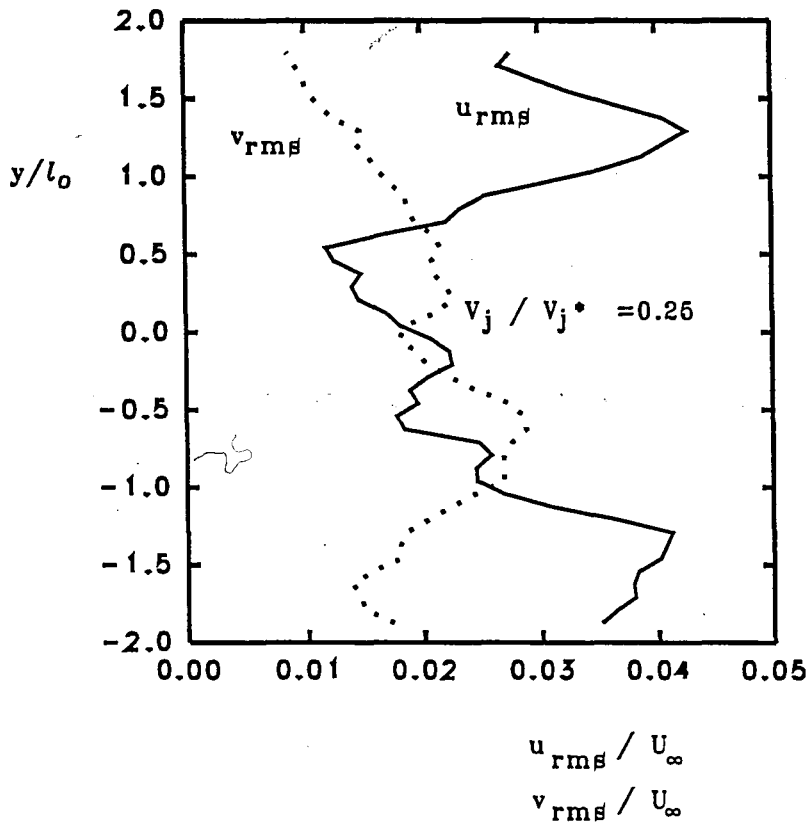

FIGURE 6.8 Normalized u_{rms}, v_{rms}, for single-slit trailing-edge (#1) with blowing approximately 25% of that needed for a momentumless wake.

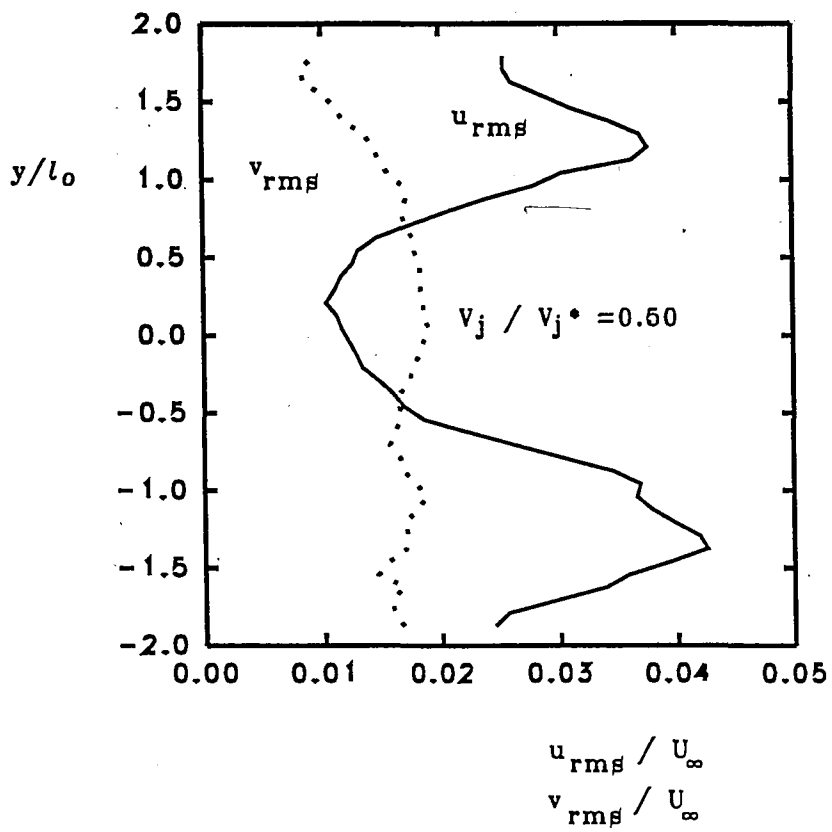

FIGURE 6.9: Normalized u_{rms}, v_{rms}, for single-slit trailing-edge (#1) with blowing approximately 50% of that needed for a momentumless wake.

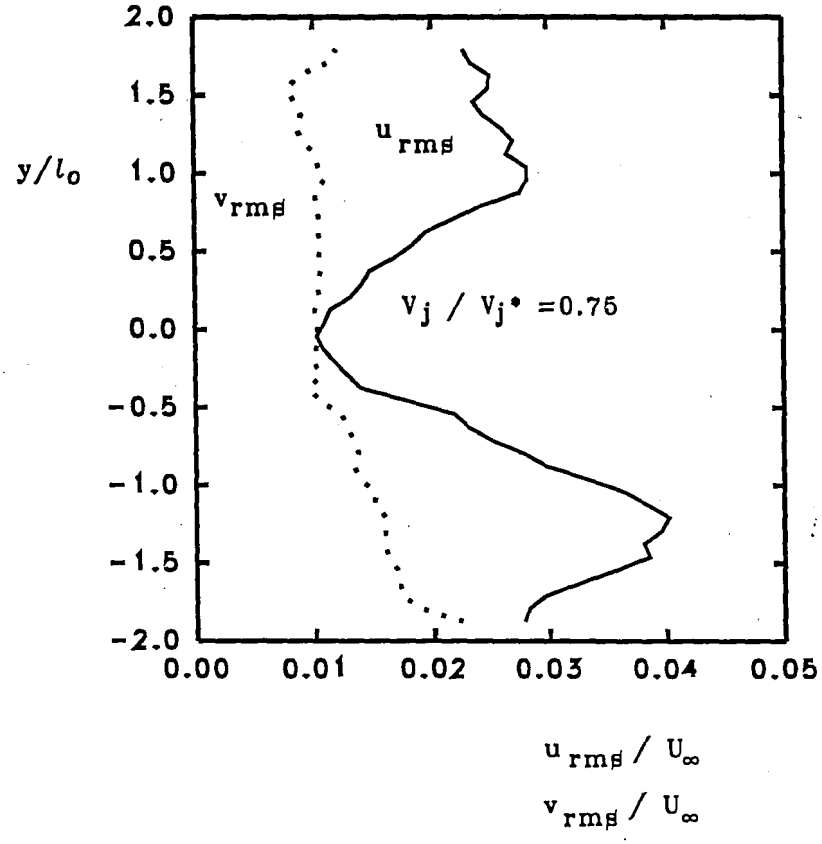

FIGURE 6.10: Normalized u_{rms}, v_{rms}, for single-slit trailing-edge (#1) with blowing approximately 75% of that needed for a momentumless wake.

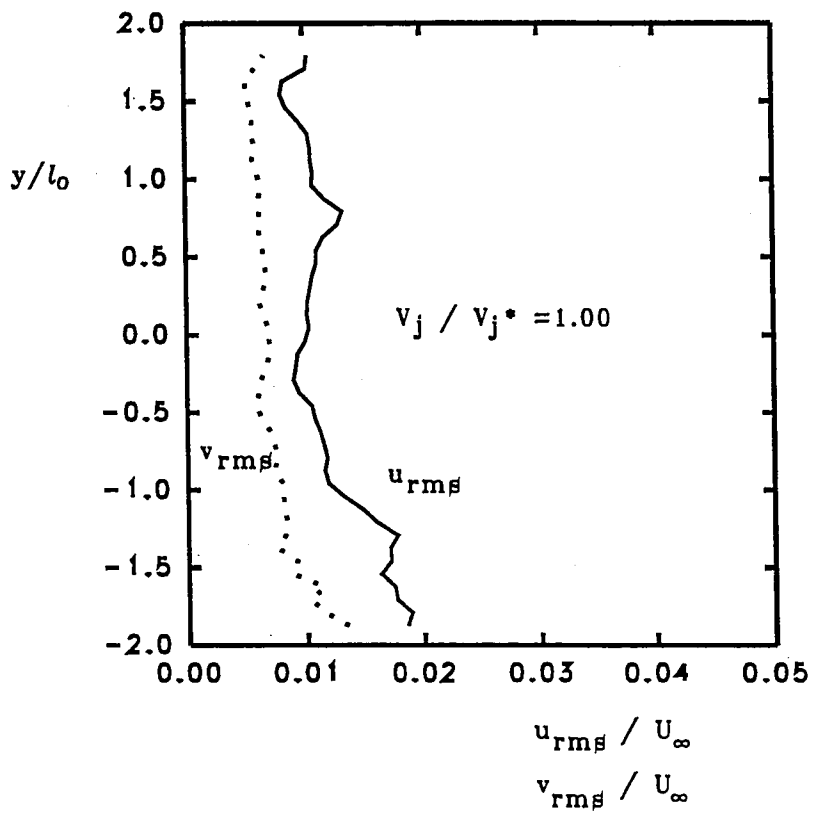

FIGURE 6.11: Normalized u_{rms}, v_{rms}, for single-slit trailing-edge (#1) with blowing to generate a momentumless wake.

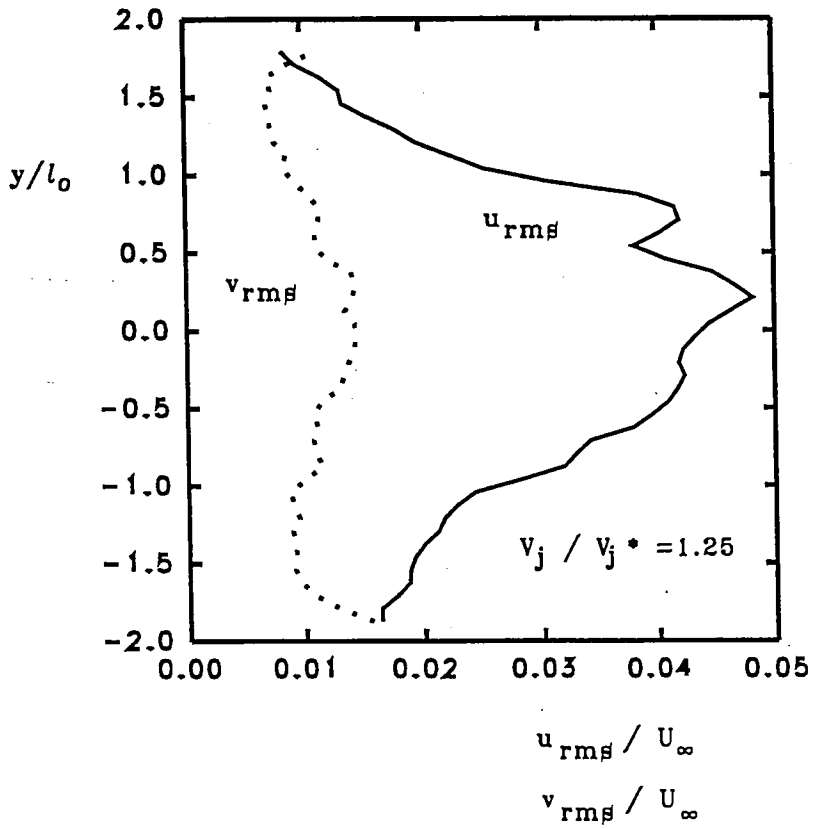

FIGURE 6.12: Normalized u_{rms}, v_{rms}, for single-slit trailing-edge (#1) with blowing approximately 125% of that needed for a momentumless wake.

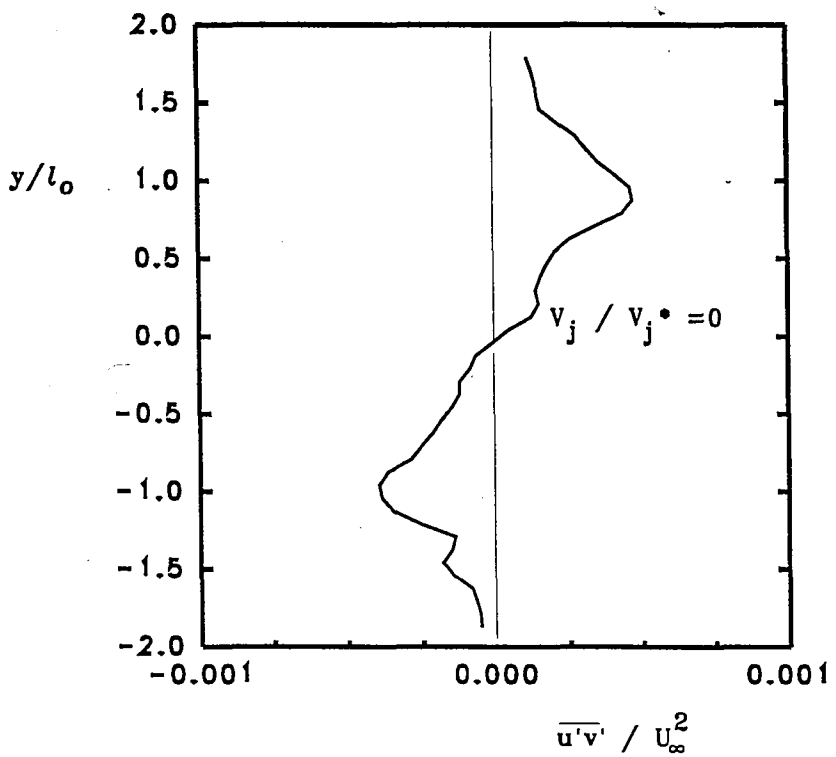

FIGURE 6.13: Normalized Reynolds Stress for single-slit trailing-edge (#1) with no blowing.

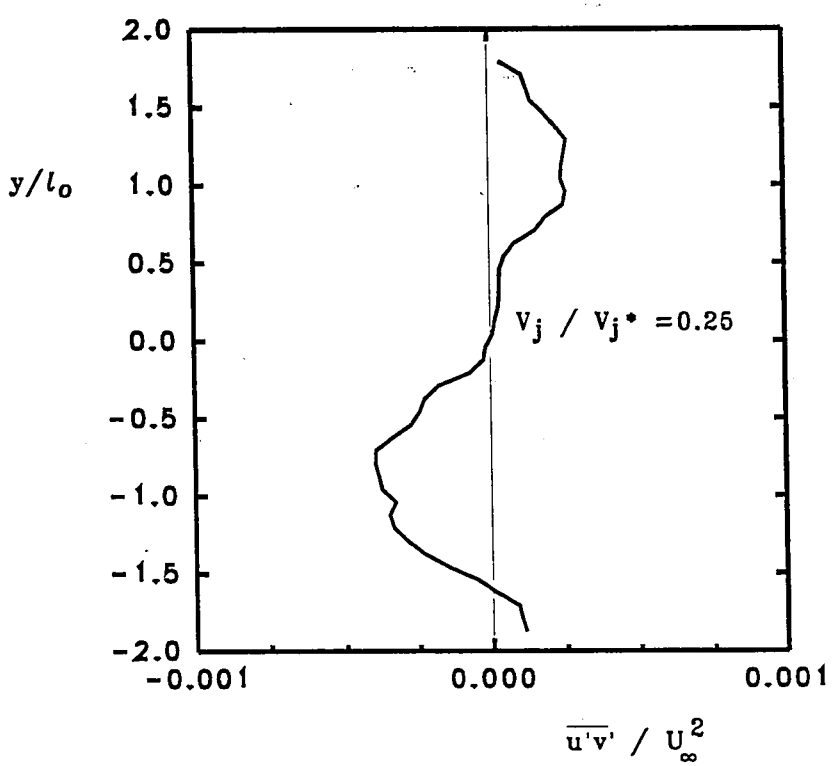

FIGURE 6.14: Normalized Reynolds Stress for single-slit trailing-edge (#1) with blowing approximately 25% of that needed for a momentumless wake.

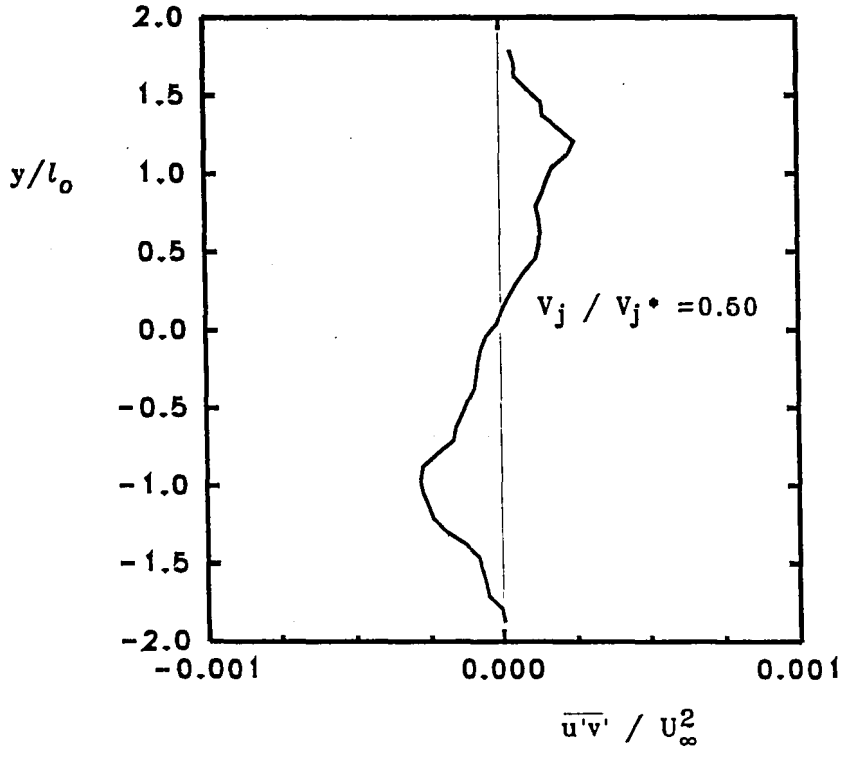

FIGURE 6.15: Normalized Reynolds Stress for single-slit trailing-edge (#1) with blowing approximately 50% of that needed for a momentumless wake.

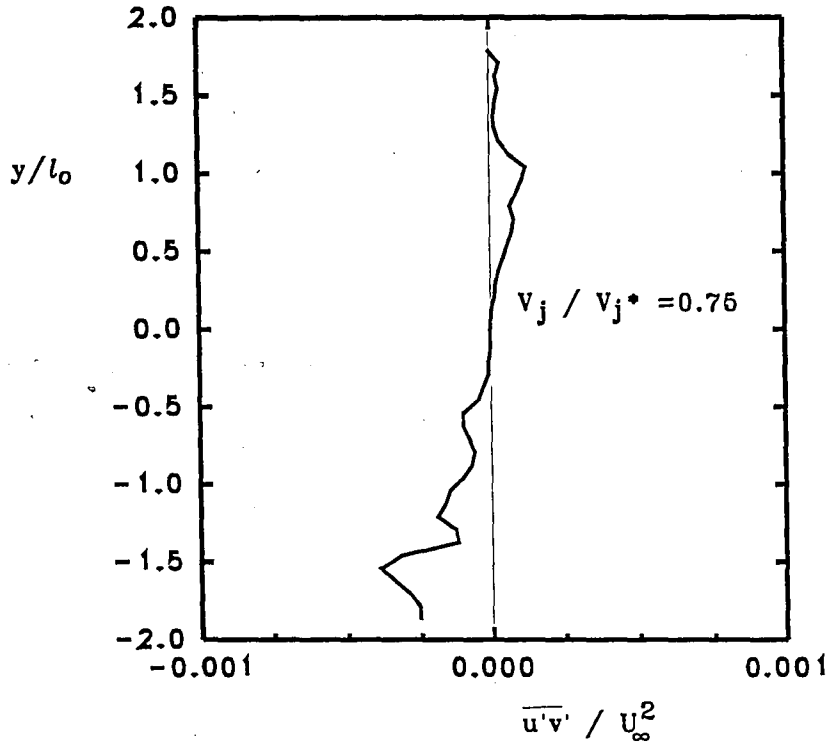

FIGURE 6.16: Normalized Reynolds Stress for single-slit trailing-edge (#1) with blowing approximately 75% of that needed for a momentumless wake.

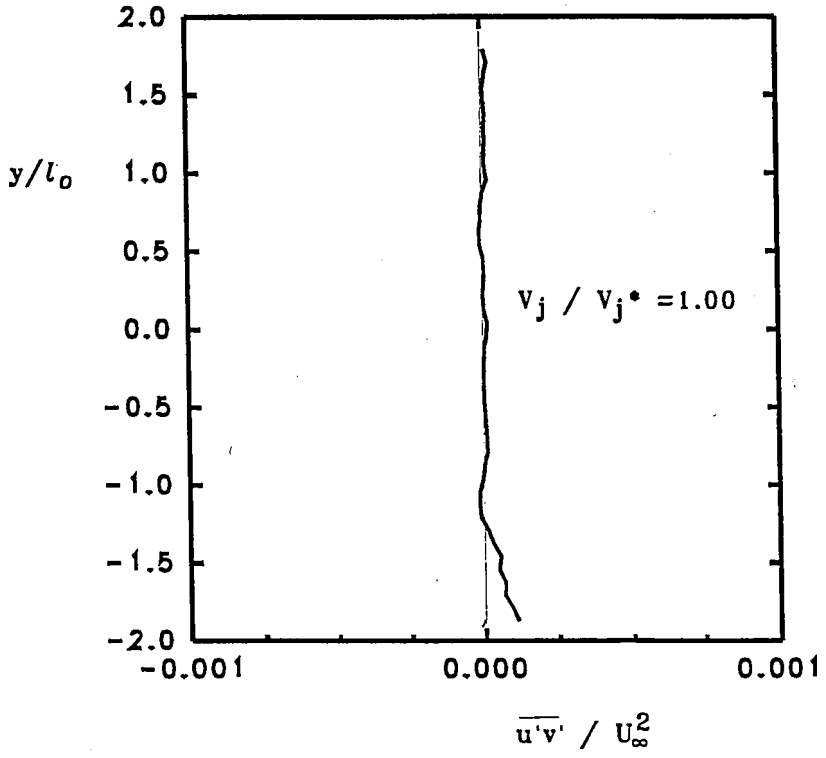

FIGURE 6.17: Normalized Reynolds Stress for single-slit trailing-edge (#1) with blowing needed to generate momentumless wake.

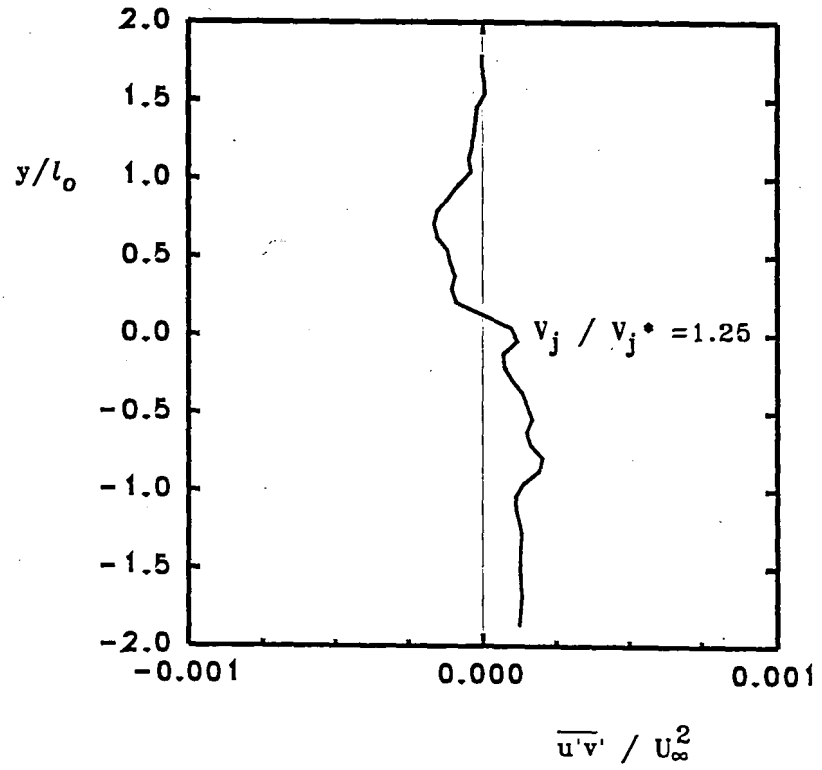

FIGURE 6.18: Normalized Reynolds Stress for single-slit trailing-edge (#1) with blowing approximately 125% of that needed for a momentumless wake.

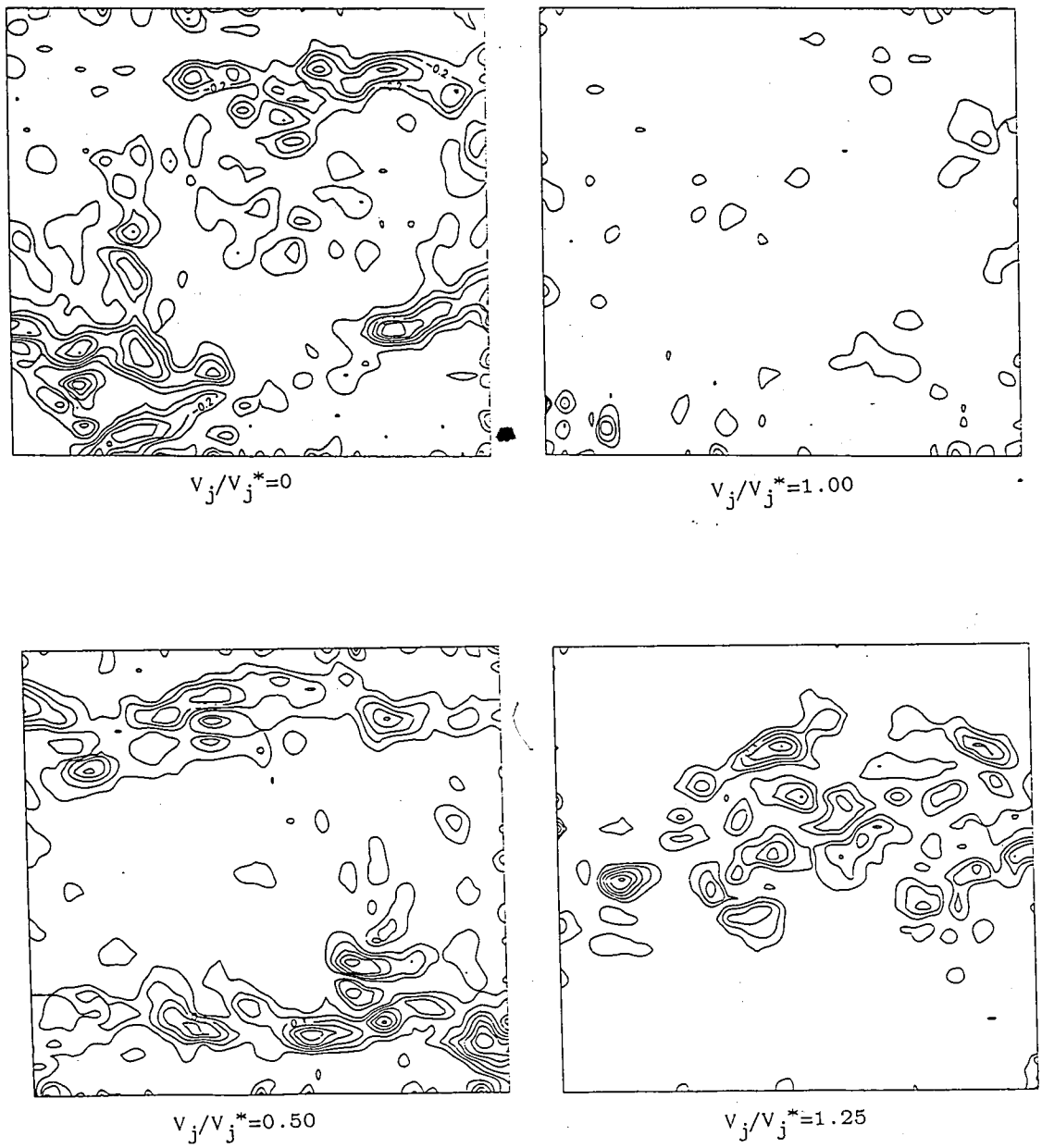

FIGURE 6.19: Instantaneous vorticity contours at various blowing rates for single-slit trailing-edge. Area pictured is approximately 3.8 x 4.3 *lo*. Contours are generated for every 0.1 change in the vorticity level (outside to inside).

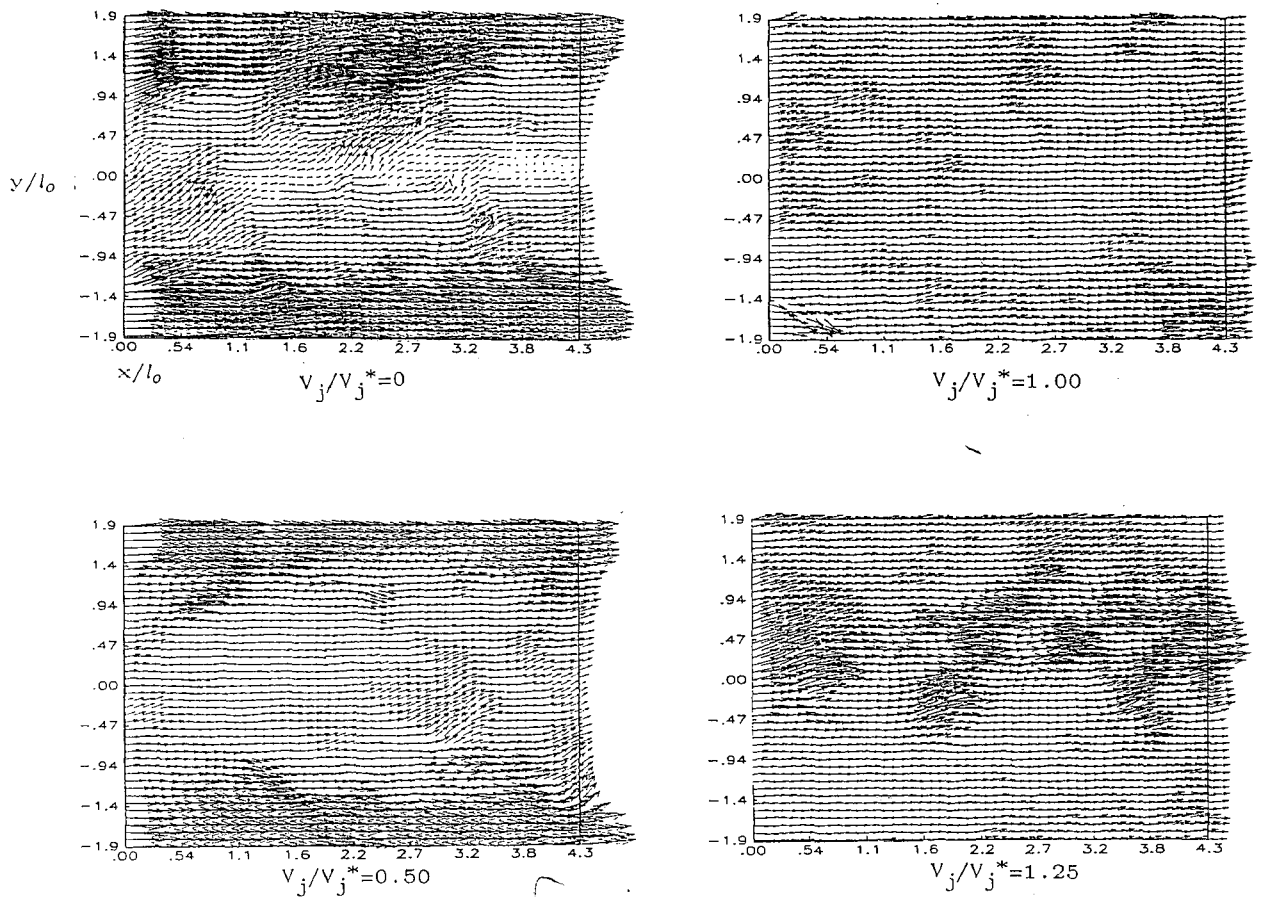

FIGURE 6.20: Instantaneous velocity fields at various blowing rates for single-slit trailing edge. All fields include a 78% bias in order to emphasize wake structure. Approximate area is 3.8 x 4.3 l_o, where l_o is the half-width of the full wake in the absence of blowing.

EXPERIMENT 3: DOUBLE-SLIT TRAILING-EDGE WITH BLOWING

The experimental procedure used in experiment 3 will be similar to those used in both experiments 1 and 2. Exact procedures for camera/ laser settings, field placement, and tunnel conditions can be found within the details of experiment 1. The data itself will appear in an identical form as experiment 2 with the exception of some obvious changes. The most obvious change is the change in the conditions necessary to obtain a momentumless wake. The double-slit trailing edge had much more open injection area making higher blowing rates necessary in order to obtain a momentumless wake. Pumping facilities were altered in order to accommodate the new trailing-edge. Even with added pumping power it became impossible to obtain a jet velocity $V_j/V_j^*=1.25$. Instead data for the maximum pump setting ($V_j/V_j^*=1.13$) is presented.

All normalization will be done as in experiment 2. The relationship between jet velocity and blowing rate for a total slit area of 2 slits x 1/16" x 16" = 2" sq. is as follows.

$V_j/V_j^*=0.00$	Q=0.00 gal/min	V=0.00 in/s	$V^2A=0.00$ in^3/s
0.25	2.78	5.35	57.2
0.50	5.55	10.7	229
0.75	8.33	16.0	512
1.00	11.1	21.4	916
1.13	12.5	24.1	1161

For the $V_j/V_j^*=0$ case, the velocity deficit profile exhibited a slightly larger deficit than in the single-slit case (figure 7.1). This is related to the substantially different configuration of the trailing edge. As blowing is

added, the wake begins to fill in first on either side of the centerline. This effect dominates the nearly identical V_j/V_j^*=0.25 and 0.50 cases (figures 7.2, 7.3). As the blowing increases further, the center of the wake begins to fill in as well. Figure 7.5 demonstrates the momentumless wake. With this double-slit trailing-edge, the shape of the wake takes a hybrid form of a wake and a jet, in contrast to the wake of the single-slit trailing-edge. As the blowing increases further, the velocity profile slowly approaches a jet-like form along the centerline.

The u_{rms} profile for the double-slit case at V_j/V_j^*=0 is at a much higher level than that of the single-slit case (Compare figure 6.13) while the v_{rms} case actually starts out at a slightly lower level. Neither value shows significant change through V_j/V_j^*=0.50 (figures 7.7 - 7.9). At V_j/V_j^*=0.75, the peak value of the u_{rms} distribution drops significantly, and the average value of the v_{rms} distribution drops slightly. For the momentumless case, u_{rms} remains roughly constant while v_{rms} increases slightly. The overblowing case (figure 7.12), demonstrates lower and more consistent levels for u_{rms} and slightly higher levels for v_{rms}.

The Reynolds stress results are somewhat more erratic than those seen in the single-slit case, but the trends are generally the same. The distributions $\overline{u'v'}(y)$ converge smoothly towards the center of the wake axis as blowing is increased. In figure 7.16, for V_j/V_j^* = 0.75, a nearly momentumless wake with a wake-like form while, at V_j/V_j^*=1.00 the form of a nearly momentumless wake has a jet-like form. All of the results show an unexplained asymmetry around the horizontal axis.

Figure 7.19 shows the instantaneous vorticity for the double-slit case. The mean vorticity dominates the low-

blowing cases. At the momentumless level, $V_j/V_j^*=1$, the field becomes filled with extensive patterns of low-level vorticity. The $V_j/V_j^*=1.13$ shows similar patterns.

Figure 7.20 shows instantaneous velocity fields for several blowing cases. The wake is initially widened by the lower blowing rates. When the $V_j/V_j^*=1.00$ case is reached, a wide central jet forms, surrounded by two small wakes, and the freestream. As the blowing continues to increase, the field becomes more uniform, and a less pronounced central jet can be noted.

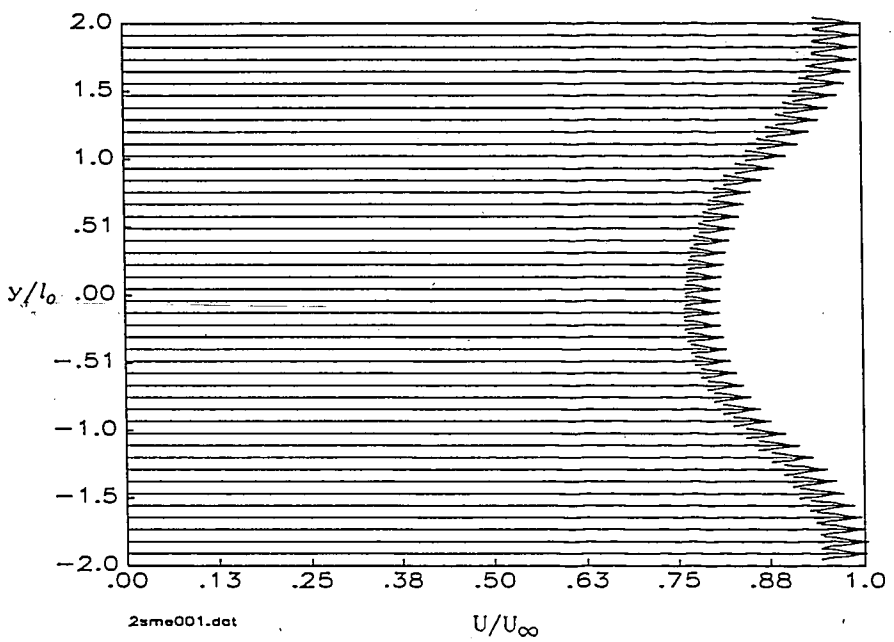

FIGURE 7.1: Normalized Velocity Profile for double-slit trailing-edge (#2) with no blowing.

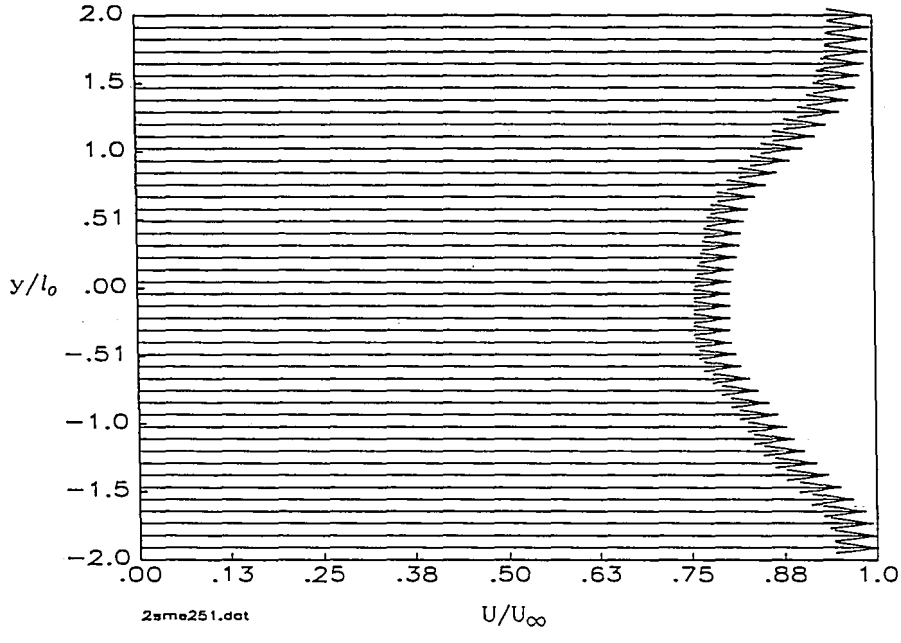

FIGURE 7.2: Normalized Velocity Profile for double-slit trailing-edge (#2) with blowing rate approximately 25% of that needed for a momentumless wake.

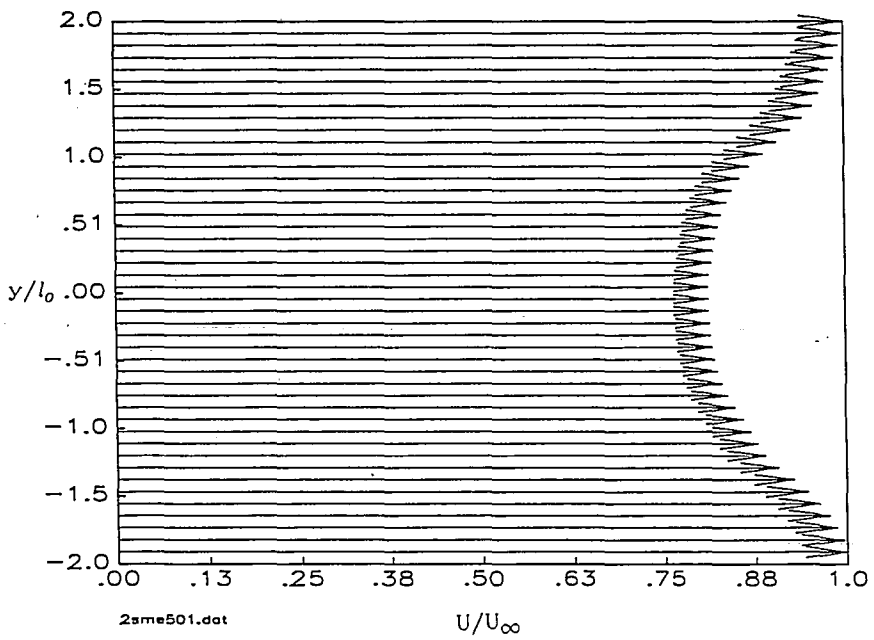

FIGURE 7.3: Normalized Velocity Profile for double-slit trailing-edge (#2) with blowing rate approximately 50% of that needed for a momentumless wake.

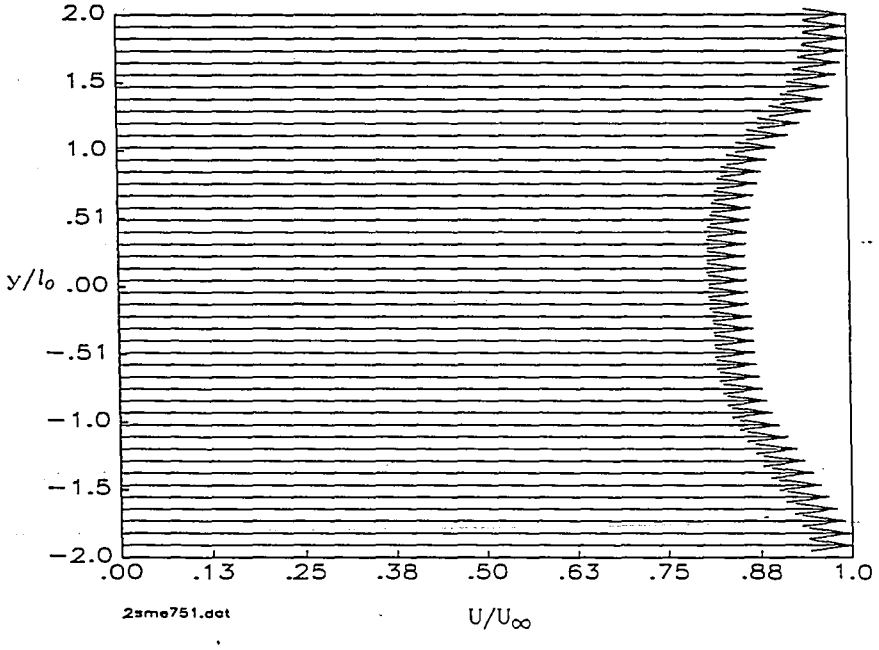

FIGURE 7.4: Normalized Velocity Profile for double-slit trailing-edge (#2) with blowing rate approximately 75% of that needed for a momentumless wake.

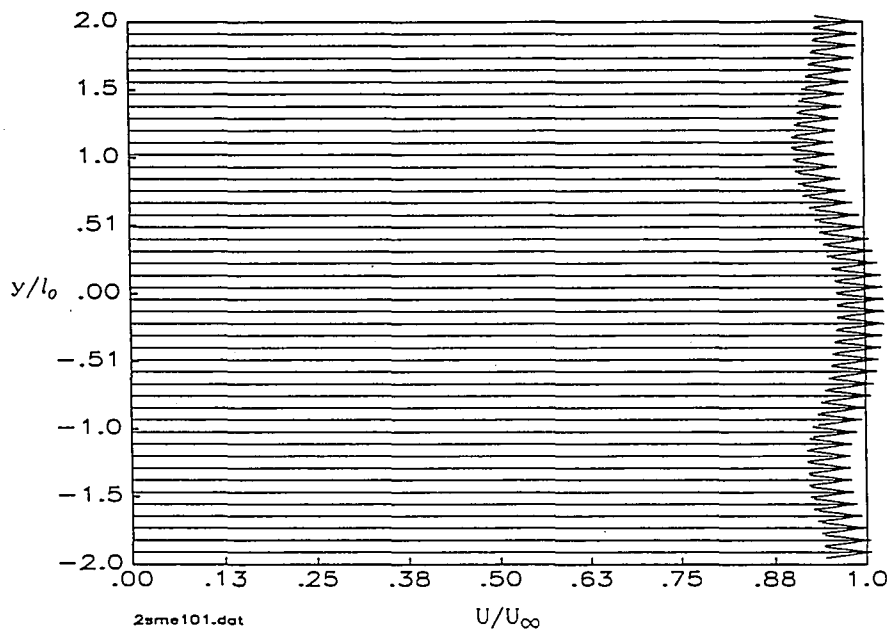

FIGURE 7.5: Normalized Velocity Profile for double-slit trailing-edge (#2) with blowing to generate a momentumless wake.

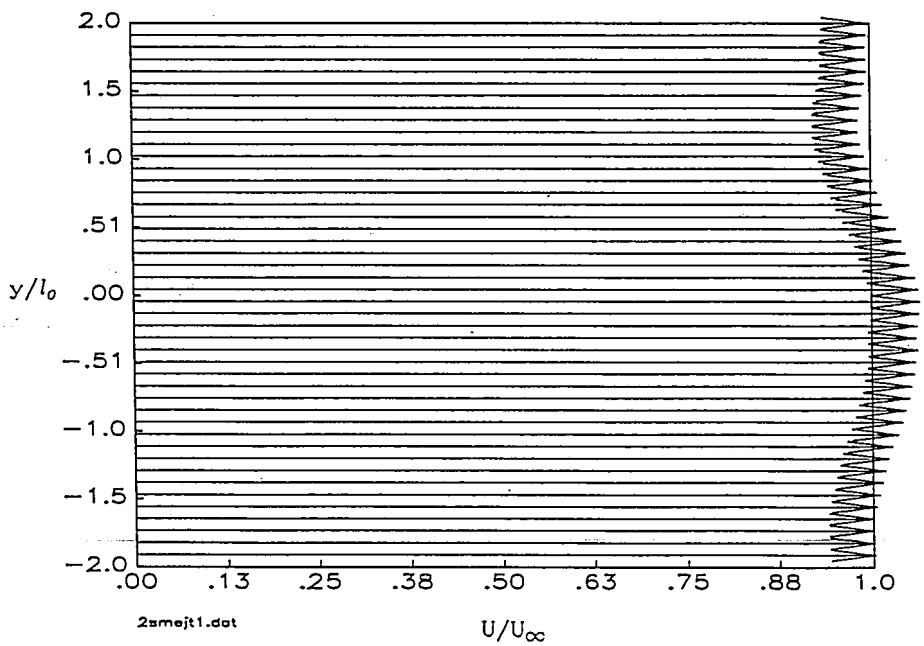

FIGURE 7.6: Normalized Velocity Profile for double-slit trailing-edge (#2) with blowing approximately 113% of that needed for a momentumless wake.

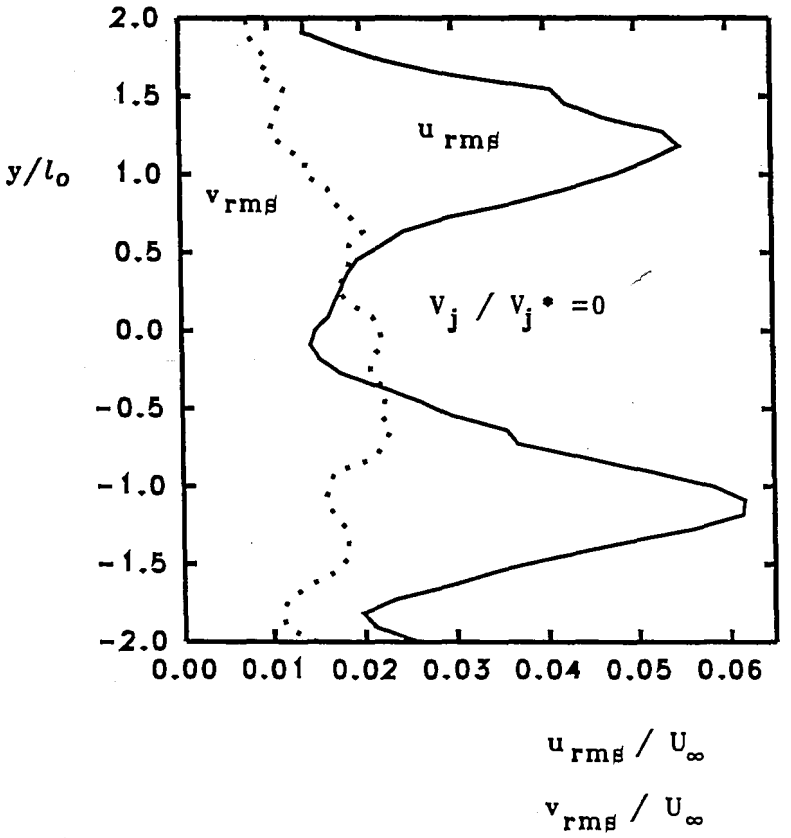

FIGURE 7.7: Normalized u_{rms}, v_{rms}, for double-slit trailing-edge (#2) with no blowing.

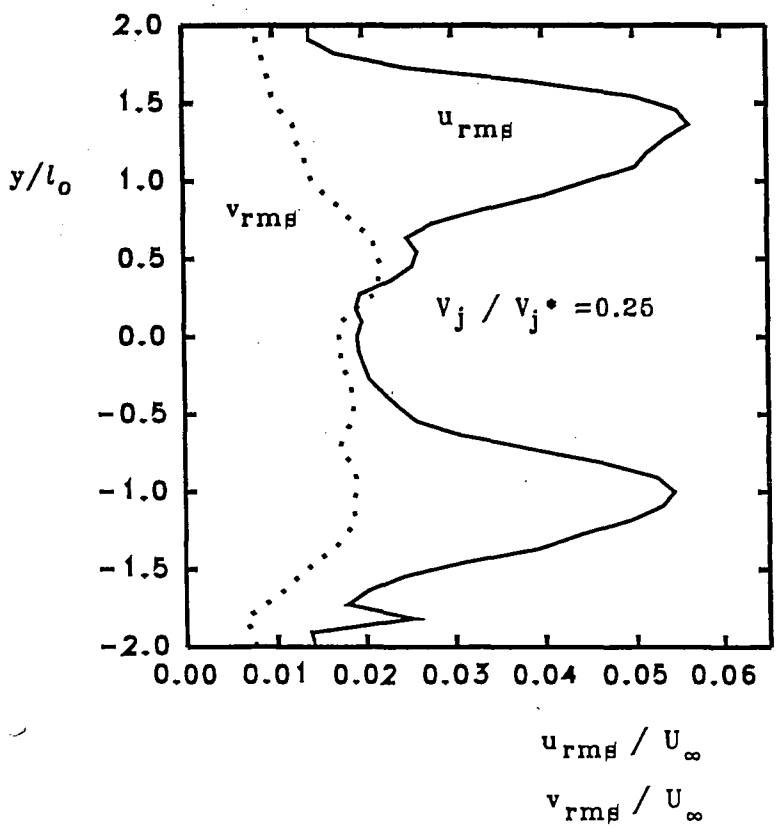

FIGURE 7.8 Normalized u_{rms}, v_{rms}, for double-slit trailing-edge (#2) with blowing approximately 25% of that needed for a momentumless wake.

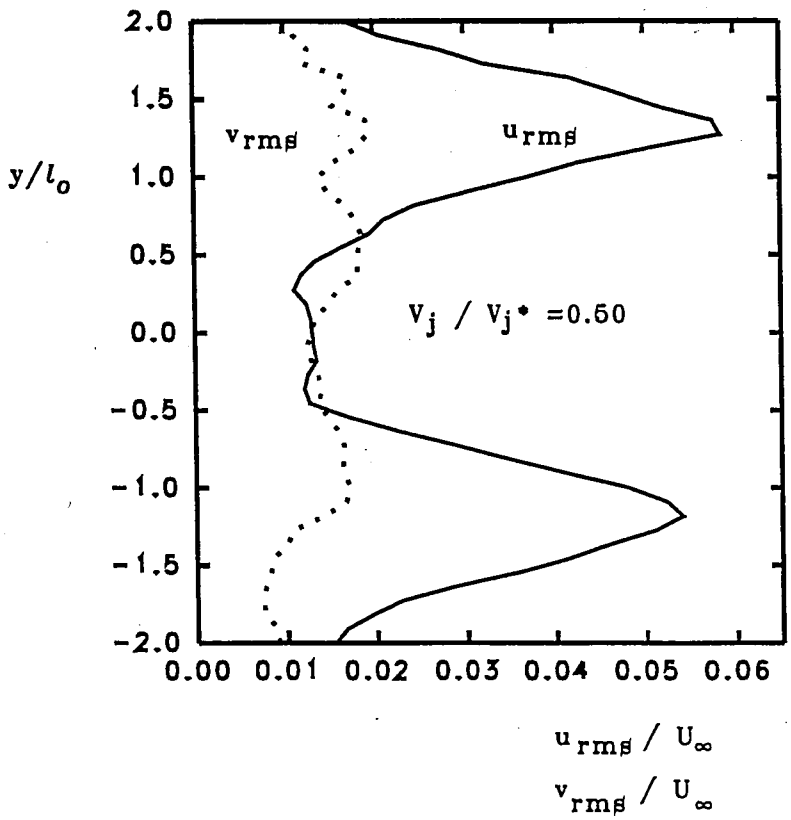

FIGURE 7.9: Normalized u_{rms}, v_{rms}, for double-slit trailing-edge (#2) with blowing approximately 50% of that needed for a momentumless wake.

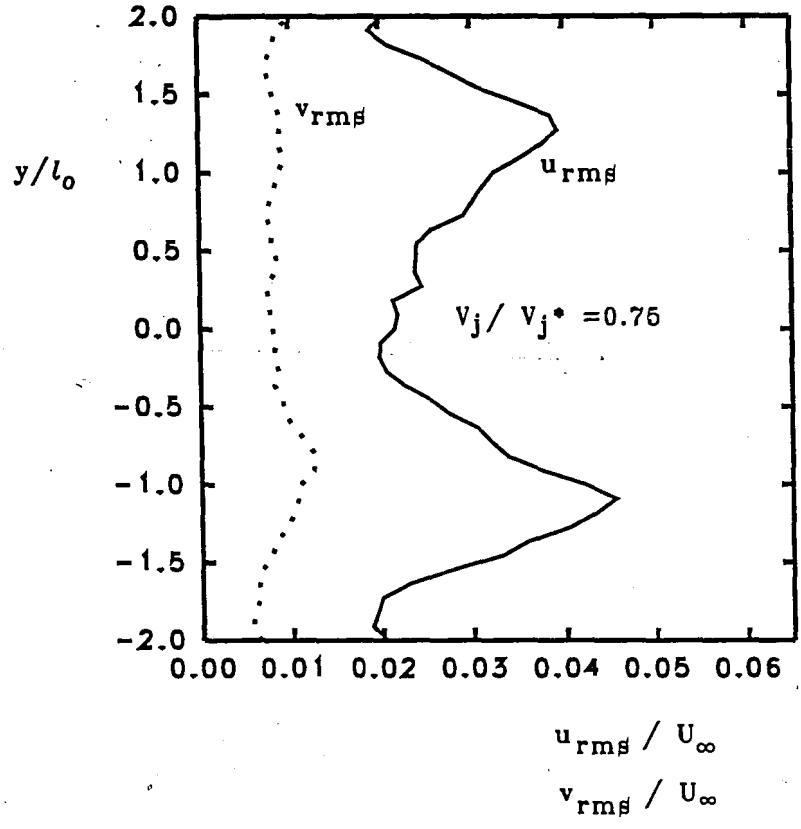

FIGURE 7.10: Normalized u_{rms}, v_{rms}, for double-slit trailing-edge (#2) with blowing approximately 75% of that needed for a momentumless wake.

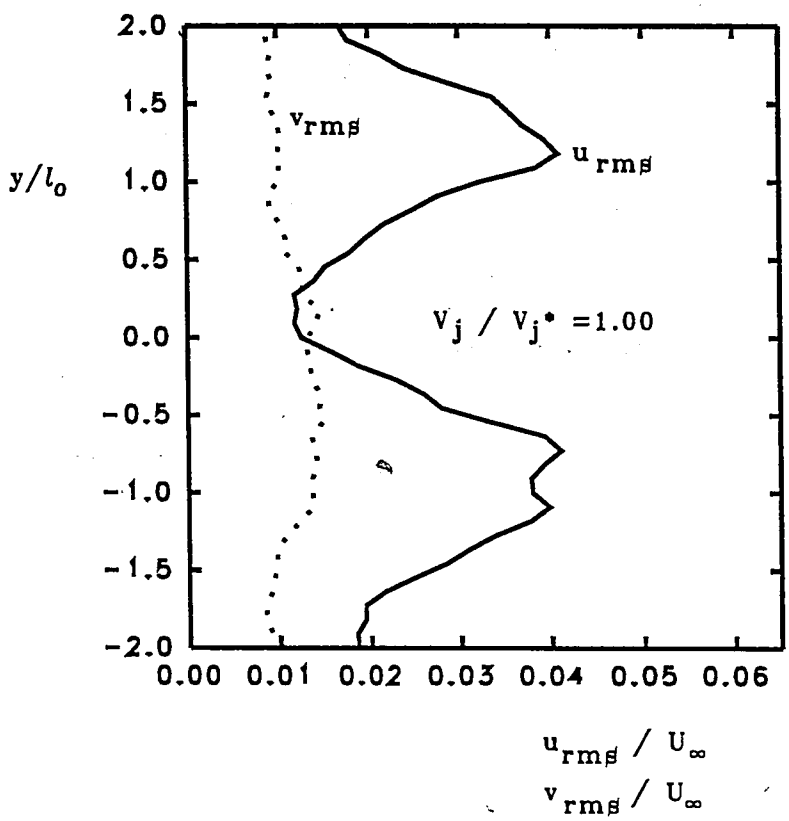

FIGURE 7.11: Normalized u_{rms}, v_{rms}, for double-slit trailing-edge (#2) with blowing to generate a momentumless wake.

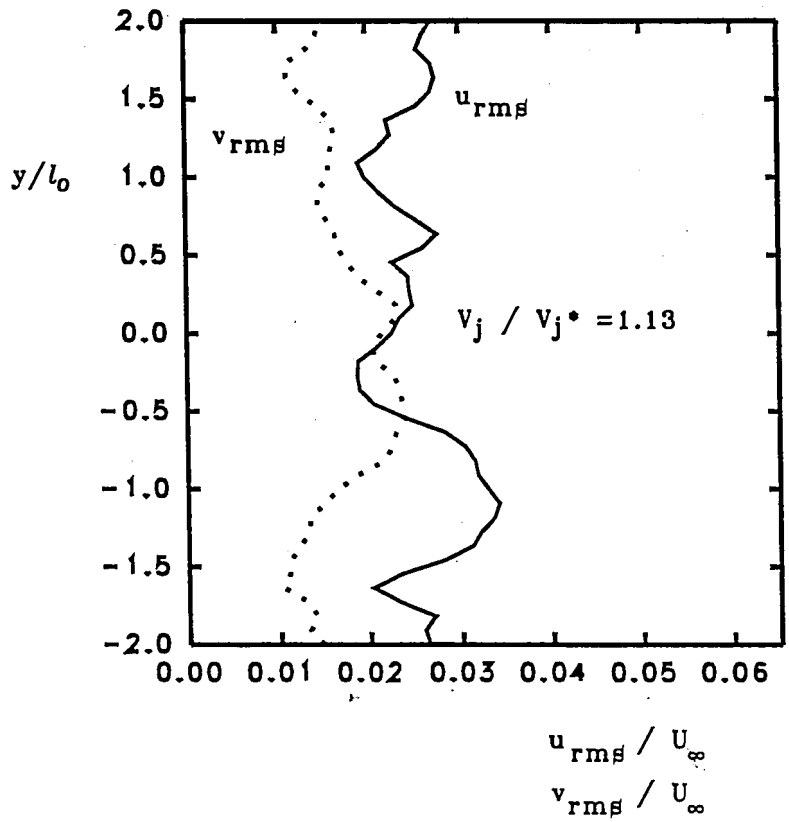

FIGURE 7.12: Normalized u_{rms}, v_{rms}, for double-slit trailing-edge (#2) with blowing approximately 113% of that needed for a momentumless wake.

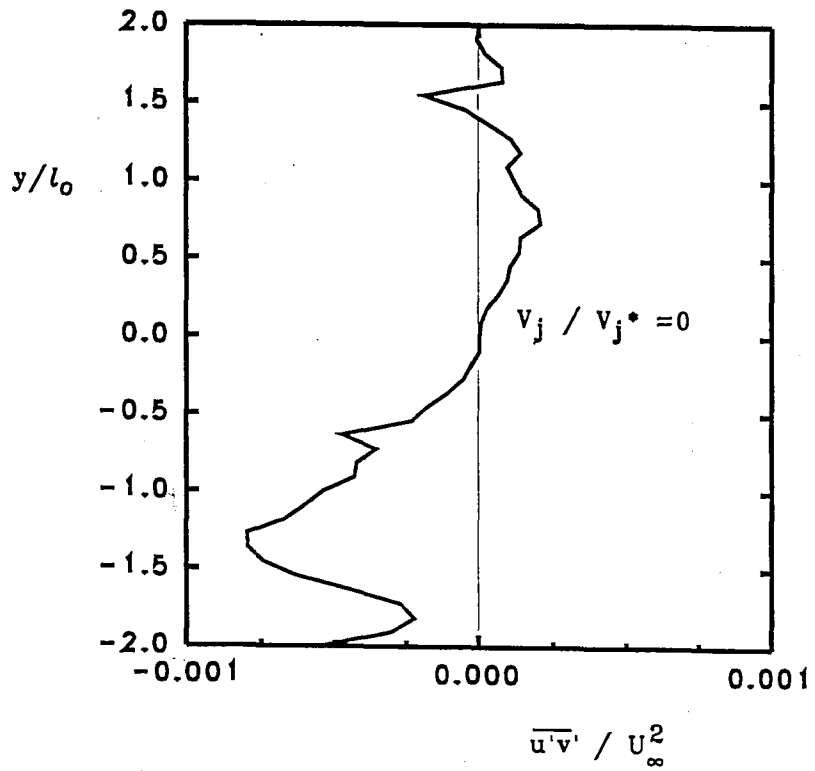

FIGURE 7.13: Normalized Reynolds Stress for double-slit trailing-edge (#2) with no blowing.

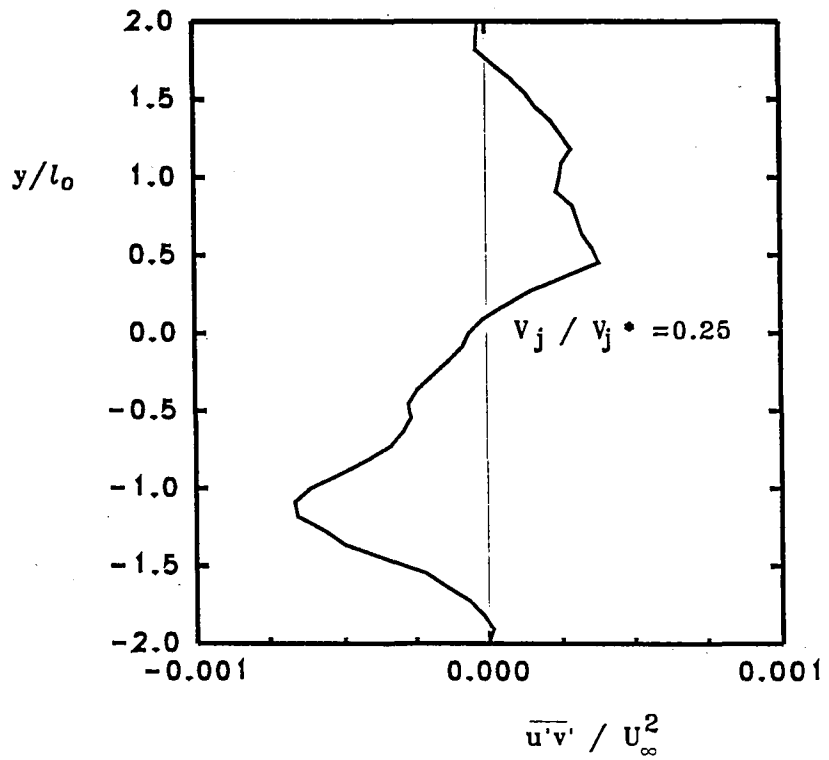

FIGURE 7.14: Normalized Reynolds Stress for double-slit trailing-edge (#2) with blowing approximately 25% of that needed for a momentumless wake.

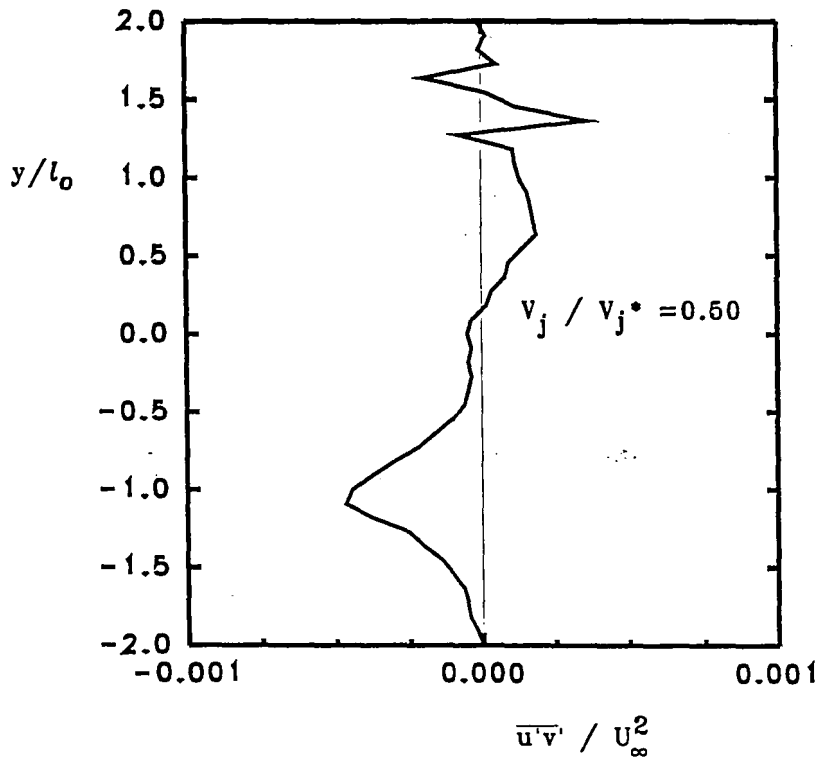

FIGURE 7.15: Normalized Reynolds Stress for double-slit trailing-edge (#2) with blowing approximately 50% of that needed for a momentumless wake.

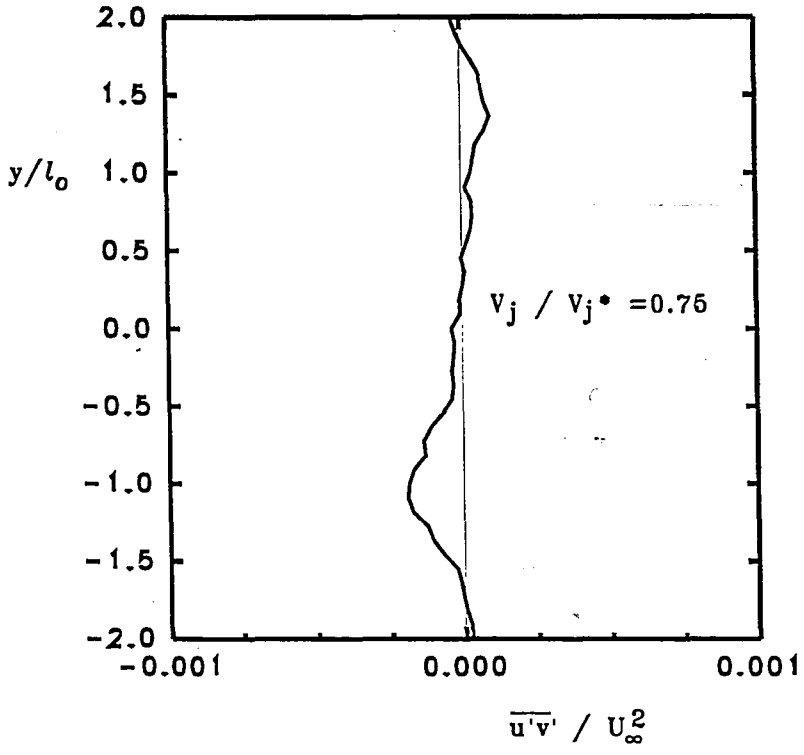

FIGURE 7.16: Normalized Reynolds Stress for double-slit trailing-edge (#2) with blowing approximately 75% of that needed for a momentumless wake.

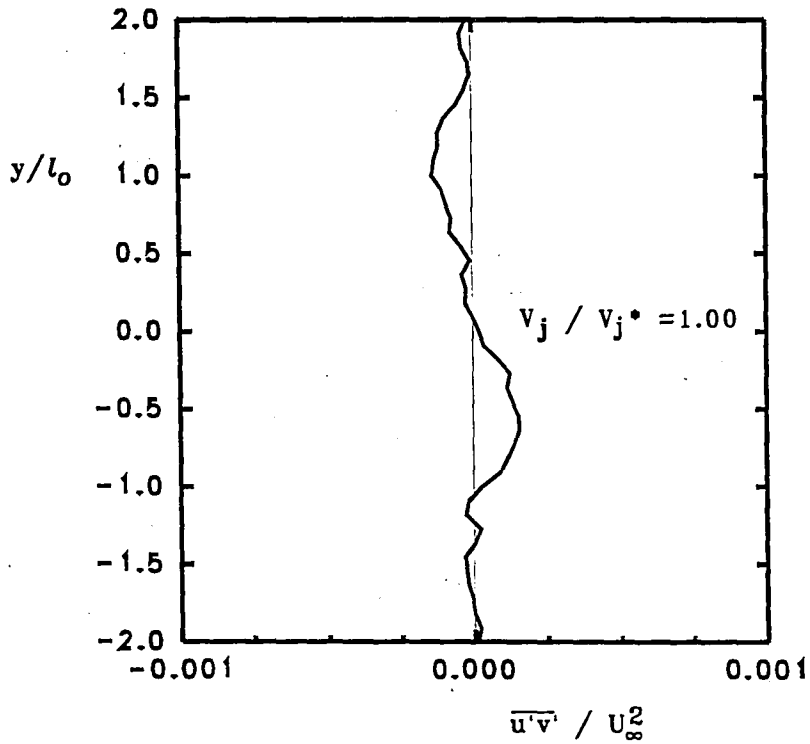

FIGURE 7.17: Normalized Reynolds Stress for double-slit trailing-edge (#2) with blowing needed to generate momentumless wake.

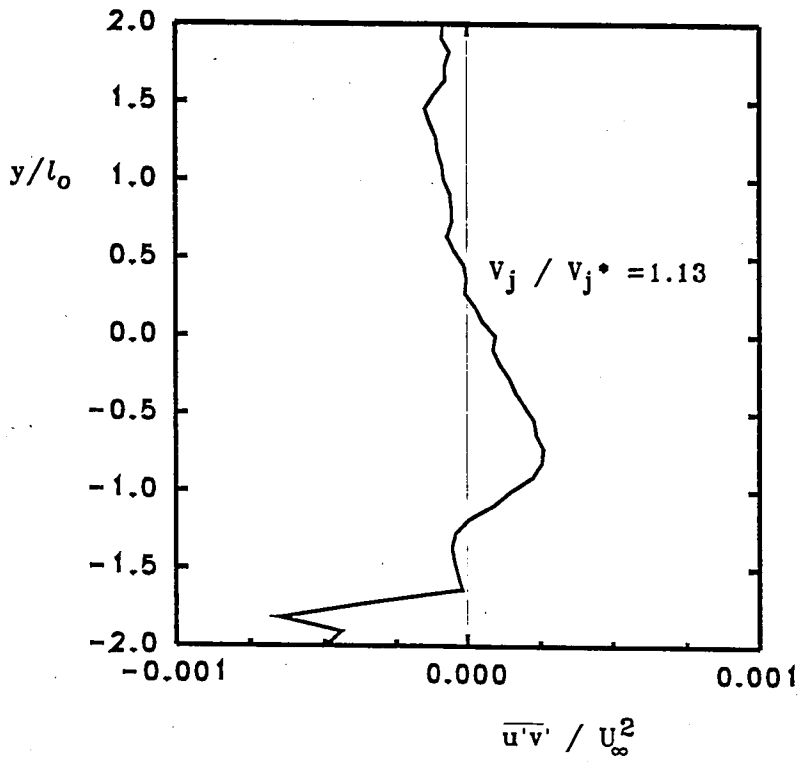

FIGURE 7.18: Normalized Reynolds Stress for double-slit trailing-edge (#2) with blowing approximately 113% of that needed for a momentumless wake.

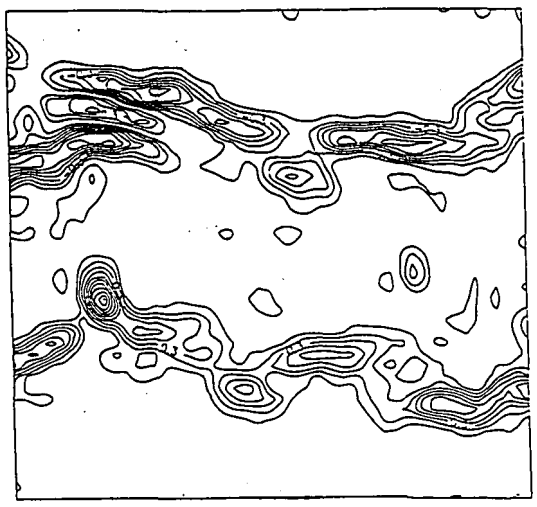

$V_j/V_j^*=0$

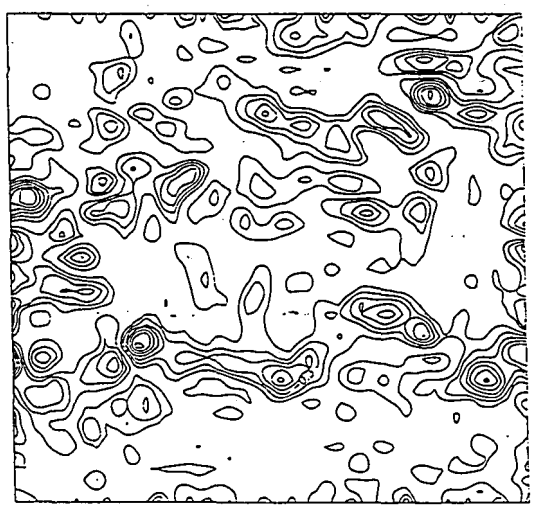

$V_j/V_j^*=1.00$

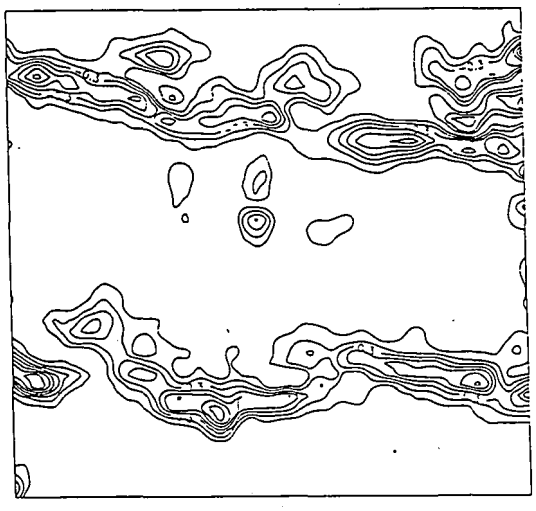

$V_j/V_j^*=0.50$

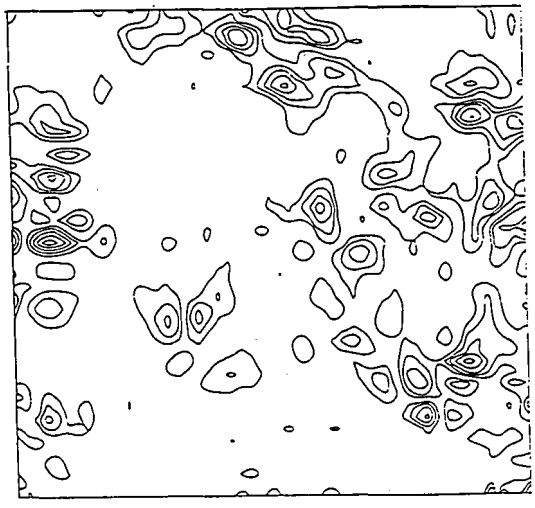

$V_j/V_j^*=1.13$

FIGURE 7.19: Instantaneous vorticity contours at various blowing rates for double-slit trailing-edge. Area pictured is approximately 4.0 x 4.6 *lo*. Contours are generated for every 0.1 change in the vorticity level (outside to inside).

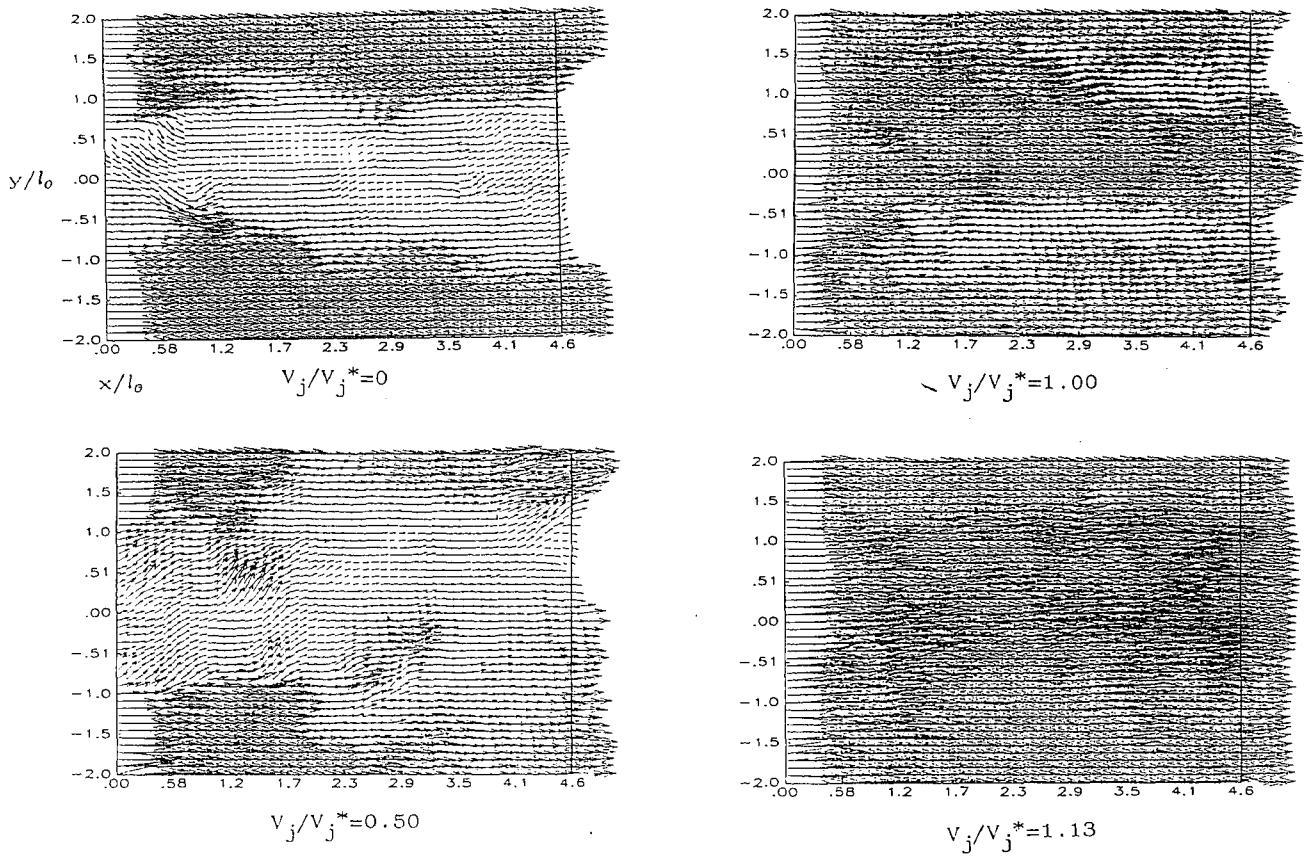

FIGURE 7.20: Instantaneous velocity fields at various blowing rates for double-slit trailing edge. All fields include a 78% bias in order to emphasize wake structure. Approximate area is 4.0 x 4.6 l_o, where l_o is the half-width of the full wake in the absence of blowing.

CONCLUDING REMARKS

Figure 8.1 shows an overview of the deficit profiles for the single- and double-slit trailing-edges at over the range of blowing rates. At the $V_j/V_j^*=0$ level, both wakes appear to have similar characteristics. When blowing is employed the blowing configuration tends to affect the shape of the wake. At $V_j/V_j^*=0.25$, the wake from the single-slit trailing-edge shows a smaller deficit, with a higher centerline velocity, and a more rounded shape. The wake from the double-slit trailing-edge fills in around its edges, leaving a deeper wake at the centerline. These trends continue through the case of $V_j/V_j^*=0.50$. When V_j/V_j^* approaches 0.75, the blowing begins to affect the centerline velocity of the wake from the double-slit trailing-edge. A general flattening near the centerline can be noted. The centerline velocity of the wake from the double-slit trailing-edge becomes roughly the same as that seen from the single-slit trailing edge.

The momentumless wakes established were dependent upon the blowing configuration at the trailing-edge. The single-slit trailing-edge generated a flatter, more consistent profile, while the double-slit trailing edge generated more of a hybrid wake-jet profile that maintained characteristics of both flows. In both cases, the momentumless wakes were established at a threshold level of blowing above $V_j/V_j^*=0.75$ corresponding to a rapid reduction of the wake deficit. The shapes of the velocity profiles were transformed into shapes representative of jet flows as the level of blowing was increased further. In summary, the momentumless wakes showed wakes with small deficits or excesses occur over a small range of blowing rates near that corresponding to a momentumless wake

The u_{rms} distributions corresponding to the single-slit

trailing-edge similarly show small changes up to blowing rates of $V_j/V_j^*=0.75$ as shown in figure 8.2. For the double-slit trailing edge (figure 8.3) the u_{rms} level was higher with no blowing, $V_j/V_j^*=0$. As blowing was implemented these peaks decreased only slightly up to $V_j/V_j^*=0.75$. The $V_j/V_j^*=0.75$ case shows a slightly more uniform profile which is quickly lost as more blowing is added. The peaks shown in the $V_j/V_j^*=1.0$ case are caused by the hybrid nature of the wake itself. They appear at the borders between the superimposed jets blown from the trailing-edge and the wake-like boundary of the central portion of the profile. The case of $V_j/V_j^*=1.13$ flattens out the u_{rms} profile.

The v_{rms} results for the single-slit trailing-edge in figure 8.4, show a progression similar to that for the u_{rms} case. The double-slit trailing-edge behavior is similar as well, with the exception of the fact that higher v_{rms} levels appear for the $V_j/V_j^*=1.00$ and 1.13 cases.

The Reynolds stress distributions generally show a more gradual change as the level of blowing is increased. The momentumless wake case for the single-slit trailing-edge shows a nearly complete vanishing of the Reynolds stress which is what could never exist in a uniform flow. Inversion of the shape of the Reynolds stress distribution nodes occurs, as expected, for the jet flow case.

The double-slit trailing edge showed more erratic results. A slight asymmetry about the wake centerline for the single-slit configuration becomes more pronounced for the double-slit configuration. The Reynolds stress values for the double-slit begin higher and decrease more quickly. The switch from a shape of the $\overline{u'v'}(y)$ representative pure-wake characteristics to that of a jet seems to occur between the $V_j/V_j^*=0.75$ and 1.0 cases.

As a general conclusion, it is obvious that the wake properties we have examined have, in general, a momentumless wake form directly related to the manner in which the blowing is introduced at the trailing-edge. In the case of the single-slit trailing-edge, these effects all seem to correspond to one particular blowing rate, while with the double-slit trailing edge, the characteristics associated with a momentumless wake do not appear simultaneously due to the more complex nature of the flow. Of course, we have examined only one streamwise location in this investigation. If the flow were allowed to relax at larger streamwise distances, we expect a tendency towards a more uniform mean velocity distribution and a reduction in the trend of the fluctuation parameters. At shorter spanwise distances, however, a design decision may have to be made as to which of these quantities (i.e. velocity deficit, u_{rms}, v_{rms}, Reynolds stress, vorticity, etc.) the designer is most interested in minimizing.

In examining the effectiveness of this procedure for possible use in decreasing fan-inlet noise in turbo machinery, we must evaluate its potential benefits and drawbacks. It has been demonstrated that trailing-edge blowing can reduce the wake deficit significantly. Most of this reduction occurred, however, near the blowing level corresponding to a momentumless wake. Given the tuning necessary to maintain this wake with our simplistic conditions, the implication of a significant amount of hardware and control system development is apparent.

Finally it becomes apparent that the next steps within this research would revolve around further testing of different trailing-edge configurations. Referring back to the tables presented within experiments 1 and 2, it can easily be seen that the amount of momentum added (i.e. the V^2A terms) was roughly similar for each trailing-edge at

the various blowing rates. An obvious goal for the next prototype would be the delivery of higher-speed fluid which imparts more momentum to the flow for the same mass flow rate. A possible practical case to consider would be similar to trailing-edge #2, but constructed with smaller slits, possibly directed slightly towards the vertical center of the trailing-edge so that more momentum was imparted on the largest part of the deficit.

Another issue to consider would be the implementation of Vortex generation (see Kuethe, 1972) in conjunction with trailing-edge blowing. The induced vorticity might aid in the reduction of the wake deficit.

CONCLUSIONS:

(1) Trailing-edge blowing was effective in attenuating the mean wake deficit caused by the model rotor blade. The nature of the attenuation was specific to each trailing-edge.

(2) Trailing-edge blowing was also shown to affect other quantities including fluctuating velocity, Reynolds stress, and vorticity. Reductions in the levels of these quantities depended on the particular trailing-edge configuration. A single slit located at the trailing-edge was more effective than a double slit configuration located upstream of the trailing-edge.

(3) Relatively high blowing rates were needed to attenuate the mean wake deficit and the turbulence level. Further experiments should address trailing-edge configurations that minimize the magnitude of the trailing-edge blowing.

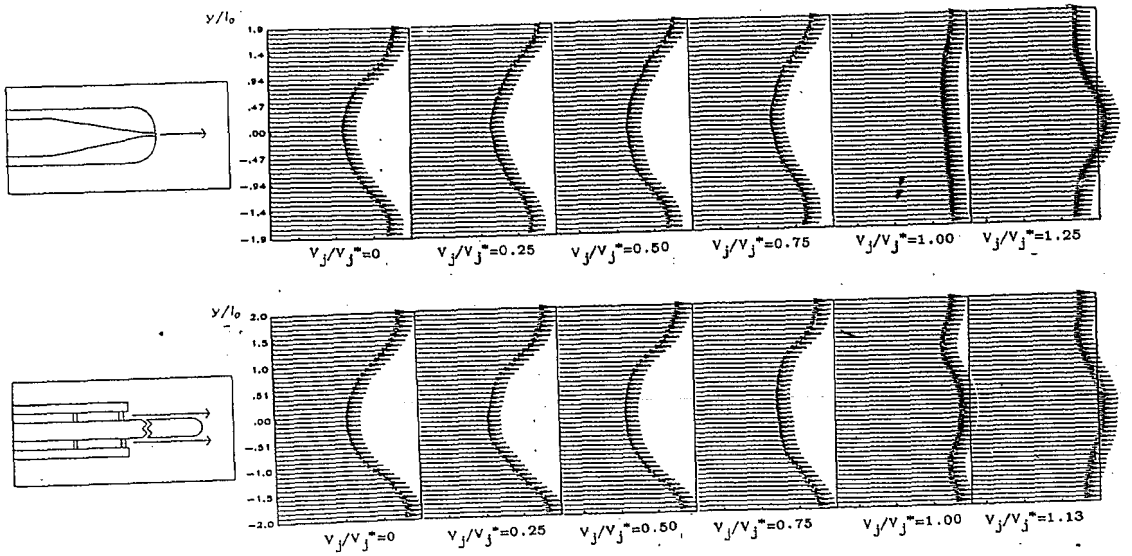

FIGURE 8.1: Normalized velocity defecit comparison for both trailing-edges over range of blowing rates. Single-slit trailing-edge appears at top and double slit trailing-edge at the bottom.

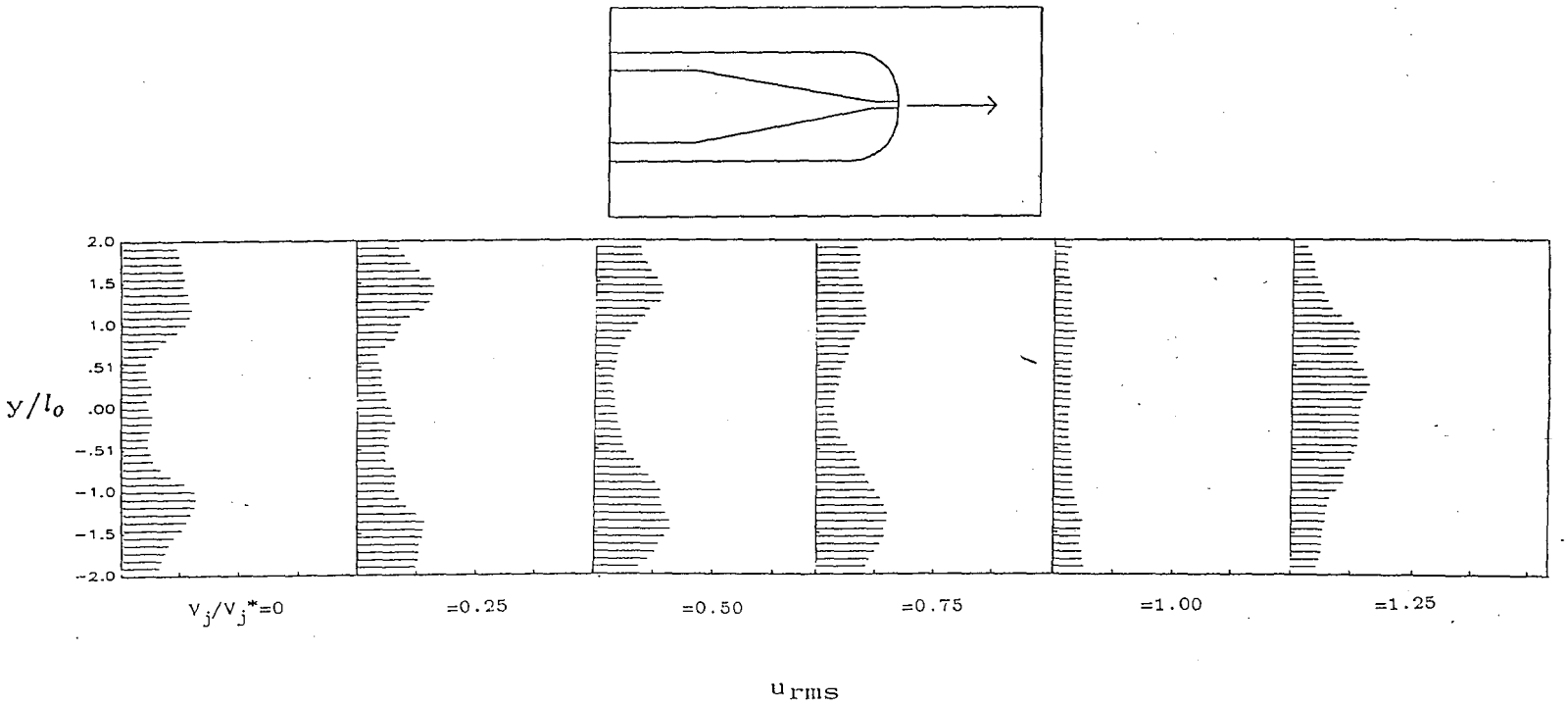

FIGURE 8.2: Comparison of profiles of u_{rms} for single-slit trailing-edge (#1) at all blowing rates. (Note: u_{rms} is not normalized.)

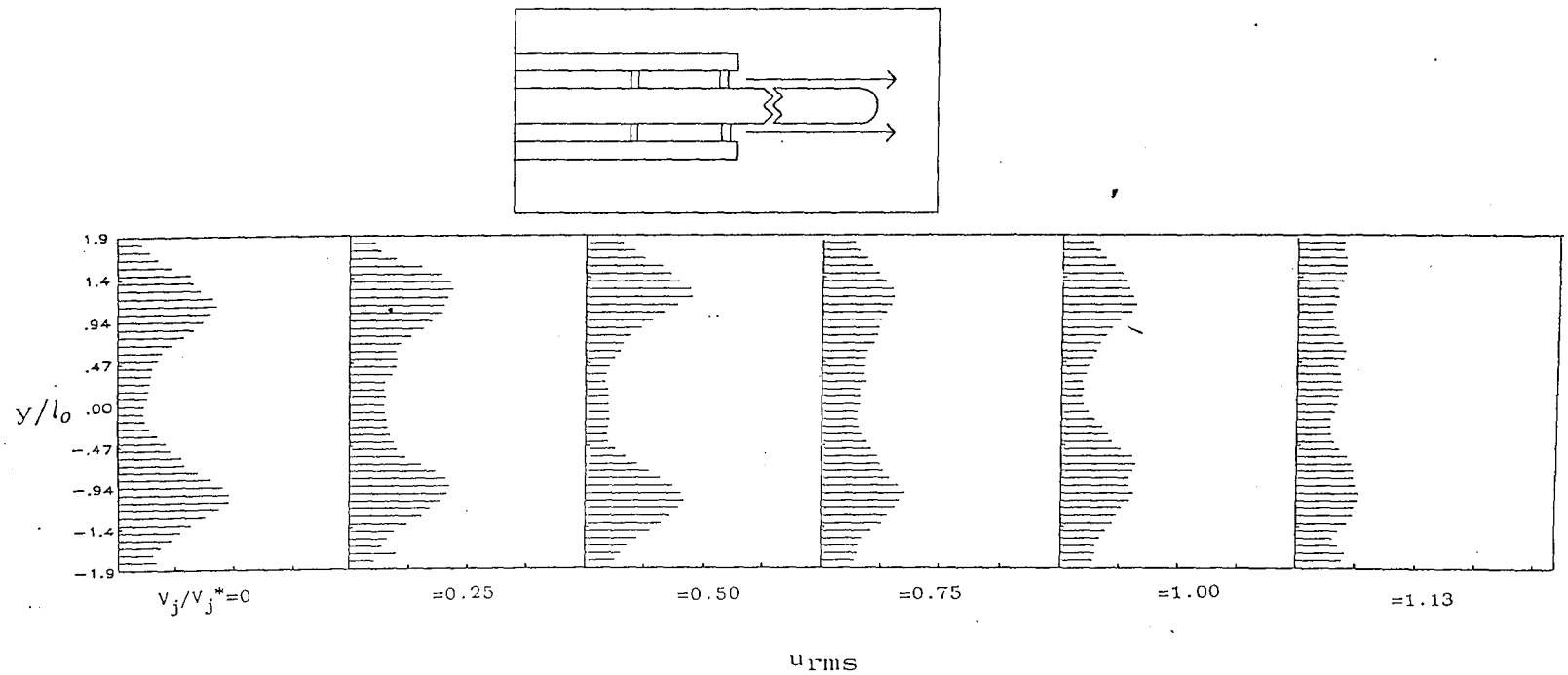

FIGURE 8.3: Comparison of profiles of u_{rms} for double-slit trailing-edge (#2) at all blowing rates. (Note: u_{rms} is not normalized.)

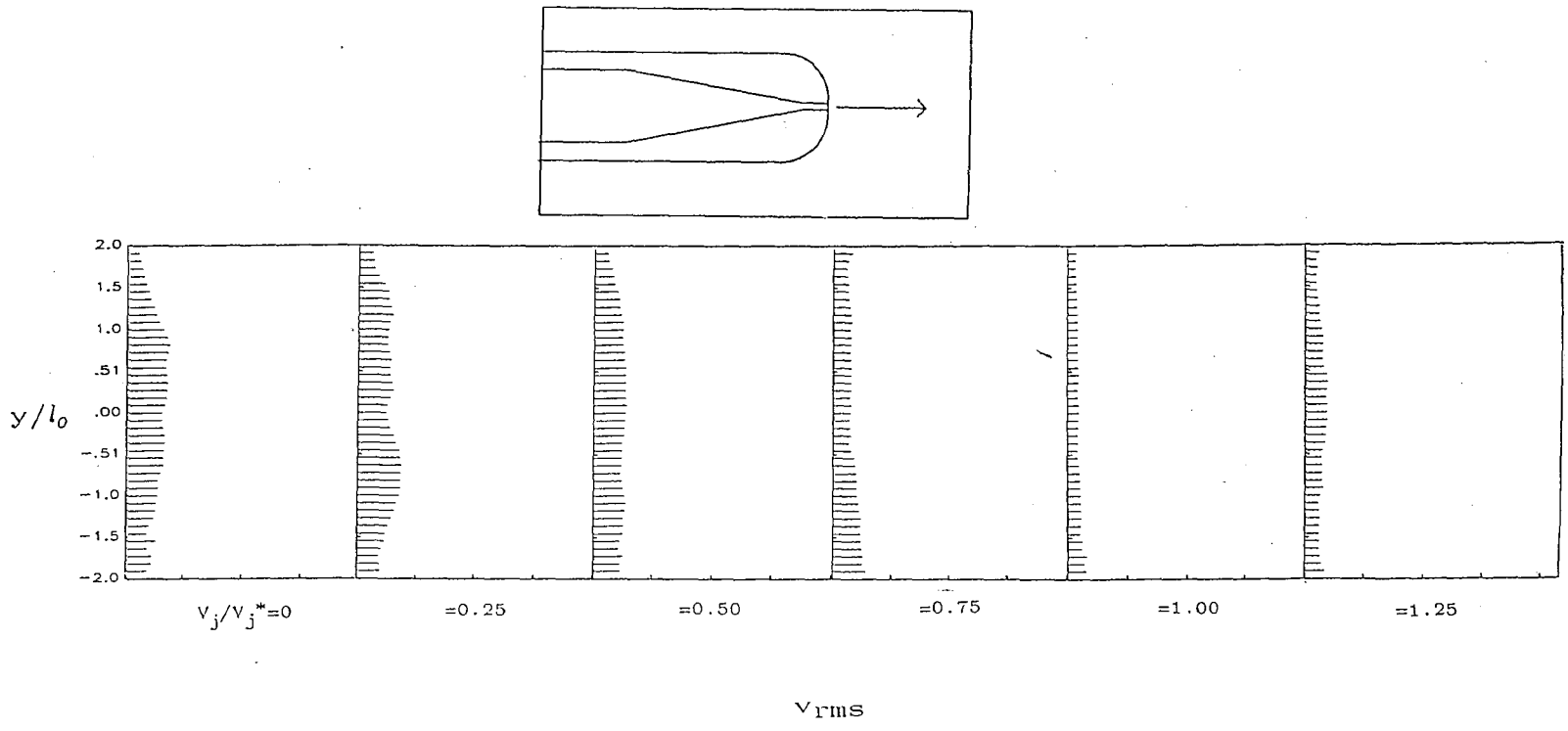

FIGURE 8.4: Comparison of profiles of v_{rms} for single-slit trailing-edge (#1) at all blowing rates. (Note: v_{rms} is not normalized.)

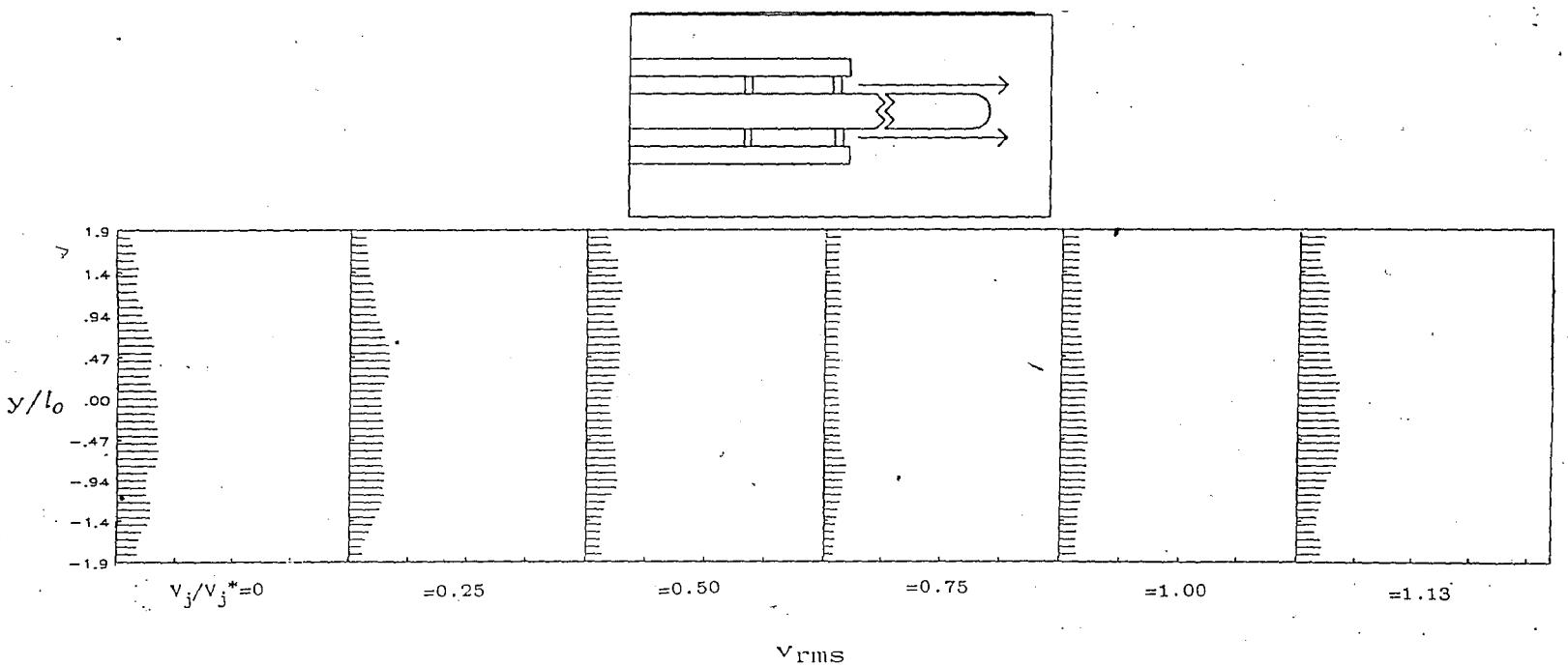

FIGURE 8.5: Comparison of profiles of v_{rms} for double-slit trailing-edge (#2) at all blowing rates. (Note: v_{rms} is not normalized.)

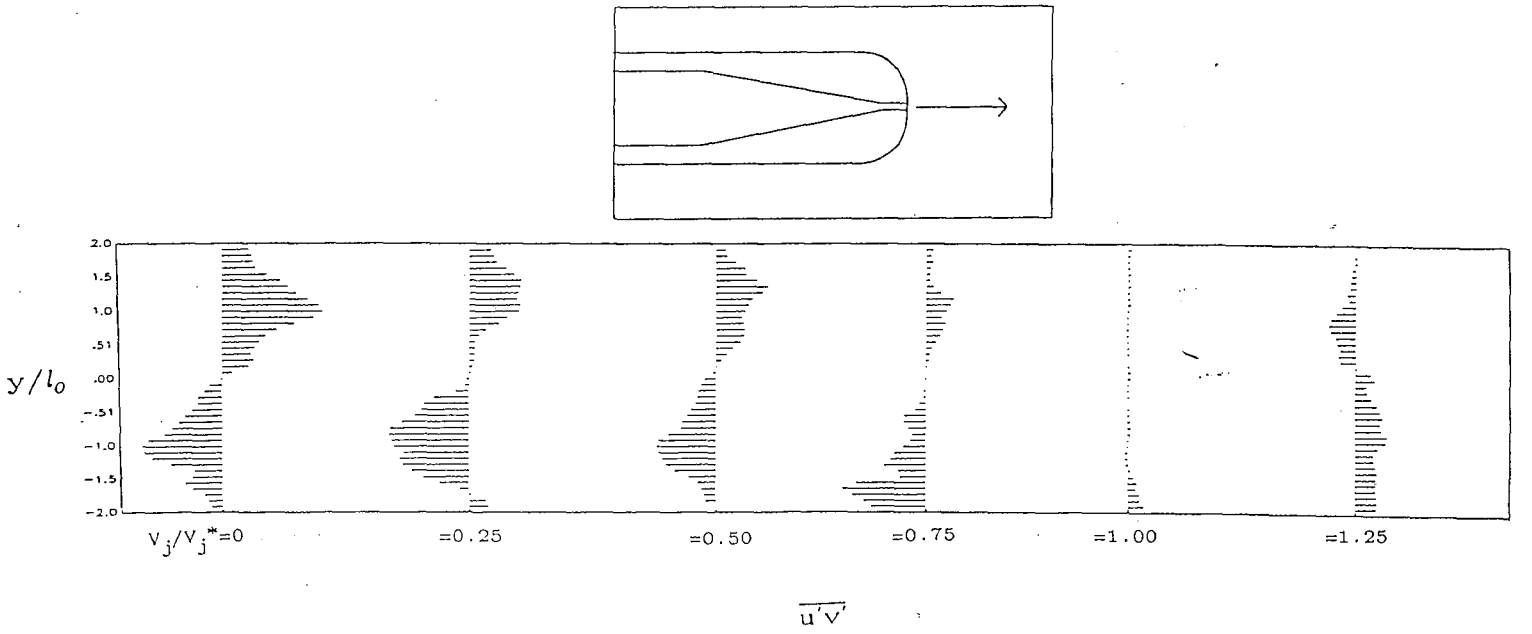

FIGURE 8.6: Comparison of profiles of Reynolds stress for single-slit trailing-edge (#1) at all blowing rates. (Note: Reynolds stress is not normalized.)

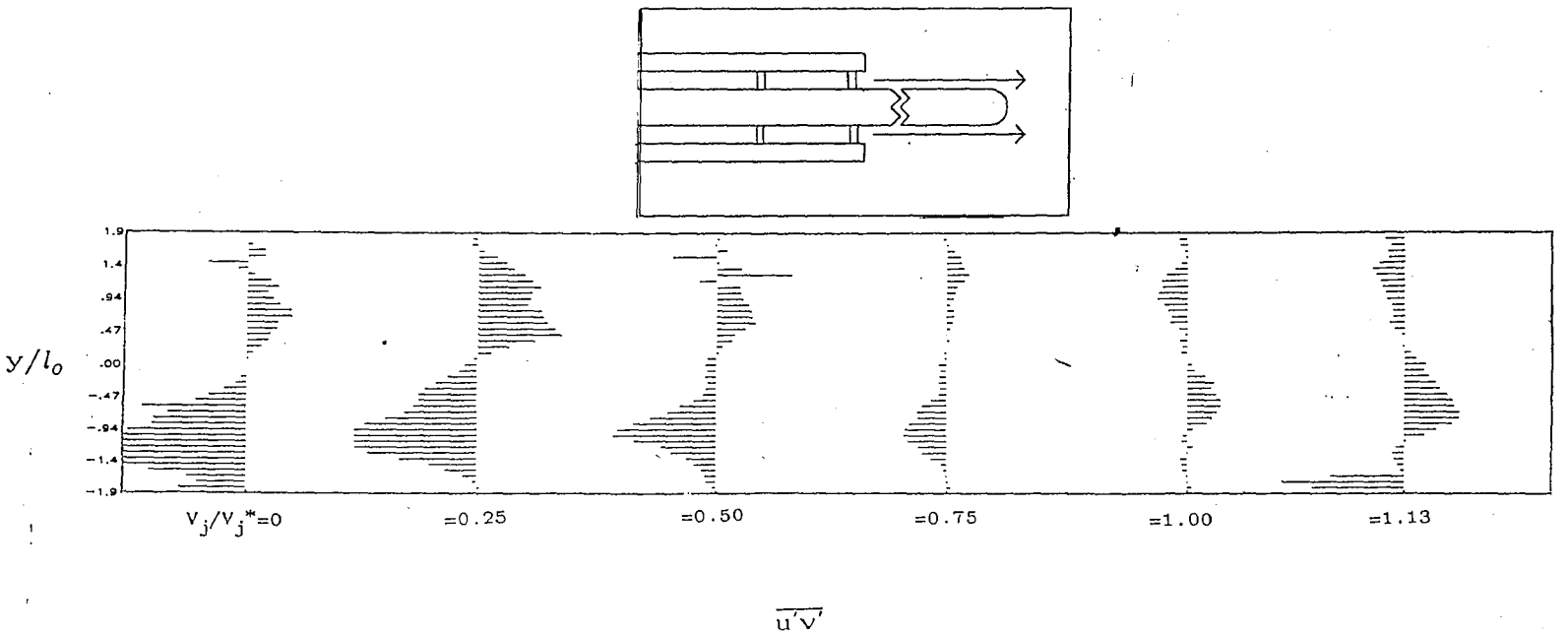

FIGURE 8.7: Comparison of profiles of Reynolds stress for double-slit trailing edge (#2) at all blowing rates. (Note: Reynolds stress is not normalized.)

APPENDIX A--OPTICAL FORMULAE

The following formulae have been taken from the Melles-Griot Optics Guide 3, and are useful for calculating the focal length of a combination of lenses. The assumption has been made that the user knows the locations of the principal points within the lenses, or that the lenses are thin enough that the principal points do not vary greatly with distance from the center of the lens. This assumption was made throughout most of the work presented. If this assumption is not applicable, or if other difficult circumstances arise, consultation of the above optics guide is suggested.

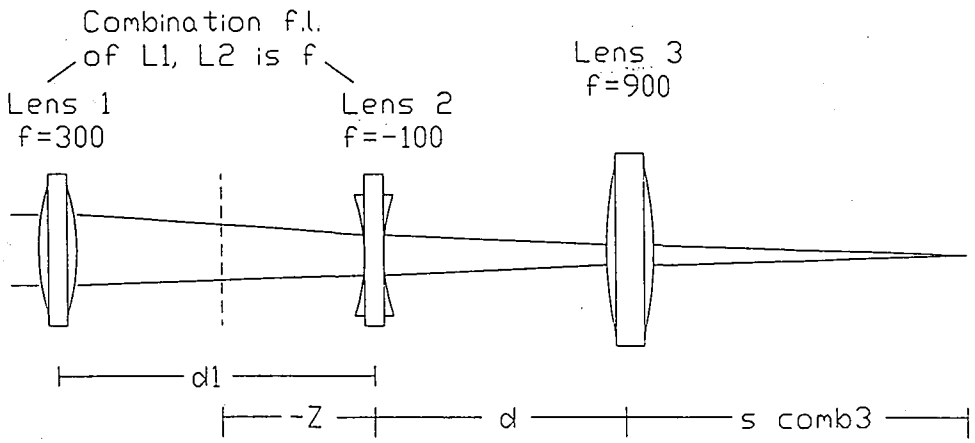

FIGURE A1: Schematic of three lens system.

Note: Z is positive if it falls to the right of lens 2 and negative if it

The distance from the second principal point of the second element in a two lens combination, to the final focal point of the combination is:

$$s=\frac{f_2(f_1-d1)}{f_1+f_2-d1} \qquad (1)$$

where the f values represent the focal lengths of the lenses and d represents the distance between them (literally between the secondary principal point of the first element and the primary principal point of the second).

The literal definition of s is the point at which an object at infinity would project an image, real or virtual (+ or -) through the lens combination.

For the telephoto combination discussed previously within the main body of the thesis, the first lens is convex and has a positive focal length, and the second is concave and has a negative focal length. It should be noted that the distance between the lenses in this combination often greatly varies the final focal point of the arrangement.

For laser use, the value of s gives a good feel for where the beam will reach a point of high intensity. To find the value of s for a combination of three lenses, we must first define the following.

The effective focal length for a combination of two lenses is defined:

$$f=\frac{f_1 f_2}{f_1+f_2-d1} \qquad (2)$$

where all nomenclature is as above. This value must be determined for the first two elements as must the value of s from equation 1.

The distance to the combination secondary principal point measured from the principal point of the second lens is defined as:

$$z=s-f \qquad (3)$$

[It should be noted that z is positive if it falls to the right of lens 2, and negative if it falls to the left (as seen in figure A1).]

This must also be found for the first two elements. Knowing all of this information, the final focal length for the combination can be found as follows:

$$s_{comb3}=\frac{f_3(f-(d-z))}{f+f_3-(d-z)} \qquad (4)$$

where f_3 is the focal length of the third element, f is the effective focal length of the first two elements, d is the

distance between the second and third lenses, and z is defined as above.

Experiments were done using a telephoto combination of lenses followed by a laser focusing singlet. The focal lengths in turn were 300mm, -100mm, and 900mm. The lenses in the telephoto combination were spaced 212mm apart, with the laser singlet spaced 140mm further back. The combination focal length was 357.6mm.

APPENDIX B--INTERROGATION PROCESS

As mentioned in the section detailing the Particle Image Velocimetry technique, the actual analysis of the photographic test negatives is known as interrogation. The apparatus used to accomplish this task appears in figure B1. The interrogation apparatus and control program PDV were obtained from Fluid Flow Diagnostics.

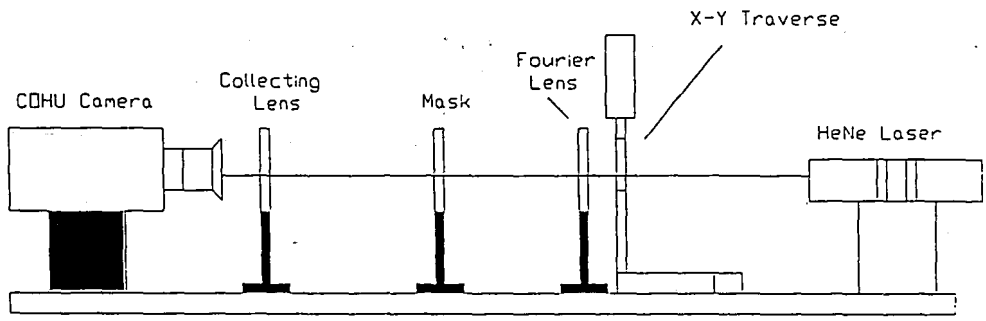

FIGURE B1
Interrogation Apparatus

The photographic negative to be interrogated is placed in the traverse as detailed in the figure. The traverse consists of a slide holder that can be moved along two axes by a pair of Klinger stepping motors. The stepping motors are adjusted so that the HeNe laser beam, also pictured in the figure, is incident upon the negative at the lower left hand corner. From here on, the processing is controlled by

the computer (running program PDV, again from Fluid Flow Diagnostics). These stepping motors will be used to move the negative frame so the negative can be completely scanned by the laser.

The laser light will illuminate a very small area of the negative (apx. 0.5 mm^2) before passing into the Fourier transform lens also pictured in figure B1. The Fourier Transform lens is nothing more than a standard, double convex lens positioned to take advantage of a lense's natural ability to perform two-dimensional optical Fourier transforms. This phenomenon occurs due to the varying diffraction rates found at different positions on a lens (due to the differences in thickness). The varying rates of diffraction will cause phase differences of the transmitted light, again depending on the location on the lens that the light passes through. This phase difference, for a single location, can be represented as follows:

$$t(x,y)=\exp[ikn\Delta_o]\ \exp[-i\ \frac{k}{2f}\ (x^2 + y^2)]$$

where n is the index of refraction of the lens, f is its focal length, Δ_o is the reference lens thickness (in this case, the thickness at the midpoint), x and y represent positions measured from a reference point, k is a constant and i represents the square root of -1.

Through a derivation appearing in Goodman (1968), for an object at a set distance d in front of the lens, a surface integration can be performed on the above, showing that an optical Fourier transform of the illumination of the object will appear at the focal length of the lens. The optical character of this transform will depend on the nature of the object involved.

If more than one object is within the field of illumination, the variance in phase in the light will cause

an interference pattern to form at the same location. These signals combine in a convolution pattern. This interference pattern therefore contains information that relates the optical orientaion of the various objects. The visible form of this information is a Young's fringe pattern formed in the Fourier plane.

In the Particle Image Velocimetry technique, when the Laser illuminates a small area of the negative, the objects causing the formation of the interference pattern will be the small number particle images within the illuminated area. Given proper spacing, the interference pattern will produce Young's fringes.

This Young's fringe pattern is characterized by parallel rows of light and darkness, with a given orientation and spacing. The pattern appears visibly on the screen due to the positioning of a collecting lens and a video camera at the image point of the fourier lens. The contrast of the fringes can be adjusted in order to expedite interpretation. The mask appearing in figure B1 ahead of the collecting lens is present in order to protect the camera from the direct light of the laser.

The image of the fringe is digitized after being processed through a frame grabbing board of the computer. A two dimensional FFT then performs an inverse Fourier transform on the image. The result is mathematically decomposed into five terms (as per Liu, Landreth, Adrian, and Hanratty, 1991):

$$G(s)=G_{D+}(s) + G_P(s) + G_{D-}(s) + G_C(s) + G_F(s)$$

When represented on a contour plot the 2D inverse transform demonstrates one large central peak $G_P(s)$, flanked by two smaller, equally distant satellite peaks $G_{D+,D-}$, and otherwise surrounded by noise. The relative

distance between the satellite peaks and the central peak can be represented by distances ΔX and ΔY.

These values can be related to velocities as follows:

$$u=\frac{\Delta X}{\Delta t\ M} \qquad v=\frac{\Delta Y}{\Delta t\ M}$$

where Δt represents the times between successive scans of the laser beam, and M represents the magnification factor incorporated in the photography. The program utilized for this study represented the velocity vectors as a ratio of the displacements since scanning time and magnification apply in both directions.

The program used (again PDV) controls the stepping motors and searches each area of the negative for fringes. If the generated fringe pattern meets a certain confidence level selected by the user, a velocity vector is generated. Otherwise the fringes are rejected and the computer moves on. A typical scan would include examination of a 32mm X 22mm negative at aproximately .5mm intervals.

Once PDV has run its course, the information can be processed (using program CVPIV, by Magness, 1991) and viewed (using program V, by Robinson, 1991). This piece of software allows for the elimination of errant vectors by the user. It also provides various scaling and biasing operations. The biasing operations are necessary if a biasing mirror is used. They can also be used to illustrate the turbulent velocity fields present by somewhat lessening the effect of the mean flow velocity. Final processing can include interpolation of any spaces left within the initial data in order to provide a full field of data (done by program FILV, Robinson and Magness, 1991). Program FILV also generates grid files of constant vorticity. Using program SURFER (Golden Software, 1989),

these fields of constant vorticity can be viewed in a topological format.

APPENDIX C--PROGRAM FANDANGO/BARFLY

The listing of program FANDANGO follows. A description of its purpose can be found within the body of the thesis. It was written in TURBO C, by Tim Corcoran and Jason Redi (Lehigh Comp. Eng.). Alternate copies may be listed within the systems at Lehigh as program BARFLY. This series of programs simply presents the data in a normalized fashion.

```
#include <stdio.h>
#include <math.h>
#define YPEAK 50
#define XPEAK 60
#define NUMFILES 15
#define FILENAMELEN 15
#define LOW_Y 0

int get_infile(char [][]);
void get_outfile();
int readinput();


main()
{
FILE *outfile=NULL,*outrmu=NULL,*outrmv=NULL,*outtur=NULL;
char filename[NUMFILES][FILENAMELEN];
int i=0;
float totalu[YPEAK][NUMFILES],totalv[YPEAK][NUMFILES];
float urms[YPEAK][NUMFILES],vrms[YPEAK][NUMFILES],turb[YPEAK][NUMFILES];
float finalu[YPEAK],finalv[YPEAK],yidx=0;
float finalru[YPEAK],finalrv[YPEAK],finalt[YPEAK];
int fileindex,numfiles,yindex=0;
float ytotal;
char format[80]="";

float x,y,u,v;

printf("Particle Image Velocimetry Averaging System\n");
printf("Jason K. Redi --Tim Corcoran\n");


printf("\n");
printf("\n");

/* initalize total u and total v as well as the finalu and finalv */
for (yindex=0;yindex<=YPEAK;yindex++) {
        finalu[yindex]=0;
        finalv[yindex]=0;
        finalru[yindex]=0;
        finalrv[yindex]=0;
        finalt[yindex]=0;

        for (fileindex=0;fileindex<=NUMFILES;fileindex++) {
                totalu[yindex][fileindex]=0;
                totalv[yindex][fileindex]=0;
                vrms[yindex][fileindex]=0;
                urms[yindex][fileindex]=0;
                turb[yindex][fileindex]=0;
        }
}


numfiles=get_infile(filename);

get_outfile(&outfile,&outrmu,&outrmv,&outtur);

ytotal=readinput(filename,totalu,totalv,urms,vrms,turb);


     /* average all the values from all the files */
     for (fileindex=0;fileindex<=numfiles;fileindex++) {
```

```
        for (yindex=0;yindex<=ytotal;yindex++) {
                finalv[yindex]+=totalv[yindex][fileindex];
                finalu[yindex]+=totalu[yindex][fileindex];
                finalru[yindex]+=urms[yindex][fileindex];
                finalrv[yindex]+=vrms[yindex][fileindex];
                finalt[yindex]+=turb[yindex][fileindex];
                  }
        }

    for (yindex=0;yindex<=ytotal;yindex++) {
       finalu[yindex]/=numfiles+1;
       finalv[yindex]/=numfiles+1;
       finalru[yindex]/=numfiles+1;
       finalrv[yindex]/=numfiles+1;
       finalt[yindex]/=numfiles+1;
         }


        /* do output! */
x=0;
v=0;
ytotal=(ytotal)*(.5);
i=0;
strcpy(format,"    %12.6e    %12.6e        %12.6e    %12.6e\n");
printf("Writing Output files.\n");
for(yidx=0;yidx<=ytotal;yidx+=0.5) {

        fprintf(outfile,format,x,yidx,finalu[i],v);

        fprintf(outrmu,format,x,yidx,finalru[i],v);

        fprintf(outrmv,format,x,yidx,finalrv[i],v);

        fprintf(outtur,format,x,yidx,finalt[i],v);

        i++;
        }

        fprintf(outfile,format,1.0,0.0,0.0,0.0);
        fprintf(outrmu,format,1.0,0.0,0.0,0.0);
        fprintf(outrmv,format,1.0,0.0,0.0,0.0);
        fprintf(outtur,format,1.0,0.0,0.0,0.0);


fclose(outfile);
fclose(outrmu);
fclose(outrmv);
fclose(outtur);

}


int get_infile(filenames)
char filenames[NUMFILES][FILENAMELEN];
{
 int fileindex=0;

        printf("Enter the datafile names<CR>, hit only <CR> to finish:\n");
        printf("%15sFile number %d =>"," ",fileindex+1);

        while ((strcmp((gets(filenames[fileindex])),"")!=0)
                && (fileindex<=NUMFILES)) {
```

```
                fileindex++;
                printf("%15sFile number %d =>"," ",fileindex+1);
                }

        printf("\n");

        return(fileindex-1);
}


void get_outfile(outfile,outrmu,outrmv,outtur)
FILE **outfile,**outrmu,**outrmv,**outtur;
{
char outfilename[FILENAMELEN]="";
char extfilename[FILENAMELEN]="";

    while (1){

        printf("Please enter an output file name (with no extension):");

        if (strcmp((gets(outfilename)),"")==0);

        else if ((*outfile=fopen(outfilename,"r"))!=NULL) {
            printf("HEY! Your file already exists!\n");
            printf("Please enter another name:");
        } /* end if */

        else if ((*outfile=fopen(outfilename,"w"))==NULL) {
            printf("Sorry, you outputfile cannot be opened for some reason.\n");
            printf("Please enter another one:");
            } /* end else -if */


        else {
            strcpy(extfilename,outfilename);
            strcat(extfilename,".rmu");
            if ((*outrmu=fopen(extfilename,"w"))==NULL) {
                printf("couldn't create outrmu\n");
                exit(1);
                }
            strcpy(extfilename,outfilename);
            strcat(extfilename,".rmv");
            if ((*outrmv=fopen(extfilename,"w"))==NULL) {
                printf("couldn't create outrmv\n");
                exit(1);
                }
            strcpy(extfilename,outfilename);
            strcat(extfilename,".tur");
            if ((*outtur=fopen(extfilename,"w"))==NULL) {
                printf("couldn't create outtur \n");
                exit(1);
                }
            return;
            } /*end else */
        } /* end while */

}
 /* end get_outfile() */
```

```
int readinput(filename,totalu,totalv,urms,vrms,turb)
char filename[NUMFILES][FILENAMELEN];
float totalu[YPEAK][NUMFILES],totalv[YPEAK][NUMFILES];
float urms[YPEAK][NUMFILES],vrms[YPEAK][NUMFILES],turb[YPEAK][NUMFILES];
{
FILE *inputfile=NULL;
int fileindex=0;
int yindex,xindex=0,xcount;
int ytotal=0;
float x,y,u,v,lasty;
float vsqt=0,usqt=0,tinst=0,uprime=0,vprime=0;
float matu[XPEAK][YPEAK],matv[XPEAK][YPEAK];


yindex=0;

/*  Do all the work -> loop until we find a <CR> as a filename */
while (strcmp(filename[fileindex],"")!=0) {

ytotal=0;
/* open the file-> make sure it is there */
        if ((inputfile=fopen(filename[fileindex],"r"))!=NULL) {
        printf("Processing file :%s\n",filename[fileindex]);
        lasty=LOW_Y;
                while (fscanf(inputfile," %f %f %f %f",&x,&y,&u,&v)==4){

                        if (lasty!=y)  {
                                yindex++;
                                xindex=0;
                                } /* end if */

                        xindex++;


                        totalu[yindex][fileindex]+=u;
                        totalv[yindex][fileindex]+=v;
                        matu[xindex][yindex]=u;
                        matv[xindex][yindex]=v;

                        lasty=y;
                        }  /* end while*/

                ytotal=yindex;
                yindex=0;

                while  (yindex<=ytotal) {
                        usqt=0;
                        vsqt=0;
                        tinst=0;

                        totalv[yindex][fileindex]/=xindex;
                        totalu[yindex][fileindex]/=xindex;

                        for(xcount=1;xcount<=xindex;xcount++) {
                                uprime=matu[xcount][yindex]-totalu[yindex][filei
                                vprime=matv[xcount][yindex]-totalv[yindex][filei

                                usqt+=(uprime*uprime);
                                vsqt+=(vprime*vprime);

                                tinst+=(uprime*vprime);
                                }

                        usqt/=
```

```
                        xindex;
                        vsqt/=xindex;
                        tinst/=xindex;

                        turb[yindex][fileindex]=tinst;
                        urms[yindex][fileindex]=sqrt(usqt);
                        vrms[yindex][fileindex]=sqrt(vsqt);


                        yindex++;

                        } /*end while */

        yindex=0;
        xindex=0;
        lasty=0;
        } /* end  if */

        /* else bad file name */
        else {
                printf("Can't find file %s!\n",filename[fileindex]);
                printf("going on to the next file %s.\n",filename[fileindex+1]);

                }   /* end else */
        printf("Done.\n");
        fclose(inputfile);
        fileindex++;


} /* end while */
printf("Leaving read_input()\n");
return(ytotal);

} /* end get_input */
```

REFERENCES--Grouped by subtopic and author name.

Jet Engine Noise Generation

Kemp, N.H. and Sears, W.R. 1955, "The Unsteady Forces Due to Viscous Wakes in Turbomachines," Journal of the Aeronautical Sciences, Vol. 22 No. 7, pp. 478-483.

Kuethe, A.M. 1972, "Effect of Streamwise Vorticies on Wake Properties Associated with Sound Generation," Journal of Aircraft, Vol. 9 No. 10 (October) pp. 715-718.

Wagner, W.B. and Mathews, D.C. 1991, "Pratt-Whitney Jet Engine Noise Reduction Technology," Presentation at Lehigh University February 22, 1991 and other private communications.

Momentumless Wake Concepts

Bearman, P.W., 1966, "Investigation Into the Effect of Base Bleed on the Flow Behind a Two-Dimensional Model with a Blunt Trailing Edge," AGARD Conf. Proc., No. 4 pp. 479-507.

Dmitrenko, Y.M., Kovalev, I.I., Luchko, N.N., Cherepanov, P.Y., 1987, "Plane Turbulent Wake with Zero Excess Momentum," Journal of Engineering Physics (Russian), Vol. 52 No. 5 (May), pp. 536-542.

Finson, M.L., 1975, "Similarity Behaviour of Momentumless Turbulent Wakes," Journal of Fluid Mechanics, Vol. 71 part 3, pp. 465-479.

Hassid, S., 1980, "Similarity and Decay Laws of Momentumless Wakes," Physics of Fluids, Vol. 23 No. 2 (February), pp. 404-407.

Higuchi, H., 1977, "Experimental Investigation of Axisymmetric Turbulent Wakes with Zero Momentum Defect," Ph. D Thesis, 1977, California Institute of Technology.

Motallebi, F., and Norbury J.F., 1981, "The Effect of Base Bleed on Vortex Shedding and Base Pressure in Compressible Flow," Journal of Fluid Mechanics, Vol. 110, pp.273-292.

Naudascher, E., 1965, "Flow in the Wake of Self-Propelled Bodies and Related Sources of Turbulence," Journal of Fluid Mechanics, Vol. 22 part 4, pp. 625-656.

Naumann, R.G., 1992, Anticipated Thesis Work, Lehigh University.

Park, W., 1989, "An Experimental Investigation of the Turbulent Structure in Two-Dimensional Momentumless Wakes," Ph.D. Thesis, Pennsylvania State University.

Park, W., and Cimbala, J.M., 1991, "The Effect of Jet Injection Geometry on Two-Dimensional Momentumless Wakes," Journal of Fluid Mechanics, Vol. 224, pp. 29-47.

Ridjanovic, M., 1963, "Wake with Zero Change of Momentum Flux," Ph. D. Thesis, State University of Iowa.

Schetz, J.A. and Jakubowski, A.K., 1975, "Experimental Studies of the Turbulent Wake Behind Self-Propelled Slender Bodies," AIAA Journal, Vol. 13 No. 12 (December).

Schooley, A.H. and Stewart, R.W., 1962, "Experiments with a Self-Propelled Body Submerged in a Fluid with a Vertical Density Gradient," Journal of Fluid Mechanics, Vol. 15 part 1, pp. 83-97.

Swanson, R.C. and Schetz, J.A., 1975, "Calculations of the Turbulent Wake Behind Slender Self-Propelled Bodies with a Kinetic Energy Method," Journal of Hydronautics, Vol. 9 No. 2 (April), pp. 78-80.

Tennekes, H. and Lumley J.L, 1972, "A First Course in Turbulence," The MIT Press, Cambridge, MA.

Wang, H., 1965, "Flow Behind a Point Source of Turbulence," Ph. D. Thesis, State University of Iowa.

Wood, C.J., 1964, "The Effect of Base Bleed on a Periodic Wake", Journal of the Royal Aeronautical Society, Vol. 68 (July), pp. 477-482.

Wood, C.J., 1967, "Visualization of an Incompressible Wake with Base Bleed," Journal of Fluid Mechanics, Vol. 29 part 2, pp. 259-272.

Particle Image Velocimetry

Adrian, R.J., 1986, "Multi-Point Optical Measurements of Simultaneous Vectors in Unsteady Flow--A Review," Int. Journal of Heat and Fluid Flow, Vol. 7 No. 2 (June), pp. 127-145.

Adrian, R.J., 1991, "Particle-Imaging Techniques for Experimental Fluid Mechanics," Annual Review of Fluid Mechanics, no. 23, pp. 261-304.

Adrian, R.J. and Yao, C., 1985, "Pulsed Laser Technique Application to Liquid and Gaseous Flows and the Scattering Power of Seed Materials," Applied Optics, Vol. 24 No. 1 (January), pp. 44-52.

Burch, J.M. and Tokaraski, J.M.J., 1968, "Production of Multiple Beam Fringes from Photographic Scatters," Optica ACTA, Vol. 15 No. 2, pp. 101-111.

Goodman, J.W., 1968, "Introduction to Fourier Optics," McGraw-Hill, San Francisco.

Gray, C. and Greated, C.A., 1988, "The Application of Particle Image Velocimetry to the Study of Water Waves," Optics and Lasers in Engineering, no. 9, pp. 265-276.

Keane, R.D. and Adrian R.J., 1989, "Optimization of Particle Image Velocimeters," L.I.A. ICALEO, Vol. 68, pp. 141-161.

Landreth, C.C., Adrian, R.J., and Yao, C., 1986, "Double Pulsed Laser Velocimeter with Directional Resolution for Complex Flows," 10th Symposium on Turbulence, University of Missouri-Rolla, September 23-25.

Liu, Z.-C., Landreath, C.C., Adrian, R.J., and Hanratty, T.J., 1991, "High Resolution Measurement of Turbulent Structure in a Channel with Particle Image Velocimetry," Experiments in Fluids, Vol. 10, pp. 301-312.

Magness, C.L., 1991, "A Visual Study of the Unsteady Flow Structures of a Pitching Delta Wing," Ph.D. Thesis, Lehigh University.

Melles-Griot Optics Guides, 1991 (No. 5), Melles-Griot Optics Corp., Irvine, CA.

Redi, J.K., Corcoran, T.E., 1991, Program Fandango/Barfly--An Averaging Program to Convert Particle Image Velocimetry Results into Turbulence Data, Lehigh University Dept. Computer Engineering/ Mechanical Engineering.

Robinson, O., 1991, Program V Version 2.7, Program to Display Particle Image Velocimetry Results, Lehigh University Dept. Mechanical Engineering.

Towfighi, J., 1992, Anticipated thesis work, Lehigh University.

Welsh, M., 1991, Personal Communication.

Previous Wake Studies: Flate Plates, Rotor Blades, Turbulent Boundary Lavers

Andreopoulous, J. and Bradshaw, P., 1980, "Measurements of Interacting Turbulent Shear Layers in the Near Wake of a Flat Plate," Journal of Fluid Mechanics, Vol. 100 part 3, pp. 639-668.

Chervay, R., and Kovasznay, L.S.G., 1969, "Turbulence Measurements in the Wake of a Thin Flat Plate," AIAA Journal, Vol. 7 No. 8 (August), pp. 1641-1643.

Johansen, John, 1982, "The Effect of Cylindrical Surface Modifications of Turbulent Boundary Layers," Master's Thesis, Lehigh University.

Klebanoff, P.S., Schubauer, G.B., and Tidstrom, K.D., 1955, "Measurements of Effects of Two-Dimensional and Three-Dimensional Roughness Elements on Boundary Layer Transition," Journal of Aeronautical Sciences, Vol. 22 no. 11, pp.803.

Majjigi, R.K. and Gliebe, P.R., "Development of a Rotor Wake/Vortex Model," NASA--Lewis Contract NAS3-23681, General Electric Aircraft Engine Business Group.

VITA

The author was born in Wilkes-Barre, Pennsylvania to Edward W. Corcoran, Sr. and Ruth M. Corcoran on November 3, 1968.

He receive his B.S. in Mechanical Engineering from Lehigh University.

He is a current employee of the United States Navy working out of Norfolk Naval Yard, Portsmouth, Virginia.

END

OF

TITLE